Universidad Rey Juan Carlos

TESIS DOCTORAL

Fatigue behaviour of Polyamide 12 processed by Selective Laser Sintering

Autor:

Alberto Jesús Cano Aragón

Directores:

Alicia Salazar López

Jesús Rodríguez Pérez

Programa de Doctorado en Tecnologías Industriales:

Química, Ambiental, Energética, Electrónica, Mecánica y de los Materiales

Escuela Internacional de Doctorado

2021

Failure is an option here. If things are not failing,

you are not innovating enough.

Elon Musk

ACKNOWLEDGMENTS

Permítame el lector el uso de mi lengua materna para recoger a todas esas personas que han hecho posible el plasmar en este documento tan arduo, a la par de gratificante, el trabajo llevado a cabo durante estos cinco años.

Comenzando por tanto mis más sinceros agradecimientos, a mis directores Alicia y Jesús. Debo agradeceros a los dos esa oportunidad que se me brindó al comienzo de esta etapa y sobre todo por la confianza en mi labor que habéis ido depositando todo este tiempo. Gracias Alicia por transmitirme tu forma de realizar las tareas, hecho que ha mejorado mucho mi orden (todo sea dicho), por toda tu paciencia y dedicación durante las interminables horas junto a la máquina y también frente al "Kaleida", aunque estas últimas no se vean tanto.

A ti Jesús, por todos esos coloquios en los que hemos ido viendo la luz y enfocando todo el trabajo realizado, por aportarme en muchas ocasiones otra visión desconocida para mí.

Continúo agradeciendo a todos y cada uno de los integrantes del grupo de Durabilidad e Integridad Mecánica de Materiales Estructurales de la URJC, esa pequeña "familia investigadora", tanto su acogida, como su apoyo durante estos años. Un agradecimiento especial a mi compañero de despacho, Álvaro, por sus consejos de "hermano mayor" que me han sido de gran utilidad en lo profesional y en lo personal, por siempre haber estado dispuesto a echarme

una "mano". A Pedro por todas sus lecciones y experiencia que han sido fundamentales durante este tiempo, sin tu ayuda, hoy no podríamos disfrutar de todas las micrografías tomadas en el SEM que se presentan en este trabajo. A Claudio por todo el apoyo, incluyendo ese estupendo apoyo en formato "DVD" que siempre me ha ofrecido y ahora solicito. A Miguel Ángel y Teresa por estar siempre dispuestos a resolver esas dudas con las que me iba topando día a día.

Y por supuesto no se me olvidan mis amigos de laboratorio, David Merino, David Cruz, Mario, Sole, Luis, Carlos y Noelia, gracias a todos por el apoyo y los ánimos que me habéis aportado desde que compartimos nuestra vocación. Sin vosotros, toda la labor experimental no hubiera sido posible. Os deseo mucha suerte, a los que todavía os encontráis inmersos en el doctorado, para terminarlo con éxito.

En este apartado, te quiero dar un agradecimiento especial a ti Rocío, porque no sé ni cómo expresar todo el apoyo que he recibido de tu parte, porque me has visto caer y has estado ahí para ayudarme a seguir siempre sacándome una sonrisa.

También quiero agradecer al departamento de Ciencia de materiales y ensayo de polímeros de la MontanUniversität de Leoben, especialmente al catedrático Gerald Pinter, a Florian Arbeiter y a Anja Gosch por su acogida y ayuda durante mi estancia en Austria.

Por supuesto, a toda mi familia, mis padres Ana y Juan Manuel, a mi hermano Dani, mi yaya Julia, mi tía Sonia y mis primos Rodrigo y Gonzalo, que me han sufrido durante todo este proceso, haciéndome llegar siempre su cariño incondicional. A mi yayo Pepe, que, aunque no haya podido llegar a verme

presentar este trabajo, me ha permitido ser la persona que soy hoy en día, inculcándome sus valores, gracias.

A todos mis amigos de "Los Tuners", con los que he crecido y de los que recibo tanto apoyo día tras día desde, prácticamente, 1992.

A ti Ana, por haberme visto crecer e incluso, aun habiéndome sufrido de compañero de mesa en el instituto (tampoco era tan terrible como ciertas fuentes pueden indicar) y durante la elaboración de este trabajo (aquí es posible que sí haya sido insufrible), estar en mi vida de una manera tan bonita, siempre con una sonrisa y unas bonitas palabras.

Finalizando estos "breves" párrafos pidiendo disculpas a todas esas maravillosas personas que han ayudado y aportado a mi desarrollo durante este tiempo y que no queden explícitamente recogidas en este escrito debido a la fatiga propia del proceso de escritura y al agotamiento mental con la que llego al final de esta etapa.

CONTENTS

Page

RESUMEN

Antecedentes

El desarrollo de la fabricación aditiva en polímeros ha supuesto una gran revolución en la industria del procesado de estos materiales, alcanzando un gran peso en sectores como el energético, el automotriz, el aeronáutico o el sanitario, entre muchos otros. La gran variedad de técnicas adaptadas a las distintas familias de materiales poliméricos ha permitido abordar diseños muy complejos. De entre todas las técnicas, las pertenecientes a la categoría de fusión de polvo en cama caliente son las más extendidas, destacando la técnica de sinterizado selectivo por láser (*Selective Laser Sintering*, *SLS*). Esta técnica puede ser utilizada en una amplia variedad de polímeros, no necesita soportes para la fabricación de la pieza final, los polvos sobrantes pueden ser reutilizados y, sobre todo, presenta una muy buena relación calidad-precio. De entre todas las familias de polímeros fabricadas por *SLS* destaca la de las poliamidas, con una cuota del 95% del total del mercado de SLS. En concreto, la poliamida 12 (PA-12) se caracteriza por su alta resistencia a sustancias químicas y, sobre todo, por sus buenas propiedades mecánicas: elevada tenacidad de fractura, notable resistencia a la fatiga y buen comportamiento frente al desgaste.

Los polímeros procesados mediante *SLS* se caracterizan por estar compuestos por una estructura de capas que puede condicionar su respuesta mecánica y su resistencia a fractura y a fatiga, por su comportamiento anisótropo y por los defectos inherentes a estas técnicas de procesado. Aunque existen estudios sobre el comportamiento mecánico de la PA-12 procesada mediante fabricación aditiva, son bastante escasos los enfocados al comportamiento a fractura y a fatiga. Además, la mayoría están orientados hacia la evaluación del efecto de los parámetros de procesado en el comportamiento mecánico medido principalmente mediante ensayos de tracción y/o flexión.

Objetivos

El objetivo principal de esta tesis doctoral es estudiar el comportamiento a fatiga de la PA-12 procesada mediante *SLS* y compararlo con el del mismo material procesado por la técnica convencional de moldeo por inyección (*Injection Moulding*, *IM*). Para ello, se ha realizado un extenso programa experimental que aporta datos relevantes sobre el comportamiento de este material y permite comparar la capacidad resistente frente a la fractura y a la fatiga de las piezas procesadas por técnicas de fabricación aditiva y técnicas convencionales. Debido a que en las técnicas de fabricación aditiva las piezas se construyen por deposición capa a capa, es posible encontrar respuestas anisótropas, concretamente comportamientos transversalmente isótropos. Por ello, se decidió llevar a cabo toda la caracterización mecánica, a fractura y a fatiga aplicando la fuerza en la dirección perpendicular y paralela a la estructura laminar.

Metodología

En primer lugar, se han determinado las propiedades térmicas y microestructurales más relevantes de este termoplástico semicristalino,

incluyendo las temperaturas de transición vítrea, el grado de cristalinidad, la porosidad o el tamaño de esferulitas, junto con algunas características de las probetas más asociadas al proceso de fabricación, como la rugosidad y la morfología piel núcleo. Se han detectado algunas diferencias significativas entre los dos procedimientos de fabricación, especialmente en el tamaño de las esferulitas y en la rugosidad superficial, siendo ambos valores mucho menores en el caso de las probetas moldeadas por inyección. Además, éstas presentaron una capa superficial de material amorfo.

Respecto a la caracterización mecánica, se han realizado ensayos de tracción cuyos resultados no muestran grandes diferencias entre las probetas *SLS* e *IM*, ni tampoco entre orientaciones diferentes en el caso de las probetas procesadas por fabricación aditiva. La diferencia más marcada está en el alargamiento a rotura, que es sensiblemente menor en el caso de las muestras procesadas por *SLS* y, dentro de éstas, en las muestras cuya orientación de capas era perpendicular a la dirección de la fuerza aplicada.

En cuanto al comportamiento a fractura, la poliamida ha presentado en todos los casos una respuesta no lineal que ha obligado a una caracterización basada en la integral J. Los valores críticos de este parámetro no muestran variaciones relevantes entre los materiales procesados por *SLS* o por *IM*, ni tampoco entre las diferentes orientaciones ensayadas. Tan sólo cabe mencionar que las probetas SLS en las que la dirección de la carga aplicada era paralela a la orientación de las capas presentaron la mayor resistencia a la propagación estable de grieta, mientras que la energía necesaria para el inicio de la propagación de la grieta fue superior en las probetas inyectadas.

En relación con el comportamiento a fatiga, se han determinado las curvas S-N y los límites de fatiga de cada tipo de material. Adicionalmente, se han realizado ensayos normalizados en probetas compactas para determinar curvas de propagación de grietas y valores umbrales del parámetro de control propuesto en esta tesis, $\Delta\sqrt{G}$. Toda esta información se ha agrupado en diagramas del tipo Kitawaga-Takahashi, extendiéndolos a los casos de vida finita y rotura inestable.

Resultados

Los resultados evidenciaron que, independientemente del tipo de caracterización, el peor comportamiento mecánico y a fatiga corresponde a las probetas *SLS* ensayadas aplicando la fuerza perpendicularmente a la orientación de las capas. Los defectos inducidos durante el procesado y una resistencia interlaminar baja justificaron este comportamiento.

Finalmente, se ha identificado la nucleación, coalescencia y crecimiento de *crazes* como el mecanismo dominante en la mayoría de los casos. Su origen suele localizarse en defectos internos asociados al proceso de fabricación o a la propia fase cristalina. En algún caso, también se han detectado mecanismos de desgarro dúctil.

Conclusiones

Como conclusión global, los resultados obtenidos en esta tesis indican que el comportamiento a fatiga de la PA-12 fabricada mediante *SLS* es bastante similar al de la PA-12 fabricada mediante *IM*, un buen punto de partida para incorporar piezas fabricadas mediante *SLS* en aplicaciones estructurales.

ABSTRACT

In this doctoral thesis, the fatigue behavior of polyamide 12 manufactured by selective laser sintering (*SLS*) is studied and compared with the same material processed by injection moulding (*IM*). An extensive experimental program has been carried out, providing relevant data on the behaviour of this material to evaluate the structural integrity of the parts processed using additive manufacturing techniques. Since in these techniques the manufacturing process is carried out by layer-by-layer deposition, the resulting parts are susceptible to exhibit a transversely isotropic behaviour. That is the reason why the mechanical and fatigue characterizations were performed applying the force parallel and perpendicular to the layered structure.

Firstly, the most relevant thermal and microstructural properties of this semicrystalline thermoplastic have been determined, including the glass transition temperatures, the degree of crystallinity, the porosity or the size of the spherulites, together with features typically associated with the manufacturing process, such as roughness or skin-core morphology. Some significant differences between the two manufacturing procedures have been

detected, especially in the size of the spherulites and in the surface roughness, both much smaller in the case of *IM* specimens. Moreover, *IM* specimens showed a skin layer of amorphous material.

Regarding the mechanical characterization, tensile tests have been carried out, the results do not show great differences either between the *SLS* and *IM* specimens or between different orientations in the case of the specimens processed by additive manufacturing. The only and very marked difference is the elongation at break, which is significantly lower in the case of samples processed by *SLS*, and within these, in the specimens tested with the load applied perpendicularly to the layer wise structure.

Regarding the fracture behavior, the polyamide has presented a non-linear mechanical response in all cases, which has compelled a characterization based on the integral J. The critical values of this parameter do not show relevant variations either between the materials processed by *SLS* or by *IM*, or between the different orientations tested. Nevertheless, it is worth mentioning that the SLS specimens tested with the load applied parallel to the layered structure showed the best crack propagation resistance and the IM samples presented the highest energy at crack growth initiation.

In relation to the fatigue behavior, the S-N curves and the fatigue limits have been determined using plain specimens. Additionally, fracture mechanics specimens (compact tension configuration) have been employed to obtain crack propagation curves and the threshold values of the crack driving force parameter proposed in this thesis, $\Delta\sqrt{G}$. All this information has been employed for the construction of the Kitawaga-Takahashi diagrams, extended to finite life and unstable failure cases.

The general trend has been that the worst mechanical and fatigue behavior occurred in the *SLS* specimens tested with the load applied perpendicularly to the layered structure. The defects induced during processing together with the weak interlayer strength accounted for this behaviour.

Finally, the dominant mechanisms of failure have been identified, which in most cases are nucleation, coalescence and growth of crazes, which usually have their origin in internal defects associated with the manufacturing process or in the crystalline phase itself. In some cases, ductile tearing has been also detected.

As an overall conclusion, the results obtained in this thesis indicate that the fatigue behaviour of PA-12 manufactured by *SLS* is quite similar to that of PA-12 manufactured by *IM*, a good starting point to incorporate parts processed by *SLS* in structural applications.

ACRONYMS AND SYMBOLS

a	Crack
A	Paris law coefficient
a_0	Initial crack length
a_{bi}	Crack growth with blunting correction
a_f	Final crack length
B	Thickness
B_B	Basquin's equation coefficient
C	Sample's compliance
CDF	Crack Driving Force
C_i	Elastic load-line compliance using the crack length a_{bi}
C_J	Coefficient of J-R power law expression
COD	Crack Opening Displacement
CT	Compact Tension
da/dN	Crack growth rate
$\overline{D}$	Average spherulite diameter
DMA	Dynamic Mechanical Analysis
DSC	Differential Scanning Calorimetry

E	Young's modulus
$f(\alpha)$	Geometrical calibration factor
f_i	Failure at i^{th} stress level
F	Cumulative probability function
$g(\alpha)$	Non-dimensional load line compliance
G_{IC}	Critical value of energy release rate
G_{max}	Maximum energy release rate
G_{min}	Minimum energy release rate
G_Q	Conditional energy release rate
IM	Injection Moulding
$J_{0.2}$	Crack resistance at 0.2mm of the total crack growth
J_{BL}	*J* value from the intersection between *J* curve and the blunting line
J_{IC} / J_C	Critical J-integral value
J_{pl}	Plastic component of J-integral
K_i	Stress intensity factor at i^{th} *load data* P_i
K_{IC}	Fracture toughness or critical stress intensity factor
K_{max}	Maximum stress intensity factor
K_{min}	Minimum stress intensity factor
K_Q	Conditional stress intensity factor
L	Likelihood function
l_0	Characteristic length in El Haddad empirical model
l_0^s	Characteristic length for static response in El Haddad empirical model
LC	Long Cracks regime
LEFM	Linear Elastic Fracture Mechanics
m_B	Basquin's equation exponent

MSC	Microstructurally short cracks regime
n	Paris law exponent
n_T	Total number of stress amplitude levels
N	Number of cycles
N_J	Exponent of the J-R power law expression
NLFM	Non-Linear Fracture Mechanics
$P_{5\%}$	Load resulting from the intersection of the load curve with a straight line with 95% initial stiffness
P_i	Load at iteration i^{th} data point
P_{max}	Maximum load of a cycle
P_{med}	Mean load of a cycle
P_{min}	Minimum load of a cycle
P_{Ni}	Normalized load at iteration i^{th} data point
P_Q	Conditional load at crack growth initiation
PSC	Physically short cracks regime
R-ratio	P_{min} to P_{max} ratio
R_a	Arithmetical mean value of the tested roughness profile
r_i	Run-out at i^{th} stress level
R_z	Maximum peak to valley height of the roughness profile
s	Standard deviation of a normal distribution
S	Stiffness
SEM	Scanning electron microscopy
SENT	Single Edge Notch Tension
SLS	Selective Laser Sintering
T_α	Alpha-transition temperature
T_β	Betha-transition temperature

T_c	Crystallization temperature
T_g	Glass transition temperature
T_m	Melting temperature
U	Normalized compliance
U_i	Area under force-displacement curve until P_i data point
U_Q	Energy to break or energy up to P_Q data point
W	Width
W_{air}	Weight of sample in air
W_{im}	Weight of sample in an immersion medium
α	Crack length, a, to width, W, ratio
δ'_{pli}	Plastic normalized displacement at i^{th} data point
δ_i	Normalized displacement at i^{th} data point
ΔG	Energy release rate amplitude
ΔH_0	Enthalpy of fusion of pure PA-12
ΔH_c	Crystallization enthalpy
ΔH_m	Melting enthalpy
ΔK	Stress intensity factor amplitude
ΔK_{th}	Threshold stress intensity factor
ΔP	Load amplitude of a cycle
$\Delta\sigma$	Applied stress amplitude or stress range
$\Delta\sigma_{Hd}$	Applied stress amplitude in El Haddad empirical model
$\Delta\sigma_{fl}$	Fatigue limit
$\Delta\sqrt{G}$	Crack driving force for fatigue propagation curves
$(\Delta\sqrt{G})_{th}$	Threshold crack driving force for fatigue propagation curves
$(\sqrt{G})_{max,c}$	Maximum crack driving force before break

η	Geometry factor
η_{pl}	Plastic constriction factor
μ	Mean value of a normal distribution
v	crack mouth opening displacement
ρ	Density
ρ_0	Density of the immersion medium
ρ_L	Density of air
σ_{Hd}	Stress by El Haddad empirical model
σ_{max}	Maximum stress of the cycle
σ_{min}	Minimum stress of the cycle
σ_T	Tensile strength
σ_y	Yield stress
φ	Energy calibration factor
χ_c	Crystallinity degree from crystallization peak
χ_m	Melting crystallinity degree

Chapter 1.

Problem statement

Additive manufacturing techniques have marked a milestone due to the innovative nature of the idea compared to traditional manufacturing by subtractive methods and due to its enormous versatility, spreading rapidly to many industrial sectors. Today it is easy to find additive manufacturing applications in very diverse fields, from automotive or aeronautics to biomedical or defence engineering.

Thermoplastic polymers for 3D printing are the most widely used today, but technological evolution has made it possible to employ additive manufacturing techniques in other families of materials such as metals, hydrogels and soft materials of biomedical use, biological tissues or even energetic materials, such as solid propellants and explosives. Within thermoplastic polymers, polyamides (in particular polyamide 12) are one of the most widely used families, both for their thermal properties that facilitate the manufacturing process and for the final mechanical properties obtained.

There are many issues related to the new additive manufacturing techniques that require a great research effort. One of the most relevant issues is the optimisation of the manufacturing parameters to achieve the highest quality and the best performance of the products and components manufactured in this way. However, this is not the research topic of this doctoral thesis, more focused on mechanical behaviour.

From the mechanical point of view, there are some issues that need to advance in knowledge. On the one hand, there is the possible anisotropic response of materials that are characterised by presenting a structure of layers that have been successively deposited. Even supposing that within each layer the behaviour is isotropic, it is quite reasonable to think of different responses in

the direction parallel and perpendicular to the deposition of the material, that is, a transversely isotropic behaviour. On the other hand, the manufacturing process itself is prone to inducing a population of characteristic defects, such as unmolten particles or porosity, which can affect the mechanical response and the integrity of the components manufactured this way, especially in the fracture and fatigue behaviours. It is true that all manufacturing processes can have families of characteristic defects and, therefore, it is necessary to assess the response of additively manufactured materials compared to those manufactured by other techniques.

Many works can be found in the scientific literature that study the mechanical properties of polymers processed via additive manufacturing techniques. The most common is to find results from uniaxial tensile tests and comparative studies on the response of materials manufactured by 3D printing and injection or compression moulding. Studies focused on fracture characterization are scarcer, in line with some difficulties inherent to polymers in applying Fracture Mechanics methodologies: influence of the notch sharpening process, viscoelasticity, etc.

However, where there is a great lack of results is in the response to cycling loads, that is, in the fatigue behaviour. There are several reasons behind this situation in the literature: firstly, the fatigue characterization of polymeric materials is very time-consuming because they have to be tested at low frequencies, usually around one hertz, to avoid thermal damage; secondly, the knowledge of the fatigue behaviour of polymers is far from that achieved in the field of metals because the physical mechanisms responsible of damage nucleation and propagation of fatigue cracks are much less well defined.

This does not mean, obviously, that in the field of metals the response to fatigue is a solved and closed problem. The problem of short cracks continues to be the object of intense study and the need remains open to improve the unified description of short and long cracks, with approaches similar to that proposed by the Kitagawa-Takahashi diagrams. The fatigue behaviour of notched components continues to need solutions, despite the enormous effort made in this field by renowned researchers such as Neuber, Glinka or Lazzarin. Probabilistic approaches are another front that, step by step, is providing increasingly satisfactory results.

In this situation, this doctoral thesis is proposed, which aims to characterise the fatigue behaviour of polyamide 12 manufactured by selective laser sintering and to compare its behaviour with the same material manufactured by injection moulding. The approach is clearly experimental, trying to provide information from a careful testing program that includes uniaxial tensile tests, fracture mechanics tests and fatigue tests in specimens prepared in different orientations with long and short cracks.

Chapter 2.

Introduction

2.1 COVERING NEW INDUSTRY REQUIREMENTS: ADDITIVE MANUFACTURING TECHNIQUES OF POLYMERS

Since the last century, transport industry "moves the world". They are in constant development of lightweight structures for reducing fuel consumption while maintaining safety and comfort standards. There are two typical ways to manage them. On one hand using lighter materials which maintain the performance reached with heavier ones. An example of this evolution can be seen in racing car chassis, which has evolved from steel frames used in the early years of the automotive to aluminium alloys introduced at 1950s, arriving at composite materials and high-performance polymers in use since 1980s. The second way is to modify the design of the structure, which could imply complex designs clearly dependent on the capability of the manufacturing to get the end products. Therefore, this way requires an evolution of the manufacturing processes.

Until about thirty years ago, the manufacturing techniques were classified into two categories. Formative manufacturing which models the material with heat and pressure. It includes techniques as forging, stamping, injection moulding or casting. The second category is subtractive manufacturing, which uses cutting tools to remove material from a blank to achieve the final design. Turning, milling and drilling are some of these techniques. It was not until the early 1980s when the development of a third category of manufacturing processes began: additive manufacturing.

According to ASTM F2792-12a standard definition, additive manufacturing (*AM*) technologies are "a set of processes of joining materials to make objects from 3D model data layer upon layer" [1]. These techniques were thought

initially as rapid prototyping processes which reduce the cost and time during the development stage. Since beginning, they have suffered a speedy development translated in new and better techniques.

The first additive manufacturing technique was stereolithography and it was invented in 1983 by Hideo Kodama in Japan [2]. However, it was not commercialized until 1986. In addition, the selective laser sintering (*SLS*) technology was presented that year and since that time, the evolution of additive manufacturing caused a direct impact on the industry, as is shown in *Figure 2-1* for the aerospace industry [3][4]. *AM* technologies have evolved from obtaining low quality parts, which were used in rapid prototyping, to produce parts with complex geometry in reduced time and with no tooling requirements in different technological and industrial sectors[5]–[7].

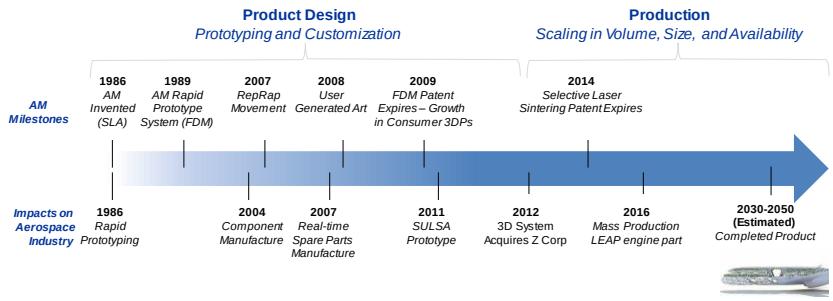

Figure 2-1. Additive manufacturing timeline [1].

According to Wohler's Report, the growth of the *AM* industry, consisting of all *AM* products and services worldwide, has surged from 21% in 2017 to 33.5% in 2018, overcoming nowadays $9.8 billion US [8]. This rising trend is expected to continue during the next years.

A report published recently by SmarTech shows the growing trend of automotive *AM* market for the next decade (*Figure 2-2*). As *Figure 2-2* shows, *AM* market does not consist just in manufacturing final parts. Although this part hoards most of the production, *AM* techniques are also used for prototyping and producing specific tools. This figure also shows the general material trend: the *AM* techniques are focused on polymeric materials, whose final properties could be obtained directly in the manufacturing process in contrast with metallic, ceramic and composite materials, which obtain their final properties after a secondary process such as sintering or infiltration [9]. Volkswagen and The Royal Netherlands air force are two examples of the use of *AM* tools made of polymer on their processes, saving time and cost [10], [11]. Total automotive *AM* market is estimated to reach $12.4 billion US in revenues by 2028 [12]. In addition, considering the development of these techniques, revenues of fabrication of final parts is thought to surpass the revenues of prototyping, tooling and hardware.

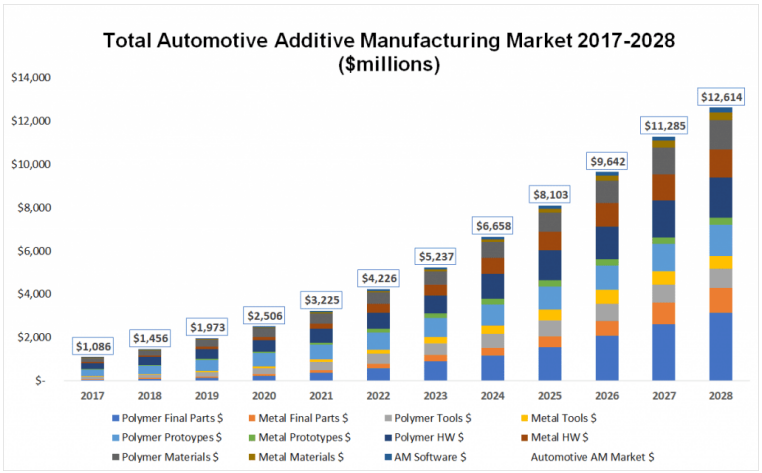

Figure 2-2. Estimation of total automotive AM market for the next decade. [2]

For this reason, the principal automotive Original Equipment Manufacturers, *OEMs*, cooperate with *AM* hardware producers to integrate this technology in their processes.

On the other hand, it is important to know the level of competitiveness of these techniques. *Figure 2-3* shows how unitary cost of a general part varies depending on the manufacturing process chosen. In economic terms, formative manufacturing is the most cost-effective way for manufacturing high number of parts, being followed by the subtractive processes. For these two manufacturing ways, higher number of parts implies lower cost per unit, while the unitary price for additive manufacturing remains constant without relying on the number of manufactured pieces. Thus, *AM* takes a key role when a short number of parts is required or when the geometry of the part is complicated or impossible to obtain with the traditional techniques. However, there are other limiting factors for choosing *AM*, like the mechanical behaviour of *AM* pieces or processing times.

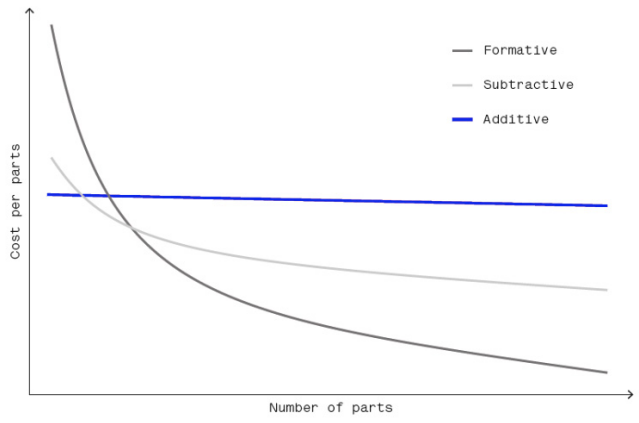

Figure 2-3. Unit cost comparison between formative, subtractive and additive manufacturing. [3]

Despite the general point of view, *AM* is not only linked with industry. There are some relevant events which help to popularize *AM* outside the industry (*Figure 2-1*). Among others, the RepRap project that began in 2005, whose aim was to develop a low-cost 3D printer capable to print its own parts, and the expiration of the Fuse Deposition Modelling (*FDM*) patent in 2009, helped the development of desktop 3D printers. Wohler's Report informs that more than 500.000 desktop 3D printers have been sold between 2015 and 2017 [8].

There are several common steps in all the wide variety of *AM* techniques: all of them begin with the creation of a 3D file by Computer Aided Design (*CAD*) which contains the desired part. This file is converted into a simplified computer-readable format file compatible with the *AM* equipment. Once this Stereolithography (*STL*) file is obtained, it is divided by the software into slices of specific thickness, which gives to the *AM* equipment the manufacturing information of each layer of the part. Then, the *AM* equipment can start with the manufacture of the piece layer by layer until the piece is completed. When the part is finished, it is removed from the machine and usually subjected to post-processing procedures to improve the final quality of the piece [13]. This general procedure is summarized in *Figure 2-4*.

Despite these general steps, ASTM F2792-12a [1] separates *AM* technologies in different categories according to the raw polymer used and the processing method. The most important ones are contained in *Figure 2-5* [14]–[16]. In VAT techniques, a photopolymer resin is used and selectively cured with ultraviolet (*UV*) light, so they are limited to very specific polymers.

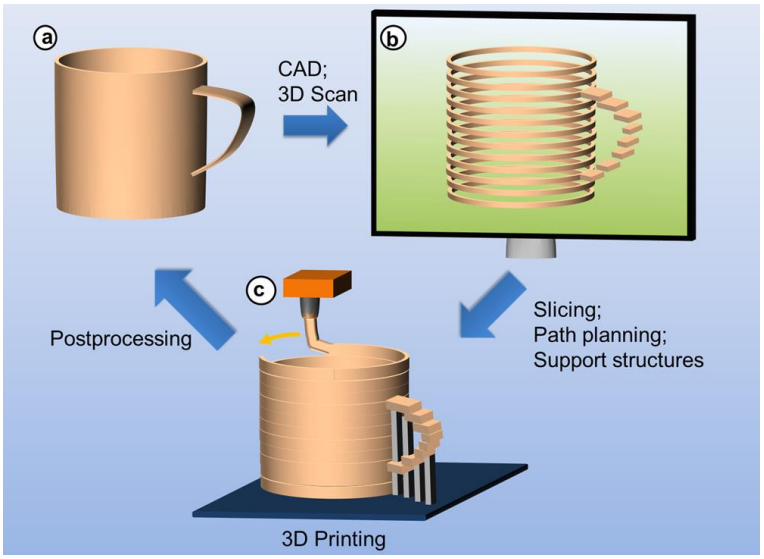

Figure 2-4. General steps of AM processes: (a) creating a CAD file from an idea or scanning a piece, (b) converting it in a STL file and slice the piece in layers, (c) manufacturing process, removal of the piece and optional postprocessing [15].

In the case of material extrusion, the polymer is melted or semimelted and is selectively dispensed with a nozzle. The raw material for powder bed fusion and for material and binder jetting is a powder bed of polymer, with the difference that in jetting processes a binder moves across the layers forming the final part, and in the powder bed fusion, the melted polymer links layer by layer creating the entire piece. This possibility of using just the material powder without any addition, the varieties of suitable powders, the no need for structural support, the excess powder recyclability and the low-cost quality of the parts, make powder bed fusion processes the most popular and applied *AM* technique [8], [16]. Among the powder bed fusion systems, the Selective Laser Sintering (*SLS*) is the most firmly established technique for polymers.

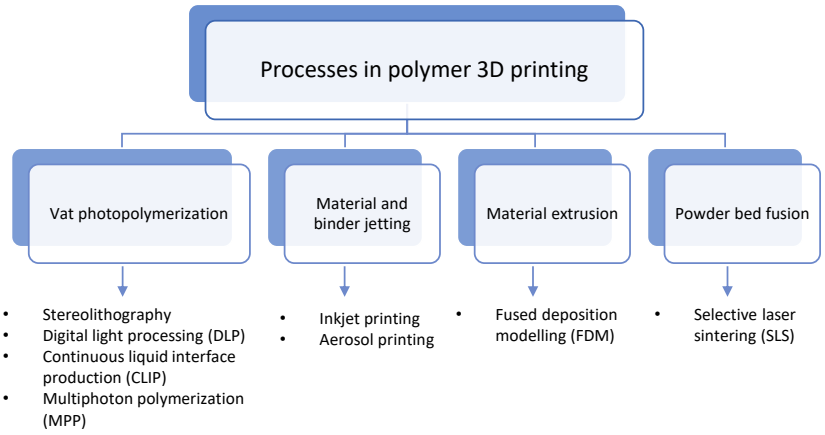

Figure 2-5. Principal 3D printing processes with polymers.

2.2 SELECTIVE LASER SINTERING OF POLYMERS

Selective Laser Sintering (*SLS*) is one of the *AM* processes which has evolved the most during the last decade. This technique allows building polymeric parts with mechanical properties very close to those obtained from specimens processed by conventional manufacturing processes such as injection moulding [8], [12], [13], [16]. This process is presented schematically in *Figure 2-6*. It begins when a thin layer of powder, preheated somewhat below the melting temperature, is spread in the building area positioned in an elevated temperature chamber. A high power laser (CO_2) beam scans the surface of the powders following a 3D computer model pattern. The energy applied by the laser melts and fuses small powder particles upon contact, which finish adhering the previous sintered layer. When a layer is finished, another fresh layer of powder is swept along the build platform which moves downwards a pre-set amount, commonly one layer thickness. The next layer is traced out

and the process repeats layer by layer till the model is fully grown. The unsintered powder remains during the process to support the piece.

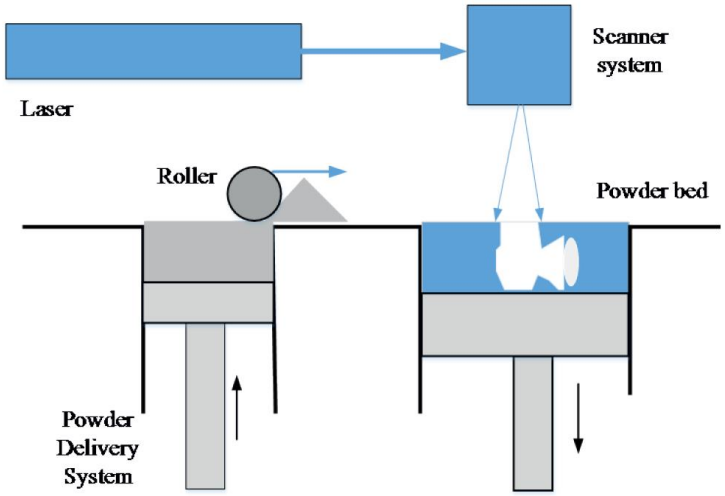

Figure 2-6. Selective laser sintering (SLS) process [17].

This technique can generate high quality and complex 3D parts using the major variety of materials of all the *AM* processes. However, this variety of polymeric powders is limited due to the requirements that have to be fulfilled. *Figure 2-7* contains representative thermoplastics, indicating their *SLS* availability, their microstructure and their mechanical performance. They are divided into three groups: commodity polymers, which are not suitable for structural applications; engineering polymers, which have good mechanical properties; and finally, high performance polymers, usually are used in very demanding tasks like in aerospace industry [18].

The polymeric powders must accomplish some requirements to be used in the *SLS* process. Schmid et al. [19] defined five main aspects, divided into intrinsic (thermal, optical and rheological) and extrinsic properties (particle and powder).

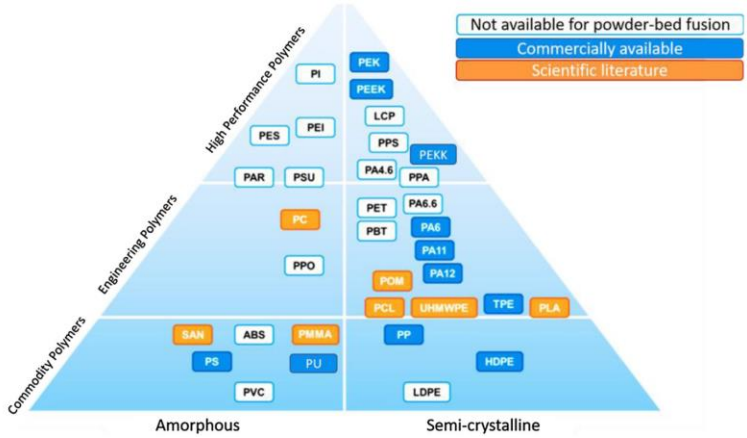

Figure 2-7. Characteristic thermoplastic polymers available for SLS process [18].

The intrinsic properties are defined by the molecular structure of the polymer, which cannot be usually modified. Thermal properties are one of the most crucial factors because *SLS* aims to obtain a full coalescence of the polymeric particles when the CO_2 laser melts selectively the powder. Therefore, temperature during sintering (T_s) must be precisely controlled and optimized attending to material thermal properties. For semi-crystalline polymers, T_s must be chosen attending to the crystallization temperature (T_c) and the melting temperature (T_m). T_s should be higher but near T_c to maintain the crystallization rate as slow as possible, at least few sintered layers, to avoid residual stresses and warping of the piece. On the other hand, T_s must be lower than T_m for keeping dimensional resolution. With these requirements, the temperature range between T_c and T_m could be defined as the *sintering window* as is outlined in *Figure 2-8*. Although this figure shows the sintering window obtained from the Differential Scanning Calorimetry (*DSC*), the practice one in *SLS* is narrowed due to the difficult control of heating and cooling temperatures during processing [19], [20].

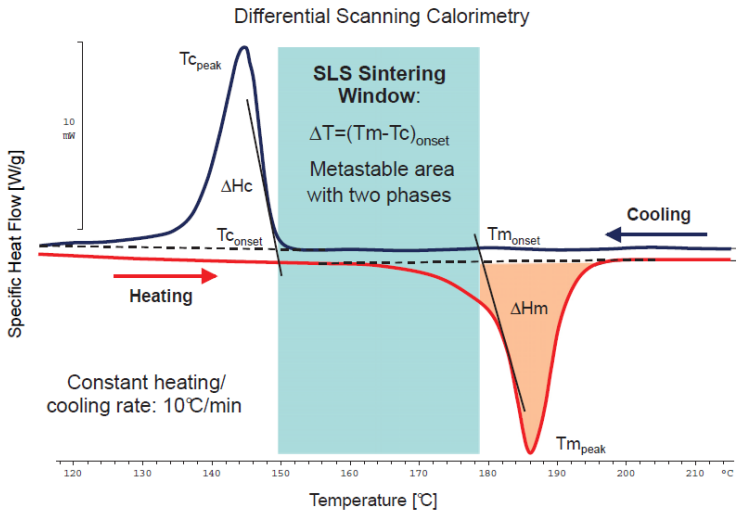

Figure 2-8. Differential Scanning Calorimetry Thermograph with SLS sintering window [19].

Other important point of the thermal properties is the resistance to thermal degradation. The exposition of the polymeric powders to temperatures near T_c during long periods of time results in ageing. So, the powder used in one sintering process that remains unmolten cannot be used directly in other sintering processes. It has to be mixed with new powder up to 50 %wt [21].

Other intrinsic factors are the viscosity and the surface tension, which must be kept as low as possible to attain full dense parts. Otherwise, a complete coalescence of polymeric particles is not produced during sintering, obtaining parts with reduced mechanical properties. Due to the low viscosity requirement, *SLS* of amorphous polymers, whose viscosity maintains high values above the glass transition temperature (T_g), are not widespread used because of the poor coalescence during sintering, resulting in brittle materials.

Optical properties are also of some concern as the material must have the ability to absorb the energy provided by the CO_2 laser used in *SLS* (wavelength

of 10.6 µm). Most polymers consist of aliphatic compounds (C-H) in their molecules, which can absorb relevant portions of the laser radiation.

On the other hand, the extrinsic factors are the ones which can be modified attending to the powder production procedures. One of these factors is related with the shape of particles. To obtain an optimum powder flow and slip between particles in the processing bed, the best particle geometry is spherical. In addition, a smooth surface of the particle also improves the flow and the final roughness of the piece [22]. Commercial powders are not usually spherical due to the manufacturing process, showing irregular shapes. Also, the particle size distribution of the powder is important. To improve the flowability of the powder, it is important to have particles of different sizes. If the powder is composed of particles with the same size, the slip between particles in the bed is difficult. When particles are too small, an excessive adhesion between particles also reduces the flowability. A commercial distribution usually has a particle size distribution between 20 µm and 80 µm and a low percentage of particles with size below 10 µm [22]. The porosity of the sintered piece is reduced optimizing both factors.

In addition to the thermoplastics contained in *Figure 2-7*, Ligon et al. [23] registered 31 different commercial powders on their work in 2017 including the recently added thermoplastic elastomers. They summarized the mechanical properties of those materials in a stiffness/toughness balance diagram which is shown in *Figure 2-9*. Although this number has increased, there are just a few material suppliers and most of those materials are made by 3D Systems, Electro Optical Solutions (*EOS*) or Advanced Laser Materials. For this reason, the different materials have their origin in one of these

companies and they can be mainly divided into thermoplastics and thermoplastic elastomers.

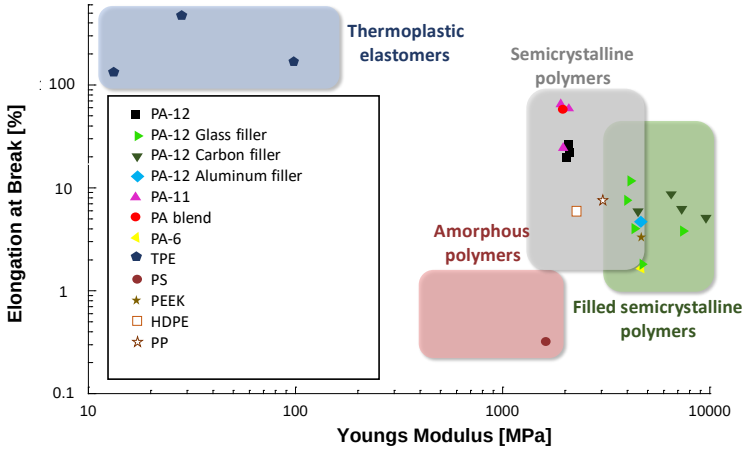

Figure 2-9. Stiffness/Toughness balance diagram of commercial SLS materials by Ligon et al.[23]

Despite this variety, Polyamide (PA)-based thermoplastic are the most used polymers in *SLS* with 95% market share of total *SLS* manufacturing [18], [23], [24]. Polyamide 11 (PA-11) and Polyamide 12 (PA-12) are semi-crystalline thermoplastics which fulfil all the critical requirements previously mentioned. Moreover, PA-12 has high mechanical properties, high toughness and high fatigue resistance compared to other thermoplastics, good tribological performance and high chemical resistance [25], [26]. *Figure 2-9* shows the prevalence of these polymers when high stiffness is needed. Different types of PA-11 (Primepart DC, EOS GmbH) and PA-12 (PA2200 by EOS GmbH, Duraform® by 3D systems or PA 250 by ALM) stand out against others. This figure also included PAs with inorganic fillers added for increasing mechanical properties, resulting in higher strength and thermal stability but lower elongation at break. Some of the used fillers are glass beads, alumina, aluminium particles, carbon and carbon nanotubes and titanium whiskers [23].

Although PA-11 is cheaper than PA-12 and provide parts with higher ductility, it is more difficult to process due to its narrower sintering window and a fast recrystallization and degradation during preheating processes, giving as result poor accuracy and higher geometrical distortions in the pieces [18], [27]. For these manufacturing difficulties, PA-12 and PA-12 composites take the majority of the *SLS* market [8], [23], [24].

2.2.1 Mechanical properties of PA-12 processed via Selective Laser Sintering

The mechanical performance of PA-12 processed by *SLS* has been evaluated mainly by tensile tests and fracture toughness tests. *Table 2-1* collects the tensile properties such as the ultimate tensile strength, the elongation at break and the Young´s modulus of *SLS* PA-12 measured by different authors. The processing parameters, when provided by the authors, are also included, as the mechanical performance is strongly dependent on the resulting microstructure which is governed by the values of the fabrication parameters. The table also incorporates the values given by the two main manufactures of PA-12 for *SLS* as PA 2200 by EOS [28] and DuraForm PA [29], as well as those obtained from the conventional technique as injection moulding (*IM*). In general trends, the values of the tensile strength and the Young´s modulus of *SLS* PA-12 are very similar to those of *IM* PA-12, except for the elongation at break. In this case, the elongation at break of *IM* PA-12 is almost one order of magnitude higher than that of *SLS* PA-12. The main factors behind these differences are the processing parameters that control the *SLS* technique, the intrinsic anisotropy of the layer wise *SLS* manufacturing process or the hygroscopic nature of the polyamide.

Table 2-1. Ultimate tensile strength, elongation at break and Young's modulus of PA-12 processed by SLS and IM by different authors. The processing parameters and a sum up of the main results of the investigation are included.

		Processing parameters	Ultimate tensile strength (MPa)	Elongation at break (%)	Young's Modulus (MPa)
Selective Laser Sintering (SLS)	PA 2200 EOS [28]	-	48	18	1650
	DuraForm PA [29]	-	43	14	1586
	Hooreweder et al. [30]	· PA2200 · EOS P730 · Energy density: 0.031 J/mm^2 · Layer height: 120 µm · Building chamber: 170 °C	49 – 52	4 – 7	2080 - 2158
	Seltzer et al. [31]	· Duraform 3D Systems	23-13 (dry-wet)	10-5 (dry-wet)	1720-1170 (dry-wet)
	Goodridge et al. [32]	· Duraform 3D Systems · Laser Power: 11 W · Layer height: 100 µm · Building chamber: 142 °C	45-40 (dry-wet)	8-15 (dry-wet)	2000-1500 (dry-wet)

Selective Laser Sintering (SLS)	Caulfield et al. [33]	· Duraform 3D Systems · DTM Sinterstation 2500plus · Laser Power: 6-21 W · Laser energy density: 0.008-0.028 J/mm^2 · Layer height: 150 μm	12 – 53	4 - 18	500 - 1100
	Stichel et al. [34]	· 6 paramater protocol for 6 different commercial machines	22 – 45	2 – 32	-
	Starr et al. [35]	· DTM Sinterstation 2500plus · Building chamber: 166 °C · Energy density: 0.08-0.63 J/mm^2	50.7 – 52.9	12.2 – 16.5	-
	Lammens et al. [36]	· PA2200 · EOS P395 machine	45.96 – 56.95	3.6 – 15.46	1832 - 2104

Injection moulding (IM)	Hooreweder et al. [30]	· PA2200 EOS granules · ES200/35 HL machine · Mould temperature: 60 °C · Holding time: 3 s · Injection speed: 60 mm/s · Injection pressure: 50 bar · Nose temperature: 230 °C · Melt injected at 240 °C	53	97	1701
	Goodridge et al. [32]	· Grilamid L20G · EMS-Grivory	40-30 (dry-wet)	8-20 (dry-wet)	1800-700 (Dry-wet)

Among the manufacturing parameters of the *SLS* technique, the supplied energy density (dependent on the laser power, laser scan spacing, laser beam displacement velocity and laser radius) has shown a great impact on the microstructure and crystalline features and consequently, on the mechanical performance of *SLS* PA-12. Dupin et al. [37] showed that the increase in the energy density decreases the porosity and nascent polyamide particles and increases the recrystallized fraction, implying higher mechanical properties. Similar results were obtained by Caulfield et al. [33] and by Stichel et al. [34].

The latter evaluated the tensile parameters of PA-12 sintered by different machines and then, different parameter sets optimum for the respective machine.

Another relevant factor is the intrinsic anisotropy induced by the stacking layer *SLS* process and there are many authors that have evaluated the mechanical response as a function of the applied load direction with respect to the layered structure. Hooreweder et al. [30] compared the tensile results of PA-12 manufactured by *SLS* obtained when the applied load was applied along the scanning direction and perpendicular to the scanning direction with the results obtained from *IM* PA-12. For *SLS* parts, the main difference between the two orientations was found in the elongation at break which was lower when the load was applied perpendicularly to the layered structure. Regarding the effect of the manufacturing technique, the *SLS* specimens showed a more brittle behaviour than *IM* but higher Young's modulus. The same trend was obtained by Caulfield et al. [33], Stichel et al. [34] and Lammens et al. [36].The latter also analysed the effect of the different machine cross-head displacement rates (5, 50 and 500 mm/min) on the tensile properties, registering higher stiffness at higher displacement rates accompanied with lower elongation at break. On the other hand, the results obtained by Starr et al. [35], which tested six different orientations, revealed small differences in the mechanical properties among the distinct orientations, although the lower elongation at break was also found when the load was applied perpendicularly. In all the cases, the low elongation at break along the building direction was related to layer adhesion, very sensitive to process conditions. Some authors have analysed the effect of the hygroscopic nature of the *SLS* PA-12 on the mechanical performance. Seltzer et al. [31] studied the effect of humidity on *SLS* PA-12, obtaining an

adverse effect of the hydrothermal aging on the mechanical properties, specifically, for water saturated specimens, with a reduction in strength, in the Young's modulus, and in ductility. Similar results were obtained by Goodridge et al. [32] in their study comparing the effect of the storage conditions and length of time of *SLS* PA-12 and *IM* PA-12, except for the elongation at break which in water conditioned samples presented higher values than those of the dry specimens. In addition to the detrimental effect of humidity in PA-12, the *SLS* PA-12 showed better water resistance than *IM* PA-12. Besides, tensile testing at temperatures that ranged from -40 °C to 140 °C were performed on specimens with distinct humidity conditions and in all the cases, *SLS* samples held the strength better than *IM* specimens.

The research on the fracture behaviour of *SLS* PA-12 using the Fracture Mechanics approaches are not so prolific as those dealing with the tensile properties. *Table 2-2* collects some of the most representative works found in the literature addressing the influence of different factors, such as the anisotropy due to the layered structure, the hygroscopic nature of polyamides or the processing parameters, on the fracture toughness of PA-12. Together with the values of the fracture parameters in terms of the mode I critical stress intensity factor, K_{IC}, or the energy at crack growth initiation, J_{IC}, the values of the manufacturing parameters are also included as their knowledge can shed more light on the results. Hitt et al. [38] compared the fracture behaviour of *SLS* and *IM* PA-12 parts as a function of the specimen thickness. The results were in contradiction in the sense that while for *IM* specimens, the energy at crack growth initiation decreased as the specimen thickness increased, the opposite trend occurred for *SLS* samples. The reason of this anomaly could be in the computation of the fracture parameters through the Linear Elastic

Fracture Mechanics (LEFM) approach, despite the well-defined non-linear behaviour shown by the materials. Seltzer et al. [31] analysed the effect of water conditioning on the fracture behaviour of neat PA-12 and PA-12 composites reinforced with glass beads and short ceramic fibres. The reinforcement implied both a better fracture behaviour and a better water resistance. Salazar et al. [39], [40] investigated the effect of the temperature (23 °C and -50 °C) and the hygrothermal ageing on the fracture toughness of neat PA-12 and PA-12 filled with short ceramic fibres. In the case of the neat PA-12, the fracture toughness was not affected by the testing temperature but in case of the composite, the fracture toughness values at -50 °C were higher than at room temperature. In the specimens saturated in water, the fracture toughness showed an important impoverishment of up to 50%. Brugo et al. [41] evaluated the influence of the notch sharpening method and of the load direction with respect to the building direction. Regarding the notching technique, no differences on the fracture toughness values were obtained between the specimens notched by pressing a razor blade into the notch and those with a 0.3 mm in thickness notch generated during the *SLS* manufacturing process. Nevertheless, none of these techniques provided a sharp crack with no damage at the crack front which guaranteed quality fracture toughness values [42], [43]. In case of evaluating the orientation, the fracture toughness of the specimens loaded perpendicularly to the layers was lower than when the load was applied along the layers.

Table 2-2. Compilations of fracture toughness parameters in terms of critical stress intensity factor, K_{IC}, and the energy at crack growth initiation, J_{IC}, of PA-12 processed by SLS and IM obtained by several authors. The processing parameters and the testing conditions are included (SENB: Single Edge Notch Bend, CT: Compact Tension, SENT: Single Edge Notch Tension, DENT: Double Edge Notch Tension, DCB: Double Cantilever Beam).

		Processing parameters	**Testing conditions**	**K_{IC} (MPa·m$^{1/2}$)**	**J_{IC} (kJ/m^2)**
Selective Laser Sintering (SLS)	Hitt et al. [38]	· PA2200 · EOS Formiga P100 · Power: 21 W · Laser scan: 2.5 m/s · Layer height: 250 μm · Building chamber: 172 °C	· (SENB)	-	2.9 - 4.3
	Brugo et al. [41]	· PA2200 · EOS Formiga P100 · Power: 21 W · Laser scan: 2.5 m/s · Layer height: 100 μm · Building chamber: 172 °C	·(CT) · Load parallel to the layers	4.5 - 4.8	-
			· (CT) · Load perpendicular to the layers	3.3 - 4.0	-
	Seltzer et al. [31]	· Duraform 3D Systems	· (SENB) · Dry	3.00 ± 0.05 (PA-12) 3.6 ± 0.1 (25wt% short fibers) 3.40 ± 0.04 (43wt% glass beads)	-
			· (SENB)	0.70 ± 0.05 (PA-12)	-

			· Saturated in water	2.6 ± 0.1 (25wt% short fibers) 2..6 ± 0.2 (43wt% glass beads)	
	Salazar et al. [39], [40]	· Duraform 3D Systems	· (CT) · Dry at 23 °C	3.2 ± 1.2	-
			· (CT) · Dry at -50 °C	2.7 ± 0.2	-
			· (CT) · Saturated in water at 23 °C	1.3 ± 0.2	-
	Crespo et al. [44], [45]	· PA2200 · EOS Formiga P100	· (SENT) · Load parallel to the layers	3.2 ± 0.3 (2 mm/min) 2.1 ($5 \cdot 10^5$ mm/min)	-
			· (SENT) · Load perpendicular to the layers	2.4 ± 0.2 (2 mm/min)	-
Selective Laser Sintering (SLS)	Linul et al.[46]	· PA2200 · Power: 21-25 W · Laser scan: 1.5-2.5 m/s · Layer height: 150 μm · Building chamber: 170 °C	· (SENB) · Load perpendicular to the layers	2.282 (25 W, 1.5 m/s)	-
			· (SENB) · Load parallel to the layers	1.098 (25 W, 1.5 m/s)	-
	Schneider and Kumar [47]	· Duraform 3D Systems · Power: 2.8 W · Laser scan: $4 \cdot 10^4$ points /s · Layer height: 100 μm · Building chamber: 147 °C	· (DENT) · Load parallel to the layers	4.1 ± 0.5	-
			· (DENT) · Load perpendicular to the layers	4.2 ± 0.6	-

Selective Laser Sintering (SLS)	Stoia et al. [48]	· PA2200 · EOS Formiga P100 · Power: 25W · Laser scan: 1.5 mm/s · Layer height: 250 μm · Building chamber: 171 °C	· (DCB) · Load parallel to the layers	2.3 ± 0.1	-
			· (DCB) · Load perpendicular to the layers	0.9 ± 0.1	-
Injection Moulding (IM)	Hitt et al. [38]	· Rilsan AMNO PA12 pellets · Negri-Bossi NB62 machine · Mould temperature: 40 °C · Melt injected at 240 °C	· SENB	-	2.9-4.3

The effect of the load direction with respect to the layered structure on the fracture parameters of *SLS* PA-12 was also studied by Crespo et al [44], [45], Linul et al. [46], Schneider and Kumar [47] and Stoia et al. [48]. The former inferred the fracture toughness from the fracture of notched samples through the application of the theory of the critical distances. The fracture toughness of the specimens loaded parallel to the layered structure was also higher than for the specimens loaded perpendicularly. The same authors [44], [45] analysed the influence of the strain rate on the fracture toughness following the same methodology, carrying out tests that ranged from quasi-static conditions in electromechanical machines to very high strain rates attained by Hopkinson bar tests. On the other hand, Linul et al. [46] inspected the effect of the process energy density on the mode I and mode II fracture toughness

evaluated on specimens loaded at different directions with respect to the layered structure. As expected, the fracture behaviour of the specimens processed with higher applied energy and loaded parallel to the layered structure was the best, unequivocal sign that the higher applied energy implied higher density and consequently, less defects. Moreover, the interlayer adhesion is still a limiting factor as the authors observed the crack growth tended to occur along the layer bonding interface. Schneider and Kumar [47] determined under plane stress conditions the fracture toughness as a function of the load direction with respect to the layered structure, finding no relevant differences between the parallel and perpendicular orientations. Finally, Stoia et al. [48] studied the effect of the geometrical defects introduced during sintering as well as the load direction on the fracture toughness. In case of defect-free specimens, there was an important anisotropy in the fracture toughness, with values of the specimens tested with the load applied perpendicular to the building direction more than twice those obtained from tests with the load applied along the building direction.

2.3 FATIGUE OF POLYMERS

2.3.1 Fatigue Failures

The fatigue performance of polymers due to cyclic mechanical loads is commonly characterized by the stress-life or the S-N curves [49]. The approaches established for metals have been used to define the mechanisms of fatigue initiation [50] and crack growth [51] in polymers. The reason is that the majority of fatigue data of stress-life curves and fatigue crack growth curves of polymeric materials appear significantly similar in shape to those

found in metals, despite their different microstructure and chemical makeup. At present, there is no physical theory to explain the mechanical S-N behaviour of polymers. Notwithstanding, the S-N curves, where the cyclic stress amplitude is plotted versus the failure cycles, are fitted to Basquin´s empirical equation [52], useful for engineering practice although this empirical relationship does not represent well the entire fatigue data range.

Fatigue failure in polymers can occur by thermal fatigue or by mechanical fatigue [53]. In the former, failures occur by thermal softening and melting due to massive hysteretic heating while in the latter, fatigue crack initiation and stable crack propagation to fracture take place similarly to metals.

Thermal fatigue failure normally occurs due to extrinsic factors such as relatively high loading frequencies or strain rates, where thermal softening due to hysteretic heating arises from the viscoelasticity, high damping and low conductivity typical in polymers [54]–[56]. The hysteretic energy is dissipated as heat producing a rise in specimen temperature [57] and, consequently, loss of stiffness [58]–[60]. The temperature rise is very dependent on the frequency because the hysteresis arises from the phase lag between stresses and strains in the polymer, which is larger as the loading frequency is higher.

As a rule, the influence of test frequency on the fatigue response of polymers originates from the viscoelastic behaviour of polymers. An increase in frequency normally involves a greater energy dissipation and temperature rise. Nevertheless, in low frequency test conditions where thermal effects are not crucial, an increase in frequency leads to increase in modulus and strength due to increased strain rate, implying an increased fatigue life as observed in Polypropylene (PP) and Polypropylene reinforced with short glass fiber by

Eftekhari and Fatemi [60] and in Polystyrene (PS), High Impact Polystyrene (HIPS) and Acrylonitrile Butadiene Styrene (ABS) by Sauer and Chen [61].

In fatigue crack growth behaviour of polymers, the thermal effects are localized at the crack tip, leading to crack tip blunting and consequently, increasing the fatigue resistance to crack growth. These effects were observed in PS [62], Polymethyl Methacrylate (PMMA) [63] and Polyvinyl Chloride (PVC) [64] but not in Nylon [65] and Polycarbonate (PC) [64] in which the crack growth curves were independent of frequency in studies performed in the range from 1 Hz to 100 Hz. Nevertheless, in these studies the crack growth behaviour was correlated on the basis of Linear Elastic Fracture Mechanics (*LEFM*) approach, using as control parameter the stress intensity factor range, ΔK, even at frequency up to 100 Hz, doubtful parameter if excessive thermal softening occurs.

Regarding mechanical fatigue failure, Sauer and Richardson [51] stated that true mechanical fatigue failure, involving initiation and growth of fatigue crack under cyclic loading takes place in the range between one-fourth and one-half of the yield strength of the polymer. The macroscopic description of fatigue fracture in polymers is formed by the sequence of mechanical events similar to those in metals [49]–[51], [66], [67]. In glassy polymers, the initiation occurs by the development of a single craze at some surface location while in semicrystalline polymers, it takes place at spherulite boundaries after some fatigue cycles. Thereafter a fatigue crack is generated within the craze, by cyclic fracturing the fibrils farthest from the initial craze tip, and the advancement of the macroscopic crack growth, either continuously or discontinuously under cyclic loading, till the point of rupture is not any different in glassy or

semicrystalline polymers. Purely mechanical fatigue failures normally occur in the absence of thermal effects, that is, at low frequency conditions.

Finally, fatigue behaviour of polymers is also influenced by the environmental temperature because some polymers undergo crystallization or brittle-ductile transition as the temperature is increased [49]–[51], [66], [67]. The fatigue resistance is reduced with increased temperature due to alteration of the crack tip deformation and fracture mechanisms [25], [68]–[70], the reduction of the tensile strength and the fatigue limit as the test temperature is increased [25], [60], [67], [71] or the temperature-dependent variation on the viscoelastic deformation of the polymer [25], [60], [72].

2.3.2 Difficulties in fatigue characterization

The proofs provided by the literature allows the use of the continuum fatigue behaviour tools of metals for describing the mechanical fatigue response of polymers. The S-N curves obtained under mechanical fatigue conditions usually exhibit the asymptotic approach toward the tensile strength at one fatigue cycle and the asymptotic flattening at the fatigue limit (the physical stress limit below which no fatigue failure occurs), as in the case of metals. Nevertheless, there are some gaps or difficulties in the fatigue characterization of polymers. In case of the stress-life, there is not an accepted physical theory capable of constructing the shape of the S-N curves. Some attempts were made by Baltenneck et al. [73], who derived a kinetic S-N curve based on the cumulative evolution of micro-defects till the point of fatigue rupture. The predicted curves agreed partly well with the experimental ones despite the physical basis assumed that the number of cycles to failure increased with initial defect concentration. Williams et al. [74] developed an equation for

fatigue crack growth life considering a fatigue crack growing to reach the point of unstable failure. Although it predicted fatigue lives reasonably well, some parameters were chosen arbitrarily and was not applied to describe S-N curves of plain specimens. Shojaei and. Wedgewood [67] developed a model within the Continuum Damage Mechanics framework to enhance the life prediction capabilities of polymers. Considering that in the Low Cycle Fatigue regime, damage can be modelled by microvoid nucleation and propagation and that in High Cycle Fatigue regime, damage can be described by initiation and propagation of microcracks, plasticity and creep laws were coupled in fatigue Finite Element Analysis. Although the results were promising, the computation cost and the update of the damage fatigue history was an important difficulty. The most elaborate theory is that of Ravi Chandran [25] who, in the absence of thermal effects and starting from the macroscopic crack growth mechanisms, derived a continuum-based fatigue theory capable of predicting the effect of the mean stress and the temperature on the shape of S-N curves significantly well. He developed the constitutive equation for polymer fatigue assuming that the increase in stress in the uncracked ligament is responsible for the acceleration of the crack growth during fatigue, consistent with the experimental findings in metals of Frost, Dugdale and Weibull [75]–[77], whose works predate that of Paris [78]. However, more experiments with controlled changes in the structural and microstructural parameters as well as in the mechanical properties of polymers are needed to fully validate the proposed theory.

Regarding the fatigue crack growth behaviour of both glassy and semicrystalline polymers, *LEFM* approach has been mostly used to describe the crack growth rate as a function of the stress intensity factor range, $\Delta K =$

$K_{max} - K_{min}$ [49], [79]–[86]. However, some works have questioned the validity of ΔK when dealing with the R-ratio effect [50], [87]–[94]. Rink et al. [92], Furmanski and Pruitt [93] and Boonyaookana et al. [94] observed that the crack growth propagation curves seemed to be unaffected by R-ratio when the crack growth rate was correlated with K_{max}. In contrast, Takemori [50] and Radon [89] showed an uncommon trend as the decrease in the crack growth rate, $\frac{da}{dN}$, with the increase in the R-ratio when using either ΔK or K_{max} as crack driving parameters. This fact motivated the choice of energy release rate range, ΔG, [88], [95], [96] or the maximum energy release rate, G_{max} [97] as the crack driving force when brittle crack growth propagation was observed. Particularly, Sutton [88] employed ΔG in the analysis of fatigue crack growth propagation in epoxy polymers achieving the collapse onto one single master curve of the fatigue crack growing data obtained at different R-ratios. However, he also realized that this behaviour could not be extrapolated to all polymers.

The uncertainties on the predominant process involved at different R-ratios in polymers has driven to some researchers to consider two different crack driving forces to describe the fatigue crack growth rate as a function of the mean stress, applying the crack closure concept introduced by Elber [98] at low *R-ratio* and taking into account the creep process that seems to occur at high *R-ratios* [87], [89], [91], [93].

Cano et al. [99] proved the validity of $\Delta\sqrt{G} = \sqrt{G_{max}} - \sqrt{G_{min}}$, with G_{max} as the maximum energy release rate and G_{min} as the minimum energy release rate, as a valid similitude parameter for describing the crack growth behavior

of glassy polymers, overhauling the gaps previously mentioned. $\Delta\sqrt{G}$ relies on the same basis for similitude as ΔK, and is defined as:

$$\Delta\sqrt{G} = \sqrt{G_{max}} - \sqrt{G_{min}} = \Delta P \sqrt{\frac{1}{2B}\frac{dC}{da}} \qquad (2\text{-}1)$$

where ΔP is the amplitude load of the cycle, B is the specimen´s thickness, C is the sample´s compliance and a is the crack length. Therefore, the crack growth rate, $\frac{da}{dN}$, was correlated with this similitude parameter through a Paris-type relationship:

$$\frac{da}{dN} = A\left(\Delta\sqrt{G}\right)^n \qquad (2\text{-}2)$$

with N the number of elapsed cycles and A and n material´s constants.

$\Delta\sqrt{G}$ parameter was proposed by Rans et al. [100] for adhesive joints and composites. The difficulty in the fatigue crack growth behaviour of these materials was that ΔK describes locally the stress field and this makes it unsuitable in fibre-reinforced polymer matrix composites and bonded joints. That was the reason of the widespread use of ΔG as crack driving force parameter [101]–[106].

However, the main concern of ΔG is that it could not be considered as a valid similitude parameter due to its dependence on the mean load of the cycle, P_{med}:

$$\Delta G = G_{max} - G_{min} = \frac{P_{max}^2 - P_{min}^2}{2B}\frac{dC}{da} = \frac{\Delta P P_{med}}{2B}\frac{dC}{da} \qquad (2\text{-}3)$$

where P_{max} and P_{min} are the maximum and minimum loads of the cycle.

$\Delta\sqrt{G}$ has been applied with more or less success in polymers, composites and adhesive joints as the R-ratio effect is still evident in many cases [99], [100], [107]–[111].

2.3.3 Fatigue behaviour of Polyamide 12 manufactured by Selective Laser Sintering.

As previously mentioned, *SLS* PA-12 stands out for covering specific requirements for various applications in the automotive and aeronautical industries [26], [112]–[115]. In these applications, parts made of this material must have sufficient fatigue resistance to meet the in-service loading and operational performance as they are submitted to dynamic loading either applied directly or indirectly through the interaction of the entire structure with the surrounding environment [26], [114], [115].

Regarding the stress-life performance of *SLS* PA-12, *Table 2-3* collects some of the most representative works in which the processing parameters (when provided), testing conditions and main results are summed up. Van Hooreweder et al al. [30], [116], [117] analysed the influence of the frequency (1 Hz and 3 Hz) and the building direction on the S-N curves at a stress ratio, *R*, of -1. They obtained that the building orientation had no influence on the fatigue properties and the thermal fatigue failure was attained at certain combination of high stress amplitude and test frequency. Besides, they also analysed the fatigue behaviour of notched samples and compared the results obtained from specimens processed via *SLS* and *IM.* Regarding the notch effect, the fatigue resistance of notched samples was better than that obtained

from plain specimens, attributable to the reduced thermal load in the former. In case of the effect of the processing technique, no difference in the fatigue resistance was observed between the two manufacturing techniques [30]. Munguia and Dalgarno [118] obtained the *SLS* PA-12 fatigue behaviour in both reversed and rotating bending (R=-1), showing an isotropic response (no influence of the load direction with respect to the layered structure) in terms of the fatigue behaviour for both testing configurations. They also analysed the influence of the frequency (30 Hz and 50 Hz) in four point rotating bending fatigue tests, evidencing lower fatigue response at high frequency [119]. Moreover, they estimated a fatigue limit of 14 MPa, although no standard or recognized methodology was followed to attain this value. Amel et al. [120] investigated the effect of the geometry (thickness) on the fatigue behaviour explored through S-N curves obtained under displacement-controlled tension-tension (R>0) and force-controlled fully reverse fatigue loading (R=-1). The tests carried out in Low Cycle Fatigue regime evidenced creep as the main mechanism of failure. Schob et al. [121] followed the damage evolution through X-ray refraction, computed tomography and temperature rise under cyclic loading (fatigue tests at 3 Hz and R=-1) with the aim of finding the parameters of the Chaboche material model and the Gurson-Tvergarard-Needlemen damage model. Finally, Kim et al. [122] studied the effect of the shape and size of geometrical defects induced during sintering on the fatigue life. Evidently, the fatigue response impoverished with the increase in size of the defects and the authors applied the Castillo-Canteli-Siegele model [123] extended with the cyclic J-integral to predict the fatigue life of the specimens with induced geometrical defects.

Table 2-3. Compilation of stress-life behaviour of PA-12 processed by SLS and IM obtained by several authors. The processing parameters, the testing conditions and a sum up of the main results of the investigations are included.

		Processing parameters	**Testing conditions**	**Results**
Selective Laser Sintering (SLS)	Van Hooreweder et al. [30], [116], [117]	· PA2200 · EOS P730 machine · Energy density: 0.031 J/mm^2 · Layer height: 120 µm · Building chamber: 170 °C	·Frequency: 1-3 Hz · R=-1 · Plain and notched samples · Load applied parallel and perpendicular to layers · Force control	· S-N curves without Basquin law fitting · Notched specimens better performance than plain samples · Thermal failure (3 Hz) · No orientation effect
	Munguia and Dalgarno [118], [119]	· Duraform · 3D Systems sPro 60D · Laser Power: 12 W · Laser scan: 5 m/s · Layer height: 120 µm	· Frequency: 30 and 50 Hz · R=-1 · Surface roughness: 50-80 µm · Load applied parallel and perpendicular to layers · Force control	· S-N curves without Basquin law · Worse fatigue resistance at high frequency · No influence of the loading direction · Fatigue limit of 14 MPa

Selective Laser Sintering (SLS)	Amel et al. [120]	· PA2200 · EOS Formiga P100 · Laser Power: 21W · Laser scan: 2.5 m/s · Layer height: 100 µm · Laser beam diameter: 0.43 mm · Building chamber: 170 °C	· Frequency: 2 Hz · R=-1 (force control) and R>0 (displacement control) · Surface roughness: 50-80 µm · Load applied perpendicular to layers · Displacement and force control tests · Specimens with different thickness	· No S-N curves · No influence of the thickness in the fatigue behaviour · In Low Cycle Regime (displacement control), creep dominant mechanism
	Schob et al. [121]	· 3D Systems sPro 230 · Laser Power: 70 W · Laser scan: 10 m/s · Layer height: 80-150 µm · Building chamber: 170 °C · Powder particles size: 20-80 µm	· Frequency: 3 Hz · R=-1 · Force control	· $\Delta\sigma = 10^{26} N^{-17.07}$ (MPa) · Cyclic softening and self-heating · Damage modelling

Selective Laser Sintering (SLS)	Kim et al. [122]	· Duraform FR1200 · 3D Systems sPro 60HD	· Frequency: 5 Hz · R=0 · Force control Specimens with controlled pores (shape and size) induced during sintering	· S-N curves without Basquin law · Detriment in the fatigue life with increase in size of pores · Application of models to predict the fatigue life of specimens with induced geometrical defect.
Injection moulding (IM)	Van Hooreweder et al. [30]	· PA2200 EOS · ES200/35 HL machine · Mould temperature: 60 °C · Holding time: 3 s · Injection speed: 60 mm/s · Injection pressure: 50 bar · Nose temperature: 230 °C · Melt injected at 240 °C	· Frequency: 1-3 Hz · R=-1 · Plain and notched samples	· S-N curves without Basquin law · Notched specimens better performance than plain · Thermal failure (3 Hz) · No processing technique effect

Concerning the fatigue crack growth behaviour of *SLS* PA-12, *Table 2-4* gathers the main results of the papers found in the literature dealing with this issue. Once more, for a proper comparison of the results in the literature, the processing parameters, when provided by the authors, are included. As observed, there is scarce literature in this topic. Salazar et al. analysed the effect of the temperature and the short glass fibre reinforcement and the hygrothermal ageing on the fatigue crack growth response of *SLS* PA-12 [39], and also determined the differences in the fatigue crack growth behaviour of petrol-based *SLS* PA-12 and bio-based *SLS* PA-11 [40]. The fatigue behaviour of the *SLS* PA-12 was similar at room temperature and at -50 °C but the reinforced material presented an improved fatigue crack growth behaviour at low temperature in comparison with the neat PA-12. The reason was the predominant crack tip bridging mechanism in the composite against the brittle intergranular fracture in the neat PA-12 [39]. On the other side, when comparing the fatigue performance of the bio-based PA-11 versus the petrol-based PA-12 processed via *SLS*, the former presented better fatigue crack growth behaviour than the latter at both 23 °C and -50 °C. Once again, the reason was the fatigue failure, while in PA-11 the mechanism was ductile through cavitation, void growth and coalescence, in PA-12 the dominant mechanism was brittle crazing [40]. Under water conditions, the fatigue response worsened abruptly due to the reduction in crystallinity and molecular weight by hydrolysis, resulting in embrittlement [40]. Despite the inherent anisotropic nature of the stratified *SLS* process can suppose a major limitation, only Blattmeier et al. [124] have treated this issue, attaining no concluding results. Moreover, in this work the fatigue crack growth behaviour of *SLS* and *IM* processing techniques obtained through a load increase method is

compared and the influence of the surface finishing is tackled. In case of the processing technique, there seemed to be a slight better performance on the fatigue response of the *SLS* specimens in comparison with the *IM* samples while the surface finishing seemed to have no significant influence. Finally, Boukhili et al. [79] studied the fatigue crack propagation behaviour of injection moulded PA-12 and the influence of the test frequency, load waveform, specimen configuration and thickness and the material orientation, that is, the material response depending if the load direction was applied parallel or perpendicularly to the injection flow direction. The most interesting result obtained by these authors was that ΔK was not an appropriate crack driving force to describe the fatigue crack propagation of polyamides. They also concluded that the fatigue crack growth behaviour was evidently dependant on the load wave form, the specimen configuration and thickness and above all, of the frequency.

Table 2-4. Processing parameters, testing conditions and main results of the fatigue crack growth behaviour of PA-12 processed by SLS and IM found in the literature (CT: Compact Tension and SENT: Single Edge Notch Tension).

		Processing parameters	**Testing conditions**	**Results**
Selective Laser Sintering (SLS)	Salazar et al. [39], [40]	· Duraform 3D Systems	· (CT) · ΔK-increasing · R= 0.1 · Frequency: 1 Hz · Dry 23 °C and -50 °C	· PA-12 dry 23 °C · $\frac{da}{dN} = 8.7 \cdot 10^{-9} \Delta K^{13,9}$ $(MPa, mm, ciclo)$
				· PA-12 reinforced short fibres dry 23 °C · $\frac{da}{dN} = 9.2 \cdot 10^{-8} \Delta K^{11,9}$

			· Water conditioned at 23°C	$(MPa, mm, cycle)$)
				· PA-12 dry -50 °C · $\frac{da}{dN} = 2.4 \cdot 10^{-8} \Delta K^{14,6}$ $(MPa, mm, cycle)$
				· PA-12 reinforced short fibres dry -50 °C · $\frac{da}{dN} = 4.6 \cdot 10^{-14} \Delta K^{22,6}$ $(MPa, mm, cycle)$
Selective Laser Sintering (SLS)				· PA12 water saturated 23°C · $\frac{da}{dN} = 0.4 \Delta K^{11,5}$ $(MPa, mm, cycle)$
				· The fatigue curves of PA-12 are not affected by temperature · The composite shows better fatigue response at low temperature · Decrement on the fatigue response in water saturated condition
	Blattmeier et al. [124]	· PA2200 · EOS Formiga P100 · Laser Power: 19W · Laser scan:	· (CT) · Load increase method stress profile · R= 0.1 · Frequency:	· No fitting of Paris law curves · No concluding results regarding the orientation

		2500 mm/s · Layer height: 100 μm	10 Hz · Load Applied parallel, perpendicular and with 45° to the layers · Surface treatment by grinding	· Worse behaviour in IM specimens · No influence of the surface finishing technique.
	Blattmeier et al. [124]	· Vestamid Typ L1600 · Arburg Allrounder		
Injection moulding (IM)	Boukhili et al. [79]	· AMVO PA12	· (CT and SENT) · R= 0.1 · Frequencies·: 1 Hz, 5 Hz and 10 Hz · Different load waveform · Specimens with different thickness · Load applied parallel and perpendicular to injection direction	· ΔK is not an adequate crack driving force parameter · The orientation induced by moulding influences the fatigue crack growth behaviour · No effect of the testing frequency · No fitting of Paris law curves

2.4 DESIGN AGAINST FATIGUE

There are two different philosophies of the design against fatigue: the safe-life approach and the damage tolerance approach. The former, and also the oldest, has the sole objective of avoiding the fatigue failure during the design life and

is focused on the crack initiation phenomenon. On the other hand, the damage tolerance approach assumes that defects in form of cracks will exist, caused by processing or fatigue, and that this damage can progress during service life. In this case, the focus is on ensuring that fatigue cracks do not reach a critical value through regular maintenance labours. So, the attention is paid to the crack propagation phenomenon.

The failure criteria in the safe-life approach are the nominal stress-life (S-N) or the local strain-life (ε-N) models, which are used in the calculations of finite-life design to guarantee the duration of the component at the maximum expected stress or load. On the other hand, the damage tolerance approach is supported by Fracture Mechanics, employed to determine whether the fatigue cracks will grow enough to produce failures when detected in periodic inspections. For infinite-life design, Kitagawa and Takahashi [125] noticed that the fatigue life data could be represented in a double logarithm stress range, $\Delta\sigma$, and crack length, a, diagram by two lines plotted in blue in *Figure 2-10*. One represents the plain specimen fatigue strength, given by the stress-based fatigue limit, $\Delta\sigma_{fl}$, of the safe-life approach (line AB). The other line (line BC) is the prediction of the Fracture Mechanics and given by the stress intensity threshold, ΔK_{th} [78], [126].

The slope of the straight-line BC of *Figure 2-10* is defined by:

$$\Delta\sigma = \frac{\Delta K_{th}}{\sqrt{\pi a}} \qquad (2\text{-}4)$$

For any stress-crack length combination below the line ABC, a crack will not grow and the fatigue life can be assumed as infinite (area in green in *Figure 2-10*).

The most characteristic feature of the Kitagawa diagram is that it can be divided into three zones. The zone named as *Microstructurally short cracks (MSC)* is controlled by crack initiation damage phenomena, the *Long Cracks (LC)* zone is controlled by crack propagation phenomena and there is a transition zone between the two called the *Physically Short Cracks (PSC)* zone, where a competition between the two mechanisms occurs. In the *PSC* area neither the Fracture Mechanics nor the stress or strain life models provide proper predictions.

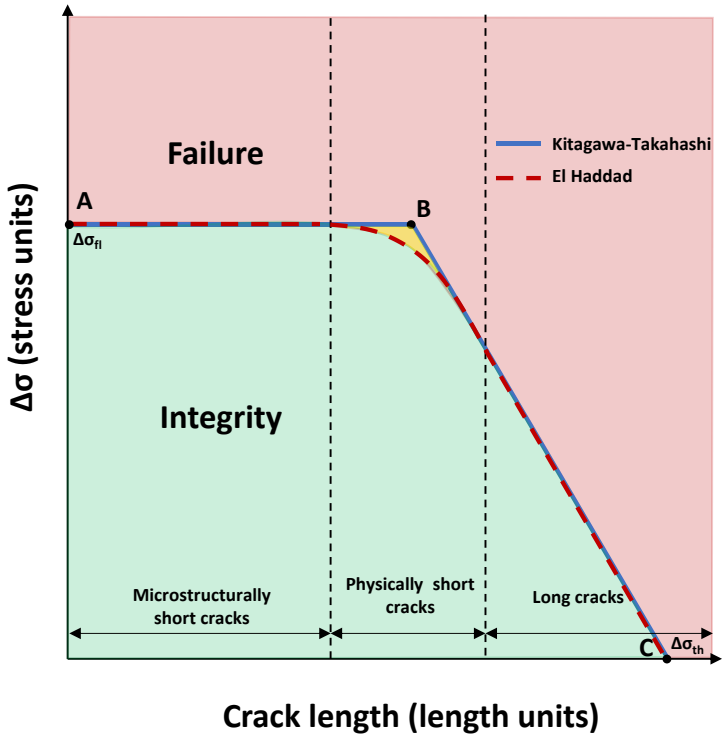

Figure 2-10. Kitagawa-Takahashi diagram with the Kitagawa-Takahashi prediction (blue line) and El Haddad empirical model (dashed red line). The green area is the integrity area, the red area is the failure area and yellow area is the area where the models differ. The three different crack stages are differentiated (microstructurally short crack (MSC), physically short crack (PSC) and long crack (LC)).

The empirical results obtained for different metals revealed that Kitagawa-Takahashi diagrams describe correctly the fatigue behaviour for *MSC* and *LC*

regimes, but in the *PSC* regime, the diagram overestimates the real behaviour of the material, which is actually below the two lines AB and BC defined by the $\Delta\sigma_{fl}$ and ΔK_{th} values. For this reason, in *Figure 2-10* it is also represented in dashed red line an empirical model proposed by El Haddad which modifies the initial Kitagawa-Takahashi predictions [127].

El Haddad et al. proposed their model just two years later than Kitagawa and Takahashi one [125], as a result of test results on aluminium alloys and on steels [128]. This model is governed by the following expression:

$$\Delta\sigma_{Hd} = \frac{\Delta K_{th}}{\sqrt{\pi(a + l_0)}} \qquad (2\text{-}5)$$

where $\Delta\sigma_{Hd}$ is the applied stress range given by the model and l_0 is a characteristic length which depends on the material and on the microstructure and is calculated as follows:

$$l_0 = \frac{1}{\pi}\left(\frac{\Delta K_{th}}{\Delta\sigma_{fl}}\right)^2 \qquad (2\text{-}6)$$

The line given by $\Delta\sigma_{fl}$ of the Kitagawa-Takahashi diagram overestimates the real critical stress range, which is reduced by the presence of short cracks which are lightly larger than the microstructural barriers. On the other hand, the line BC given by the Fracture Mechanics approach does not match the experimental values due to the small size of the crack. The validity of the El Haddad model has been confirmed in aluminium alloys [129], [130], steels [125], [127], [131]–[133] and titanium alloys [134].

Chapter 3.

Objectives

The main objective of this investigation was to determine the fatigue behaviour of polyamide 12 processed via the additive manufacturing technique as selective laser sintering and to compare it with that manufactured by the conventional technique as injection moulding. The fatigue assessment was carried out from the two approaches in design: the safe life approach and the damage tolerant approach. In the first case, the S-N or Wöhler curves and the fatigue limit were computed for finite and infinite lifetime, respectively. In the second case, the fatigue crack propagation curves as well as the threshold values were measured. Due to the layer-wise structure of the parts fabricated by selective laser sintering, which may induce an anisotropic mechanical response, two loading directions with respect to the layered structure were evaluated, one with the load applied parallel to the layered structure and the other with the load applied perpendicularly. To attain this main goal, the following key objectives were defined:

- Measurement of the physical and thermal properties as well as the microstructural features of the polyamide 12 manufactured via selective laser sintering and injection moulding.
- Characterization of the mechanical properties through tensile and fracture characterizations of the materials under study.
- Determination of the fatigue behaviour of plain specimens and the fatigue crack growth behaviour at a frequency of 1 Hz and a stress ratio of 0.1, analysing the effects of orientation and manufacturing technique.
- Development of a map of fatigue through the generalised Kitagawa-Takahashi diagrams. Special attention was paid to the physically short

crack regime, and the empirical model of El Haddad was also evaluated for all the materials and conditions under study.

- Identification of the micromechanisms of failure as a function of orientation and manufacturing technique.

Chapter 4.

Materials and experimental procedure

4.1. MATERIAL: POLYAMIDE 12

The materials under study were processed using two different techniques, injection molding (*IM*) and selective laser sintering (*SLS*). Specimens made by *IM* were manufactured by *Aries Industrias del Plástico, S.A.,* located in Spain. The raw material employed was the commercial PA-12 *Evonik Vestamid* supplied in the form of pellets, and the parameters during the manufacturing process are included in *Table 4.1.*

Table 4.1. Manufacturing parameters of IM PA-12 samples.

Mould temperature	Filling time	Holding time	Injection Speed	Injection pressure	Mold clamping force
60 °C	2.1 s	6.5 s	6-8 mm/s	10 MPa	1500 kN

The *SLS* fabrication was carried out by *Prodintec*, in Spain, employing an *EOS Formiga P-100* LS machine which uses a CO_2 laser configured with the optimum process parameters, which are contained in *Table 4.2*. The commercial PA-12 powder suitable for *SLS* was neat PA-12 EOS PA2200.

Table 4.2. Manufacturing parameters of SLS PA-12 samples.

Particle diameter	Powder bed temperature	Frame temperature	Layer thickness	Laser power
40 – 90 µm	171.5 °C	135.5 °C	0.2 mm	25 W

The technical information of the raw materials was supplied by the manufacturers *Evonik* and *EOS*. *Table 4.3* contains the most remarkable properties of *Evonik VESTAMID* and *EOS PA* 2200 reflected in the manufacturers datasheets [135], [136].

Regarding *EOS PA 2200*, the particle size distribution ranged from 40 to 90 µm, being centred on 50 – 60 µm.

Table 4.3. Evonik and EOS PA 2200 properties[135], [136] .

	Evonik VESTAMID	EOS PA 2200
Bulk density	-	> 0.43 g/cm^3
Processed density	1.015 ± 0.005 g/cm^3	0.93 ± 0.25 g/cm^3
Melting temperature	178°C	184 °C
Crystallization temperature	-	138 °C
Softening temperature 50 °C/h 50N	140°C	163 °C
Tensile strength	46 ± 1 MPa	45 ± 3 MPa
Young's modulus	1475 ± 120 MPa	1700 ± 150 MPa
Elongation at break	> 50 %	20 ± 5 %
Flexural modulus	-	1240 ± 130 MPa
Charpy-Impact strength	-	53 ± 3.8 kJ/m^2

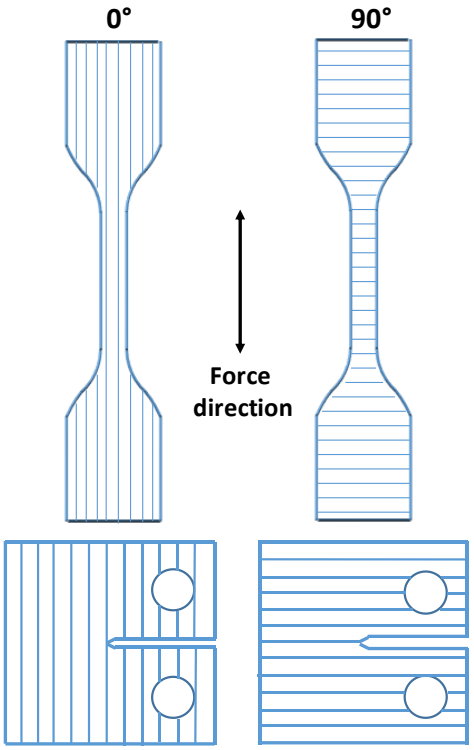

Figure 4-1. Dumbbell and compact tension (CT) specimens oriented at 0 ° and at 90 °. Sintered layers on each orientation are outlined.

Different specimen configurations were manufactured. In the case of *SLS*, due to the anisotropic nature of the process, two batches of specimens were fabricated for each configuration. In the one named 0°, the layered structure was disposed in such a way that the force was applied parallel to the layer planes; meanwhile in the batch named 90°, the layers were perpendicular to the applied force (*Figure 4-1)*.

4.2. PHYSICAL CHARACTERIZATION

4.2.1 Density measurement

Despite the theoretical densities provided by the manufacturers, the experimental ones were measured in the specimens produced. The density of the pieces was determined experimentally measuring 5 specimens of each geometry in a precision balance *Mettler Toledo AX205 DeltaRange®,* which has a resolution of ± 0.00001 g. Following the Archimedes principle, each specimen was introduced in a beaker with a known immersion medium and measuring the amount of displace fluid. The density of the sample, ρ, is given by the following expression:

$$\rho = \frac{W_{air}}{W_{air} - W_{im}}(\rho_0 - \rho_L) + \rho_L \qquad (4\text{-}1)$$

where W_{air} is the weight of sample in air, W_{im} is the weight of sample in the immersion medium, ρ_0 is the density of the immersion medium and ρ_L the density of air (0.0012 g/cm^3). Due to the nearness of the expected PA-12 density to that of distilled water, commonly used as immersion medium, which is ρ_0= 0.99782 g/cm^3, acetone was also employed as immersion medium in this

case, with ρ_0= 0.787 g/cm^3. The closed porosity of each batch was calculated in reference to the theoretical bulk density value of 1.02 g/cm^3 of the PA-12 [137]. Five replicas were measured for each material and condition.

4.2.2 Surface Roughness tests

Surface roughness was measured using a roughness tester *Mitutoyo SJ-301* equipped with a detector whose tip had a radius of 60 µm and a tip angle of 60°. A total number of 62 tests were carried out in the dumbbell geometry of each material longitudinally and transversely. The profile roughness parameters obtained were the maximum peak to valley height of the profile, R_z, and the arithmetical mean value of the tested profile along a length l_r, R_a, given by:

$$R_a = \frac{1}{l_r}\int_0^{l_r} |z(x)|dx \qquad (4\text{-}2)$$

4.3. MICROSTRUCTURAL CHARACTERISATION

The microstructural characterisation aims to analyse the crystalline phase, focusing on its morphology and its size. For *SLS* PA-12, films between 3 and 15 µm in thickness were sectioned from the centre of the bulk using a rotary microtome *Leica RM2255* [138]–[140]. The extractions were performed parallel and perpendicular to the build direction. Although the anisotropy is not a key microstructural factor in *IM* specimens, an initial optical inspection revealed some differences between the core and the skin of the material. The same procedure as in *SLS* material was followed for *IM*, that is, the films were extracted from either the core or the skin of the bulk specimen. These films were placed on microscope glass slides and analysed in an optical microscope

Motic BA310 Met-T equipped with a 5 megapixels *ZEISS Axiocam 105* camera. For their inspection, transmitted polarized light and dark field modes were applied [141]. A total number of 90 micrographs were explored, 30 of *SLS* at 0° orientation, 40 of *SLS* 90° at orientation and 20 of *IM*. The images of the *SLS* specimens were taken using a 50x objective with a 10x eyepiece lens, whereas for the examination of the *IM* films, a x100 objective lens immersed in a transparent oil with a 1.482 refraction index to attain a total magnification of x1482 was needed for the visualization of the characteristic microstructural features.

A total number of 157 spherulites were measured manually using an image analysis software.

4.4. THERMAL CHARACTERISATION

The purpose of the thermal characterisation was to determine the thermal properties and the crystallisation characteristics of *SLS* PA-12 and *IM* PA-12.

Firstly, a Differential Scanning Calorimetry (*DSC*) was performed with a *DSC Mettler 822e* equipment. *DSC* tests consisted in using specimens with 12.0 ± 0.5 mg in weight which were subjected to a heating ramp at a rate of 10 °C/min from 25 °C to 250 °C, followed by a cooling ramp at a rate of 10 °C/min from 250 °C to 25 °C. This heating/cooling processes were performed twice in a row. The crystallisation temperature, T_c, and the enthalpy, ΔH_c, were collected from the cooling cycle, meanwhile the melting temperature T_m and the enthalpy, ΔH_m, and, when detectable, the glass transition temperature, T_g, were extracted from the second heating cycle.

Regarding the calculation of the crystallinity degrees, it was distinguished between the melting crystallinity degree, χ_m, and the crystallinity degree from the crystallisation peak, χ_c. In case of the former, the heat of fusion, ΔH_m, was obtained by integrating the heat flow under the melting peak from the second heating cycle; and for the latter and in a similar way, the crystallization heat, ΔH_c, was also calculated by integrating under the crystallisation peak from the cooling cycle. Finally, the crystallinity degrees were computed using the following equations:

$$\chi_m = \frac{\Delta H_m}{\Delta H_0} \quad ; \quad \chi_c = \frac{\Delta H_c}{\Delta H_0} \qquad (4\text{-}3)$$

using an enthalpy of fusion, ΔH_0 = 209 J/g, which is the enthalpy of fusion of perfect PA-12 crystals [142]. The crystallinity degrees were calculated as the average value from χ_m and χ_c.

Additionally, Dynamic Mechanical Analysis (DMA) was carried out using a *TA Instruments DMA Q800* analyser with a single cantilever configuration according to ASTM D5023 Standard [143]. Specimens with 17x12x3 mm^3 in size were heated from - 100 °C to 150 °C at 1 Hz of frequency and at a heating rate of 3 °C/min. The glass transition temperatures were computed as the maximum values of the loss factor (*tanδ*) curves.

4.5. MECHANICAL CHARACTERISATION

Tensile tests were carried out according to ASTM D638 Standard [144] to determine mechanical properties such as tensile strength, Young's modulus, Poisson's ratio and elongation at break. These tests were done using dumbell type IV specimens with the dimensions shown in *Figure 4-2*.

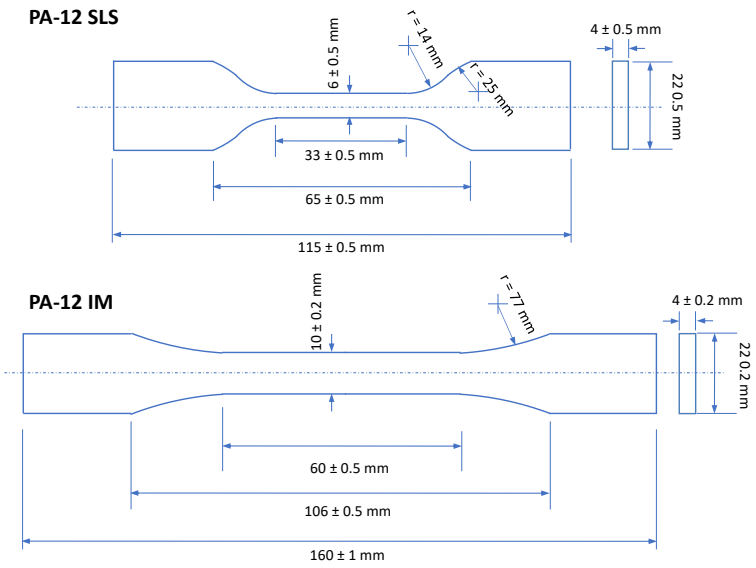

Figure 4-2. Tensile dumbbell specimens with dimensions according to ASTM D638 [144].

Tests were carried out at -50 °C, 23 °C and 50 °C at 0° and 90° orientations in *SLS* specimens and at 23 °C in *IM* samples. A universal electromechanical testing machine *MTS Alliance RF/100* equipped with a load cell of ± 5 kN was employed. The crosshead speed was 5 mm/min and a contact extensometer *MTS 634.12F-54* (*Figure 4-3*) was used for measuring the axial deformation. A total number of three valid repetitions were performed for each condition. For the tests at -50 °C and 50 °C, the load train, formed by the hinges, grips and the specimen with the extensometer, were placed inside an environmental chamber *MTS 651.06E-03* (*Figure 4-3*). Cooling and heating processes were performed maintaining a constant load of 100 N on the specimen for balancing the thermal contractions. When the required temperature was reached, conditioning was held for a minimum of 30 minutes to reach a stationary state before starting the test.

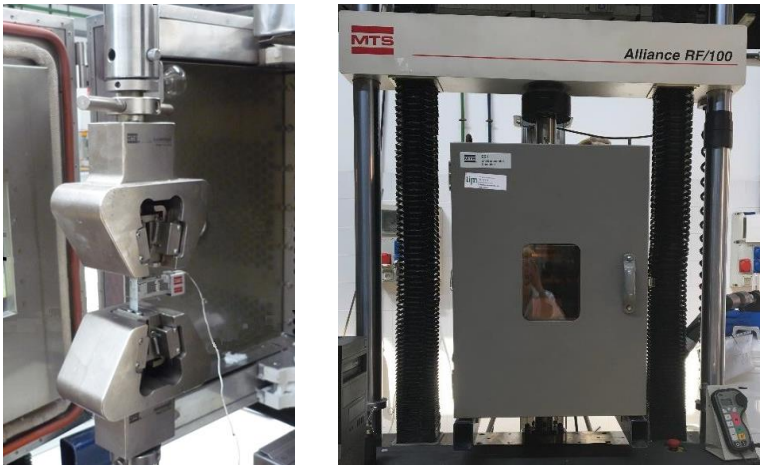

Figure 4-3. MTS Alliance RF/100 with environmental chamber MTS 651.06E-03 and load train installed for tensile tests at -50 °C and 50 °C.

In addition, 2-Dimensional video correlation was used at all temperatures for obtaining the 2D displacement field and, in particular, the longitudinal and the transverse deformation using a VIC 2D videoextensometer. This equipment consisted of a *PointGrey Grasshopper3* 5 Megapixel camera connected to a computer with the software *Correlated Solutions VIC 2D.* Because videoextensometry needs reference points to follow their movement during the test, the surface of the white specimens were sprayed with black paint to attain a random, matte pattern of speckles, providing a large quantity of points to be analysed, as shown in *Figure 4-4*.

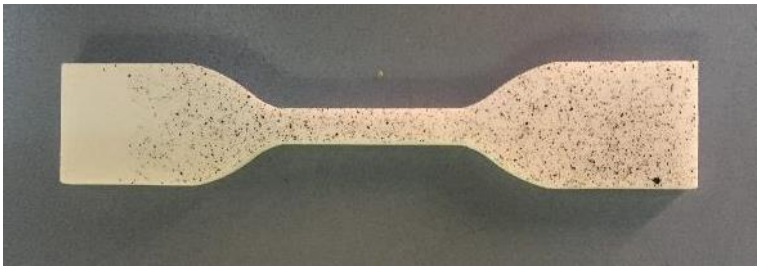

Figure 4-4. Tensile specimen painted with a random dot pattern.

Moreover, to obtain the best possible contrast in the images, LED lightening systems were employed to avoid any type of reflection of the specimen surface. The camera must be focused on the specimen perpendicularly to its lateral surface. The tensile test assembly at room temperature is shown in *Figure 4-5*.

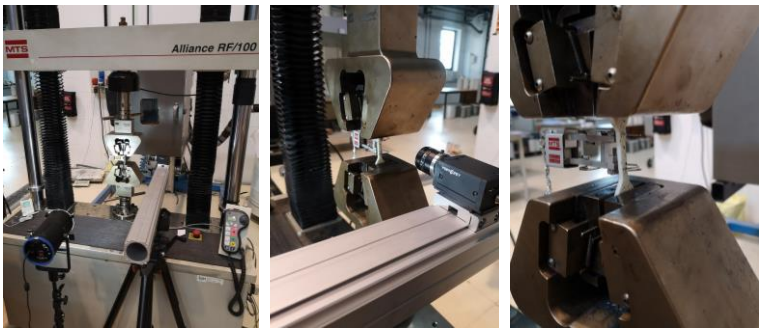

Figure 4-5. MTS Alliance RF/100 equipped for tensile tests at room temperature, with contact extensometer MTS 634.12F-54 and VIC 2D videoextensometer.

4.6. FRACTURE AND FATIGUE TESTS

4.6.1 Crack sharpening

Compact Tension (CT) configuration with the dimensions shown in *Figure 4-6* was used for fracture and fatigue tests. The only difference between fracture and fatigue specimens was the initial notch length, which in the fatigue specimens was the half that in fracture ones in order to fulfil ASTM D5045 standard [145] in fracture and ASTM E647 standard [146] in fatigue characterisations.

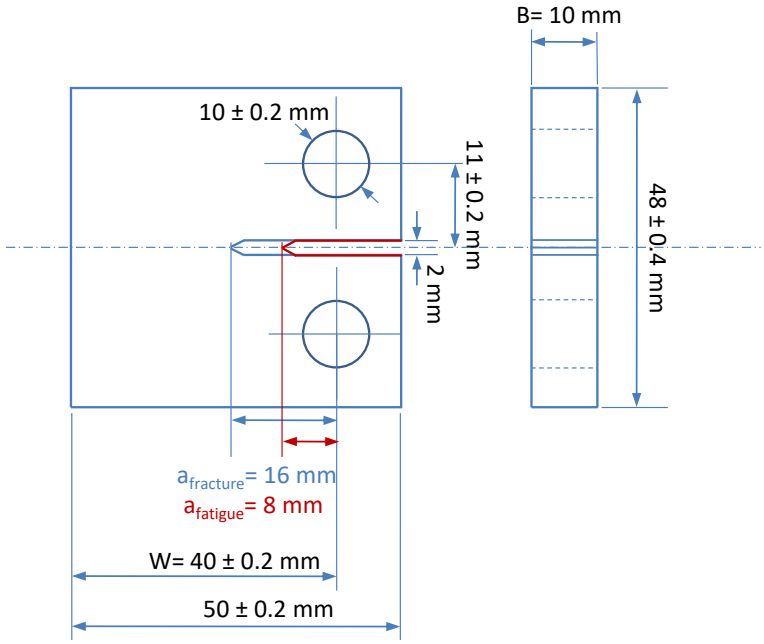

Figure 4-6. Compact Tension (CT) specimen dimensions used in fracture tests according to ASTM D5045 standard [145] *and in fatigue tests according to ASTM E647*[146].

The sharp crack in the fracture CT specimens was generated by tapping a razor blade with a thickness of 0.3 mm, previously frozen at liquid nitrogen temperature (-196 °C), on the root of the machined notch till attaining an initial natural crack length to width ratio, a_0/W, of 0.5. This ratio ensures a sharp crack length enough to avoid the influence of the manufactured notch on the results [43], [145].

In the fatigue CT specimens, the sharp crack was introduced by tapping in a similar way as in the fracture samples but, in this case the sharp crack lengths should be only larger than the notch height, of 2 mm, to avoid the notch effects [43], [146].

Small cracks were introduced in dumbbell specimens with lengths of 0.2 mm, 0.3 mm, 0.5 mm, 1 mm, 2 mm, 2.5 mm and 3 mm by pressing a microtome razor blade with a tip diameter of 5.3 µm (*Figure 4-7*). This tip diameter ensures

a notch radius smaller than 10 µm, which is the estimated limit for considering the crack as a natural crack [147], [148]. These specimens were used for static and fatigue characterisations in the *PSC* regime (*section 2.4*)

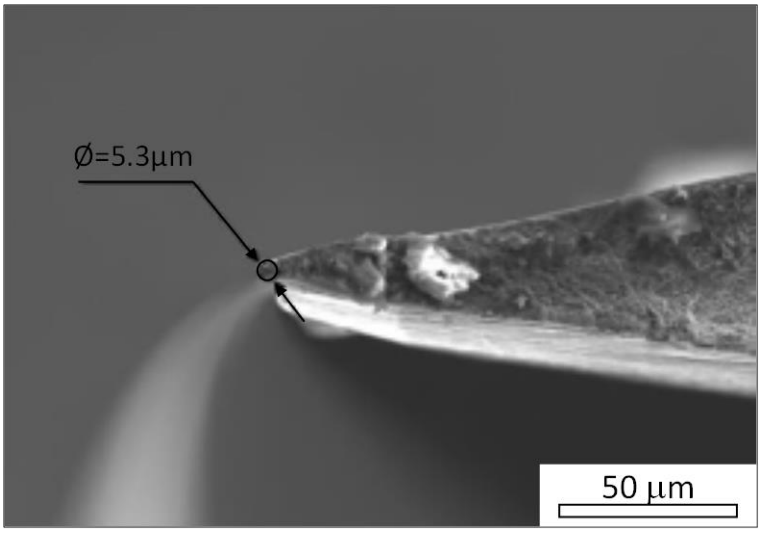

Figure 4-7. SEM image of the razor blade tip of the microtome with the diameter measurement [148].

After notch sharpening or small crack introduction, the crack front was inspected either visually or by optical means to guarantee no damage in form of microcracks or whitening. In case of presence of damage, the samples were discarded.

4.6.2 Fracture tests

Tests were carried out in a universal servohydraulic testing machine *MTS 810 Materials Testing*, equipped with a load cell of ± 5 kN. The crosshead speed was 5 mm/min. A Crack Opening Displacement transductor (*COD*) *MTS 632.02F-20* with a displacement range of + 3.9 mm/ -2 mm was also employed. The tests were performed in *SLS* specimens at 0° and 90° orientations, and in *IM* samples. To study the evolution of the fracture properties with the temperature, tests were undertaken at three different temperatures, -50 °C,

23 °C and 50 °C, completing three repetitions of each condition. For the -50 °C and 50 °C tests, an environmental chamber *MTS 651.06E-03* was used, installing the load train, formed by the hinges, grips and the specimen with the *COD* transductor, inside it (*Figure 4-8*).

Figure 4-8. Load train assembly inside environmental chamber MTS 651.06E-03 for tests at -50 °C and 50 °C.

Similar procedure to that of the tensile tests was performed, maintaining a constant load of 50 N on the specimen during cooling and heating processes until the load frame finished of balancing the thermal contractions and, consequently, reaching a stationary state. When the required temperature was reached, conditioning was held 25 min more before starting the test to guarantee the thermal equilibrium.

Attending to the mechanical behaviour of each material and test condition, the results were analysed applying the Linear Elastic Fracture Mechanics (*LEFM*) or the Non-Linear Fracture Mechanics (*NLFM*) approach as appropriate. The ISO 13586 Standard was followed to determine the crack opening mode (mode I) fracture toughness in terms of the stress intensity factor, K_{IC}, and the energy release rate, G_{IC}, under *LEFM* approach [149].

From the load (*P*)-crack mouth opening displacement (*v*) record, the maximum load, P_{max}, and a conditional load, P_Q, are calculated. P_Q is used to determine a conditional stress intensity factor, K_Q, and a conditional energy release rate, G_Q.

Firstly, $P_{5\%}$ is computed as the intersection of the *P-v* record with a line having a 5% smaller stiffness than the initial one, *S*. If the maximum of the curve falls within the best straight line to determine *S* and the line with a 5% lower stiffness, then P_{max} corresponds with the load at crack growth initiation, P_Q. If P_{max} falls outside these two lines, then P_Q is $P_{5\%}$. If $P_{max}/P_Q < 1.1$ then P_Q is used for K_Q calculation, otherwise, the test is invalid. With this limitation, the critical stress intensity factor K_Q is obtained:

$$K_Q = f(\alpha)\frac{P_Q}{B\sqrt{W}} \qquad (4\text{-}4)$$

with *B* the specimen thickness, *W* the width and *f(α)* the geometry calibration factor depending on the crack length *a* given by:

$$f(\alpha) = \frac{(2+\alpha)}{(1-\alpha)^{3/2}}(0.886 + 4.64\alpha - 13.32\alpha^2 + 14.72\alpha^3 - 5.6\alpha^4) \qquad (4\text{-}5)$$

being $\alpha = a/W$.

In addition to the previous condition, the standard establishes that to guarantee the plane-strain state, it must be fulfilled:

$$B, W - a, a \geq 2.5 \frac{K_Q^2}{\sigma_y^2} \qquad (4\text{-}6)$$

with σ_y the yield stress of the material for the temperature and loading rate of the test and K_Q is K_{IC} in this case. The energy release rate, G_Q is G_{IC} and in principle it can be obtained from the following equation:

$$G_{IC} = \frac{(1 - \nu^2){K_{IC}}^2}{E} \qquad (4\text{-}7)$$

E is the Young's modulus and ν the Poisson's ratio obtained at the same time and temperature conditions. Due to the many uncertainties introduced by this procedure, particularly, in the determination of the Young´s modulus, G_Q is computed from:

$$G_Q = \frac{U_Q}{BW\varphi(\alpha)} \qquad (4\text{-}8)$$

where U_Q is the energy obtained from the area under the P-v curve until the point P_Q and $\varphi(a/W)$ is the energy calibration factor depending on the crack length given by this expression:

$$\varphi(a/W) = \frac{A'(1 - \alpha)}{H + 2A'} \qquad (4\text{-}9)$$

with

$$A' = 1.9118 + 19.118\alpha - 2.5122\alpha^2 - 23.226\alpha^3 - 20.54\alpha^4 \qquad (4\text{-}10)$$

and

$$H = (19.118 - 5.0244\alpha - 69.678\alpha^2 + 82.16\alpha^3)(1 - \alpha) \quad (4\text{-}11)$$

When the behaviour of the material deviates from *LEFM*, the J-integral vs. crack growth resistance (J-R) curves were obtained directly from the force displacement record according to ASTM E1820 standard using the normalization method [150]. The starting point of this procedure is the measurement, by optical means, of the initial crack length, a_0, and the final crack length, a_f, taken from the fracture surface. Then, each force value P_i is normalized up to but without including the maximum value P_{max}, following the expression:

$$P_{Ni} = \frac{P_i}{WB\left[\frac{W - a_{bi}}{W}\right]^{\eta_{pl}}} \quad (4\text{-}12)$$

where η_{pl} is the plastic constriction factor, which depends on the specimen geometry and is given by:

$$\eta_{pl} = 2 + \frac{0.522(W - a_0)}{W} \quad (4\text{-}13)$$

and a_{bi} is the crack growth applying the blunting correction:

$$a_{bi} = a_0 + \frac{J_i}{2\sigma_y} \quad (4\text{-}14)$$

where

$$J_i = \frac{K_i^2(1-v^2)}{E} + J_{pl,i} \qquad (4\text{-}15)$$

with K_i the stress intensity factor obtained from eq. (*4-4*) and eq. (*4-5*) and $J_{pl,i}$ the plastic component of the J-integral:

$$J_{pl,i} = \frac{\eta_{pl} U_i}{B(W-a_0)} \qquad (4\text{-}16)$$

where U_i is the area under the curve until P_i.

The displacement corresponding with each force level P_i, δ_i, is also normalized to use a plastic normalized displacement, δ'_{pli}:

$$\delta'_{pli} = \frac{\delta_{pli}}{W} = \frac{\delta_i - P_i C_i}{W} \qquad (4\text{-}17)$$

being C_i the specimen elastic load-line compliance using the crack length a_{bi}. The same procedure is employed to obtain the last point, at P_{max}, but using, the measured final crack length, a_f, instead of a_0, the P_{Ni}-δ'_{pli} values are fitted to the normalized function:

$$P_N = \frac{a + b\delta'_{pl} + c{\delta'_{pl}}^2}{d + \delta'_{pl}} \qquad (4\text{-}18)$$

with *a*, *b*, *c* and *d* the fitting parameters. Once these parameters are determined, a_i values are calculated using an iterative method.

Finally, with the force, the displacement and the crack size estimated at each point, the J integral value for each i point was determined using:

$$J_i = \frac{\eta U_i}{B(W - a_i)} \qquad (4\text{-}19)$$

With $\eta = \eta_{pl}$ for the CT configuration and the crack extension, Δa, as:

$$\Delta a = a_i - a_0 \qquad (4\text{-}20)$$

The resulting J-crack growth resistance curve is fitted to a power law $J = C_J \Delta a^{N_J}$, with $N_J \leq 1$. The crack initiation resistance, J_{IC}, is calculated as the minimum value between $J_{0.2}$, which defines crack resistance at 0.2 mm of the total crack growth, and J_{BL}, computed as the intersection between the crack growth resistance curve and the blunting line defined as:

$$J_{BL} = 2\sigma_y \Delta a \qquad (4\text{-}21)$$

The size requirements for plane strain J_{IC} is given by [151]:

$$B, a, W - a > 25 \frac{J_{IC}}{\sigma_y} \qquad (4\text{-}22)$$

The normalized method was applied using the MATLAB® script included in the *Annex A.1.*

4.6.3 Fatigue crack growth tests

The fatigue tests were carried out under the recommendations of the ASTM E647 Standard [146] and ESIS TC4 protocol [152], which aim to obtain the crack propagation threshold value of the control parameter and the fatigue crack propagation curves.

A total number of eight samples of *IM* material and fourteen samples of each *SLS* orientation were tested at room temperature in a servo-hydraulic testing machine *MTS 810 Materials Testing* with a load cell of ± 5 kN and a crack opening displacement (*COD*) extensometer MTS 632.02 F-20 with a displacement range of +3.9 mm/-2 mm (*Figure 4-9*). The tests were carried out at room temperature (23°C), with a frequency of 1 Hz, load ratio R = P_{min}/P_{max} of 0.1 and imposing a sinusoidal load wave. Two test procedures were used according to ASTM E647.

Figure 4-9. MTS 810 Materials Testing machine configured for performing fatigue crack growth tests in CT specimens.

To obtain the crack propagation behaviour until failure, five *IM* specimens and ten *SLS* specimens per orientation were tested in constant-force-amplitude

configuration or increasing control parameter mode. On the other hand, to obtain the crack propagation threshold, three *IM* specimens and four *SLS* specimens per orientation were tested under the decreasing control parameter procedure. Beginning with a control parameter value under the critical value obtained from the fracture tests, tests with decreasing load amplitude were carried out with a step of decrease or normalized variation of the control parameter of -0.05 mm^{-1}. The threshold values were computed for crack growth rate downs to $3 \cdot 10^{-7}$ mm per cycle.

Two methods were used for obtaining the crack growth during the tests. In the first method, the crack growth was calculated by the compliance method from the flexibility of the specimen using expressions determined for metals but also validated for polymers [152]. The expressions that relate the crack length to width ratio, a/W, with the compliance in *CT* specimens are

$$\frac{a}{W} = 1.001 - 4.6695\,U + 18.460\,U^2 + 236.82\,U^3 + 1214.9\,U^4 - 2143.6\,U^5 \qquad (4\text{-}23)$$

where:

$$U = \frac{1}{\left(\frac{BE_V}{P}\right)^{1/2} + 1} \qquad (4\text{-}24)$$

To validate the compliance method, an optical method was used. Images were captured during the test at a specific frequency allowing the tracking of the crack length with a millimetre scale stuck to the specimen's surface. Moreover, the calculated final crack length was compared with the measured fatigue crack length on the fracture surface of each specimen.

The fatigue behaviour has been determined as the crack growth rate, *da/dN*, versus the Crack Driving Force, *CDF*, $\Delta\sqrt{G}$ according to *equation (2-2)*.

The crack growth rate at any average crack length $\bar{a} = \frac{a_{i+1}-a_i}{2}$ is obtained from the crack length versus elapsed cycle with the following expression:

$$\left(\frac{da}{dN}\right)_{\bar{a}} = \frac{a_{i+1} - a_i}{N_{i+1} - N_i} \qquad (4\text{-}25)$$

The control parameter $\Delta\sqrt{G}$ was obtained from *equation (2-1)* in which the value of *dC/da* is given by:

$$\frac{dC}{da} = \frac{1}{EW}\frac{dg}{d\alpha} \qquad (4\text{-}26)$$

where $g(\alpha)$ is the non-dimensional load line compliance [26] and with dg/dα for CT specimens computed as:

$$\frac{dg}{d\alpha} = \frac{(1+\alpha)}{(1-\alpha)^2}\, x \qquad (4\text{-}27)$$

$$\left[\frac{4}{(1-\alpha)}\,(2.163 + 12.219\alpha - 20.065\alpha^2 - 0.9925\alpha^3 - 20.609\alpha^4 - 9.9314\alpha^5)\right.$$

$$\left.+(1+\alpha)\,(12.219 - 40.13\alpha - 2.9775\alpha^2 + 82.436\alpha^3 - 49.657\alpha^4)\right]$$

4.6.4 Fatigue life tests

Fatigue life tests were performed to obtain S-N curves for *IM* and *SLS* specimens at both orientations, according to ASTM D7791 Standard [153]. The specimens had the same geometry and dimensions as those utilized in tensile tests (*Figure 4-2*). A total number of 89 specimens were tested, of which 20 were used for the determination of *IM* PA-12, 32 for *SLS* PA-12 at 90°

orientation and 37 for PA-12 at 0° orientation. Tests were performed at room temperature in a servo-hydraulic testing machine *MTS 810 Materials Testing* with a load cell of ± 5 kN. A contact extensometer *MTS 634.31F-24* with a displacement range of +4 mm/-2 mm was employed to measure the axial strain.

The frequency was 1 Hz, using a sinusoidal load wave form at a constant load amplitude with a load ratio, R, of 0.1. Tests were done at 12 different stress levels, that is with the maximum stress of the cycle, σ_{max}, to the tensile strength ratio between 58.75% and 85%, to guarantee to be within the High Cycle Fatigue regime. At least, two repetitions for each stress level were carried out.

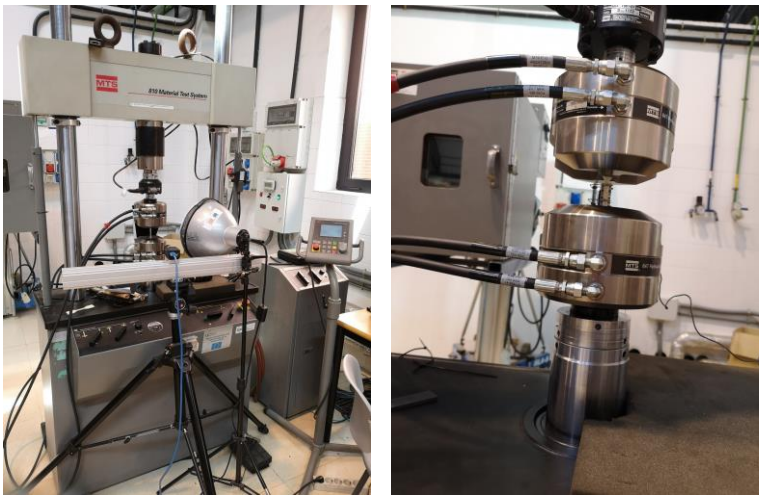

Figure 4-10. MTS 810 Materials Testing set for fatigue life tests.

The tests at the lowest levels were finished at 10^6 cycles due to their high time-consuming aspect, establishing tests which reached this number of cycles without failure as run-outs. Each test was plotted as a single point of the stress range, $\Delta\sigma$, versus N representation, giving as result the Wöhler curve for each material.

The fatigue life curves were fitted to the Basquin equation:

$$\Delta\sigma = B_B N^{m_B} \qquad (4\text{-}28)$$

The estimated value of the fatigue limit, $\Delta\sigma_{fl}$, at 10^6 cycles were determined by the maximum likelihood method, following a test sequence based on the staircase method. In this method, fatigue tests were sequenced at different stress levels with a fixed difference in the applied stress range or initial step of 2.5% of the tensile strength. If a specimen failed before reaching the end of the test, the following test was carried out at a stress level one step lower. Otherwise, the stress level was increased one step in the following test. To obtain a more accurate value, the step was decreased after seven completed tests to 1.25% of the tensile strength. Although the change in the step removed the possibility of using the Staircase method equations developed for metals [154], the maximum likelihood method allowed to obtain an accurate estimation of $\Delta\sigma_{fl}$ [155]–[157]. A total number of 17 for *SLS* PA-12 specimens at 0° orientation, 12 for PA-12 samples at the 90° orientation and 14 for *IM* material were tested to obtain $\Delta\sigma_{fl}$.

The maximum likelihood method was applied assuming that the stress levels of the run-out specimens follow a normal distribution [156], [158]. For a normal distribution with a mean value, μ, and a standard deviation value, s, the likelihood function, L, is given by:

$$L = \prod_{i=1}^{n_T} [1 - F(\Delta\sigma_i, \mu, s)]^{r_i} [F(\Delta\sigma_i, \mu, s)]^{f_i} \qquad (4\text{-}29)$$

where r_i are the number of run-outs and f_i are the number of failures at the i^{th} stress level, $\Delta\sigma_i$, n_T is the total number of stress amplitude levels and F is the cumulative probability of failure of the normal distribution.

This function depends on the stress at the i^{th} stress level, $\Delta\sigma_i$, and the parameters of the normal distribution and is calculated with the following expression:

$$F(\Delta\sigma_i, \mu, \sigma) = \int_{-\infty}^{\Delta\sigma_i} \frac{1}{s\sqrt{2\pi}} exp\left[-\frac{1}{2}\left(\frac{\mu - x}{s}\right)^2\right] dx \qquad (4\text{-}30)$$

The maximum of the likelihood function was obtained using the MATLAB® script proposed by Meizoso et al. [155] and included in the *Annex A.2.*

4.6.4.1 Determination of fracture parameters from damage evolution in plain fatigue samples using the Fracture Mechanics methodology

The fracture toughness was calculated from the measurement of the damage observed and measured from the analysis of the morphology of the fracture surfaces resulting of the fatigue life tests in *SLS* PA-12. The extent of the damage was delimited, that is, the limit associated with the area of crack propagation before instability occurred was determined from the optical and Scanning Electron Microscopy (*SEM*) inspections of the fracture surfaces. The crack nucleated at some point at the surface due to the elevated roughness resulting from the manufacturing process.

The geometrical configuration of the fatigue specimens with a crack growth zone resulting from the crack propagation stage before failure could be assimilated to the Single Edge Notch Tension (*SENT)* fracture specimens.

The fracture parameters were determined using the *NLFM* approach and the J-integral at the instant of failure was computed as

$$J = \frac{\eta U}{B(W-a)} \qquad (4\text{-}31)$$

where U is the area under the unloading load-displacement record of the last cycle before failure, a is the length of the subcritical crack growth zone measured directly from the fracture surface and η is a plastic geometric factor that in case of the SENT configuration is defined as [159]:

$$\eta = 1.067 - 1.767\left(\frac{a}{W}\right) + 7.808\left(\frac{a}{W}\right)^2 - 18.269\left(\frac{a}{W}\right)^3 + 15.295\left(\frac{a}{W}\right)^4 - 3.083\left(\frac{a}{W}\right)^5 \qquad (4\text{-}32)$$

4.7. FRACTOGRAPHY

The fracture surfaces of the tensile, fracture, fatigue crack growth and fatigue life specimens were inspected using scanning electron microscopy. The aim was to determine the micromechanisms of failure dominant at different temperatures, orientations and different manufacturing conditions. The fracture surfaces were gold coated to enhance their conductivity using a sputter coater *EMITECH K550X* with a current of 30 mA for 1 minute. The coated samples were positioned on a conductive specimen holder and examined in a *SEM HITACHI S-3400N*.

Chapter 5.

Results

5.1 DENSITY

Table 5-1 displays the density values of *SLS* PA-12 at 0° and 90° orientations and of *IM* PA-12. The density of *IM* PA-12 is higher than that of *SLS* PA-12, with no differences between 0° and 90° orientations.

Table 5-1. Density measurements obtained with the Archimedes method for IM PA-12 and SLS PA-12 at 0° and 90° orientations.

Sample ID	Density (g/cm^3)		
	SLS		IM
	0° orientation	90° orientation	
1	0.984	0.991	1.018
2	0.975	0.986	1.018
3	0.982	0.984	1.017
4	0.986	0.979	1.017
Average	**0.982 ± 0.005**	**0.985 ± 0.005**	**1.018 ± 0.005**
Porosity (%)	**3.7 ± 0.5**	**3.4 ± 0.5**	**0.19 ± 0.5**

These results are lower than the density of neat PA-12, which is 1.02 g/cm^3 [137]. Nevertheless, the *IM* PA-12 material is almost full dense, with only a porosity percentage of 0.19% versus 3.7% and 3.4% for *SLS* PA-12 at 0° and 90° orientations, respectively. In addition, it is also higher than the theoretical sintered density value of 0.93 g/cm^3 provided by the manufacturer [28] (*Table 4.3*).

5.2 SURFACE ROUGHNESS

Table 5-2 shows the surface roughness results for the three materials. While there is no difference in both R_a and R_z parameters between *SLS* orientations, a clear difference is distinguished between *SLS* and *IM* materials.

Table 5-2. Roughness average, R_a, and the average maximum height of the profile, R_z, of SLS PA-12 at 0° and at 90° orientations and of IM PA-12.

	Roughness average, Ra (µm)	Average Maximum height, Rz (µm)
SLS 0° orientation	12 ± 1	69 ± 8
SLS 90° orientation	12 ± 4	60 ± 20
IM	0.4 ± 0.2	3 ± 2

The roughness average, R_a, of SLS PA-12 are more than one order of magnitude larger than that of *IM* PA-12 and lightly smaller than the values obtained by Guo et al. [160] and Xu et al. [161]. In case of the average maximum height of the profile, R_z, the values of *SLS* PA-12 are 20 times higher than those of *IM* PA-12.

5.3 MICROSTRUCTURAL ANALYSIS

Figure 5-1 shows the characteristic microstructure of the specimens analysed: *SLS at* 0° (*Figure 5-1.a*) and at 90°orientations (*Figure 5-1.b*) and *IM* PA-12 (*Figure 5-1.c*). These images show the spherulites of the crystalline phase, which are usually distributed as spherical crystal colonies with a typical Maltese-Cross pattern, resulting from the birrefrigence of highly ordered lamellae within the spherulites oriented randomly [141], [162]. The spherulites that were fully discernible correspond to those cut in half during the slicing process with the microtome.

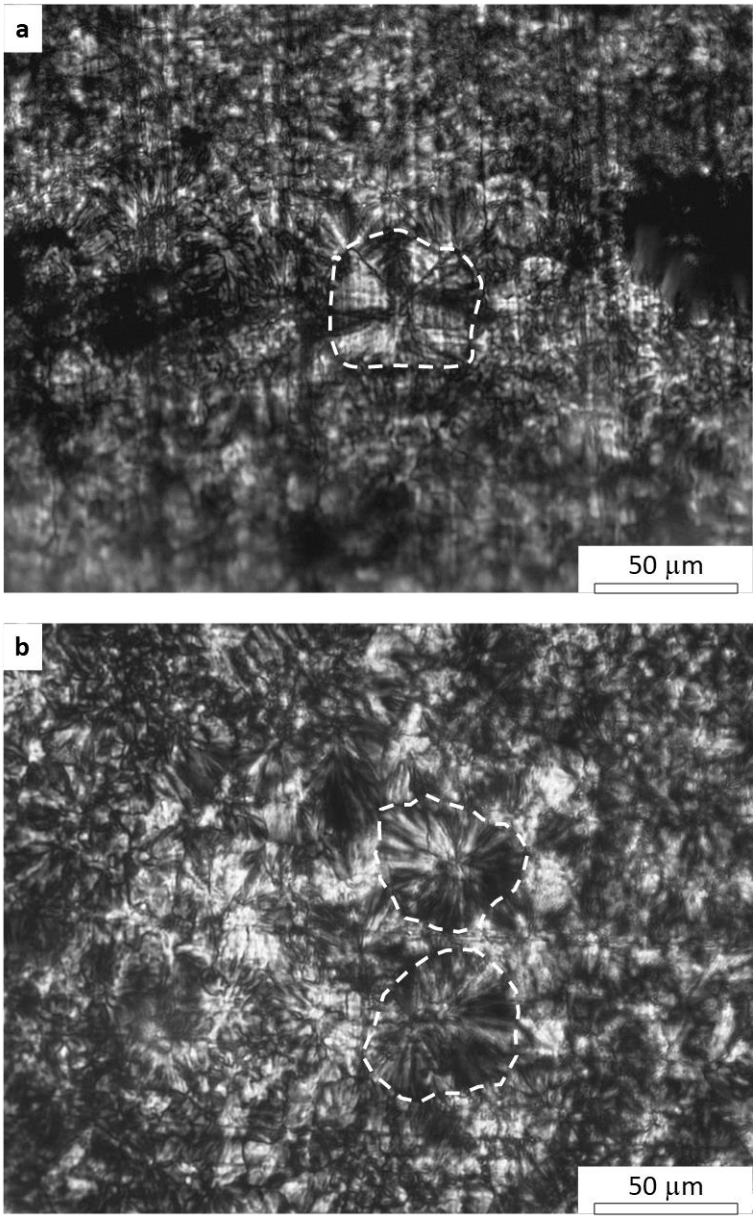
a
50 µm
b
50 µm

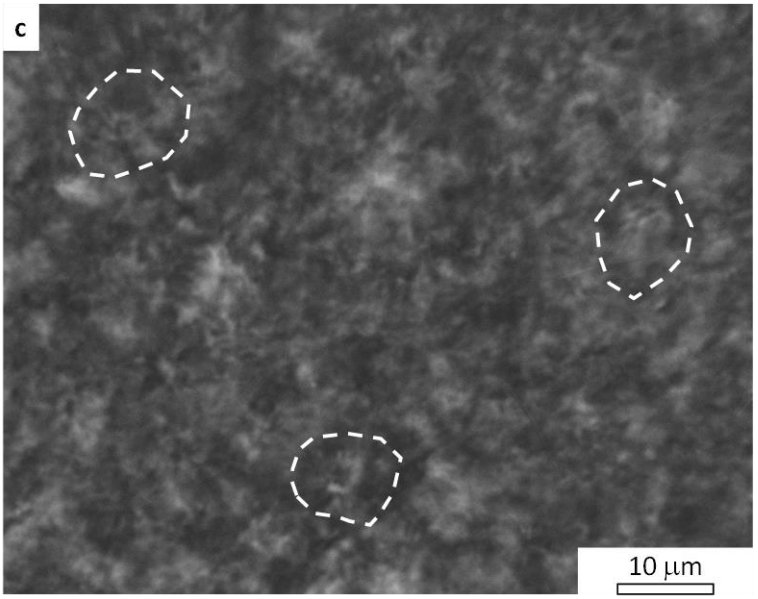

Figure 5-1.Micrographs of SLS PA-12 at 0° orientation (a) and at 90° orientation (b) and of IM PA-12 (c). Dotted lines delineate spherulite contours.

Figure 5-2 represents the diameter distribution versus the occurrence probability. The probability density was calculated using a normal distribution as the Kurtosis for all the materials reached values between 0.2 and 0.5, whereas the perfect Gaussian distribution takes values of 0 [163].

Table 5-3 collects the average spherulite diameter, $\overline{D}$, and the standard deviation, *s*, obtained from the measurements. No differences in average size and distribution are observed between *SLS* orientations, obtaining a mean spherulite size around 50 ± 10 μm. This is partly due to the fact that the average size of the spherulites depends upon the cooling conditions and the density of potential nucleating sites for crystallisation, being maintained in the *SLS* process for both orientations.

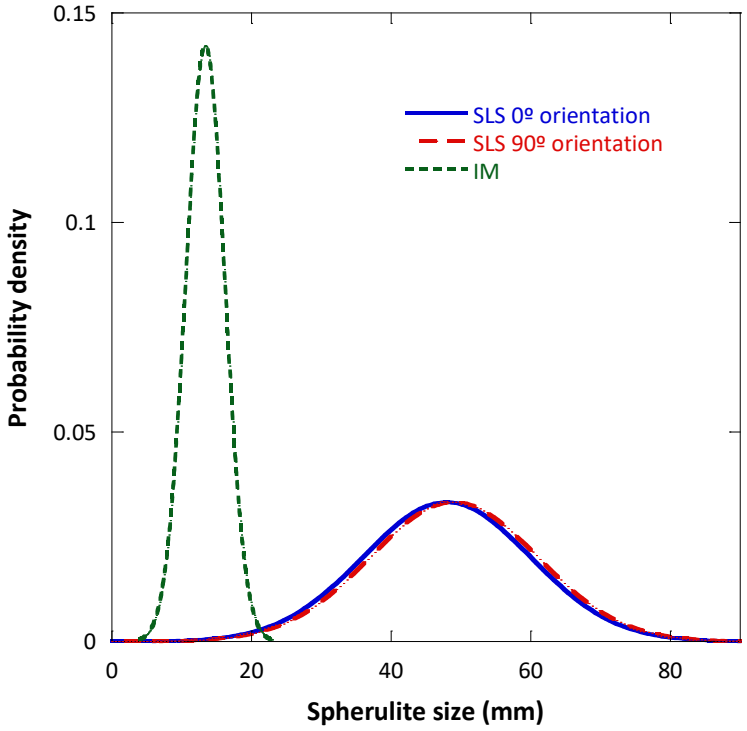

Figure 5-2. Spherulite size distribution for IM PA-12 and SLS PA-12 at 0° and 90° orientations.

It is also worth mentioning that the average values of spherulites are quite large and this can be explained by slower crystallisation kinetics during the *SLS* process and a lower nucleation density [142]. The spherulite size of the *IM* PA-12 is much finer, with average size of 13 ± 3 µm, four times lower than that of *SLS* PA-12. The differences in the spherulite size between the *SLS* and *IM* materials is caused by the thermal history during the manufacturing process. The *IM* material is fully molten before ejection and then cooled rapidly after injection. This rapid cooling allows less crystallisation growth. *SLS* material is also fully molten during laser sintering but the cooling rate is much lower allowing a much-developed transformation of the crystalline structure [164].

Table 5-3. Normal distribution parameters of the spherulite size of SLS PA-12 at 0° and 90° orientations and of IM PA-12: mean spherulitic diameter, $\overline{D}$, and standard deviation, s.

Material	$\overline{D}$ (μm)	s (μm)
SLS 0° orientation	48	12
SLS 90° orientation	49	12
IM	13	3

Moreover, in case of *IM* PA-12, a skin-core morphology was clearly observable in the cross-sectional samples (*Figure 5-3*), with a skin layer size around 14% of the total sample thickness. The spherulites were measurable in the core as they were not discernible in the surface layer, even with the inspection at the highest magnification of the optical microscope (x1482). The high level of molecular orientation together with the injection speed and the rapid cooling occurring during injection moulding may make difficult the crystallisation process in the skin. However, a micro-spherulitic structure in the core was observable (but always smaller than in *SLS*), due to a different temperature profile in the cooling stage to that undergone in the skin.

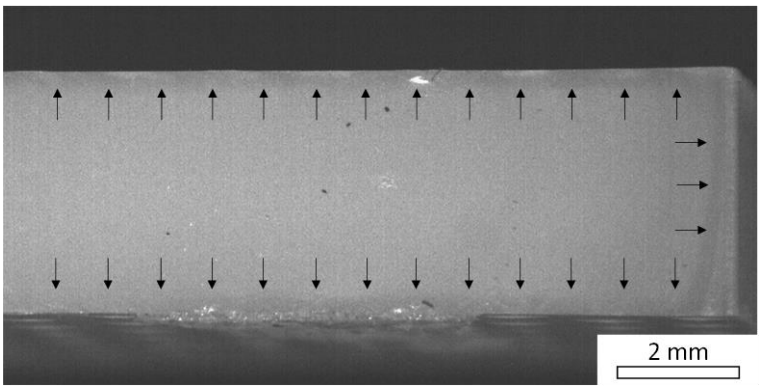

Figure 5-3. Cross-section of IM-PA12 with a core-skin morphology. The arrows indicate the skin of the material.

5.4 THERMAL CHARACTERISATION

The Differential Scanning Calorimetry (*DSC*) tests performed allow to obtain the thermograms shown in *Figure 5-4*. The crystallinity characteristics, the crystallization temperature, T_c, the melting temperature, T_m, and when observable, the glass transition temperature, T_g, can be computed from them and are collected in *Table 5-4*.

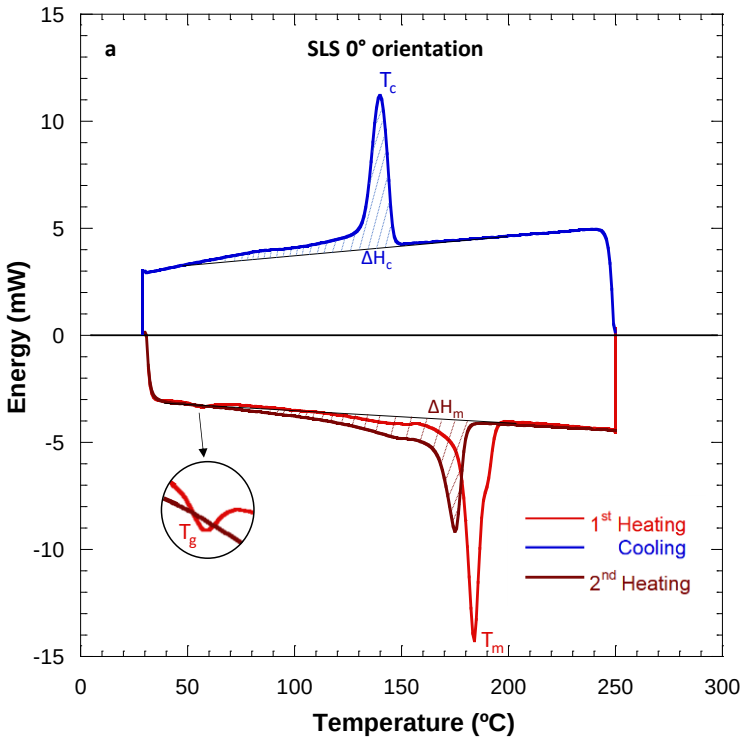

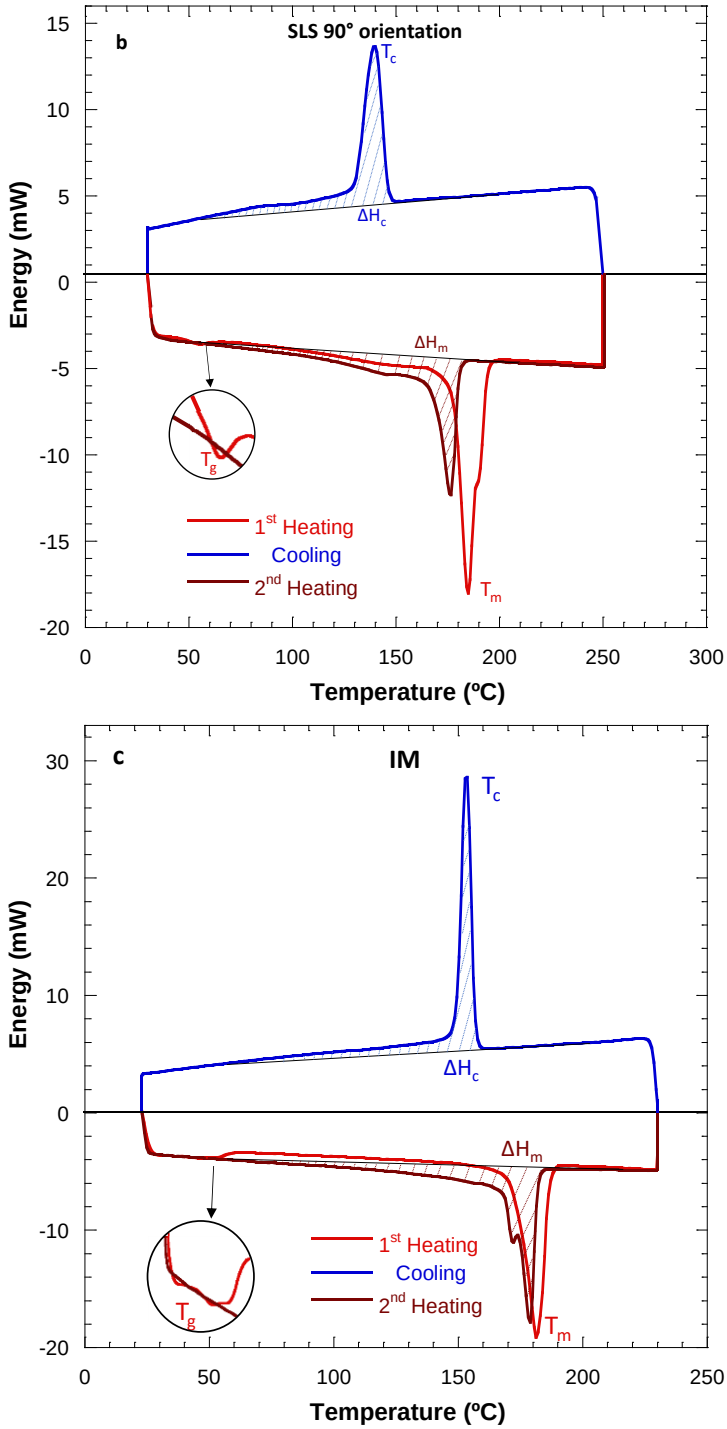

Figure 5-4: Thermographs obtained from DSC tests of SLS-PA 12 (a) at 0° orientation, (b) at 90° orientation and of (c) IM PA-12. The light red line represents the first heating of the test, the blue line shows the cooling process and the dark red line the second heating.

The thermal properties of *SLS* PA-12 at 0° and 90° orientations are almost identical, indicating that specimens at both orientations must have cooled at similar rates to give such consistent levels of crystallinity and temperatures. However, some differences were observed when comparing with *IM* PA-12. Specifically, *IM* specimens showed lower T_g, T_m and crystalline degrees, χ_c and χ_m, but higher T_C than *SLS* specimens. Once again, these differences are to do with the thermal history during the manufacturing process [165].

Table 5-4. Thermal properties obtained from DSC tests in SLS PA-12 specimens with different orientations and IM PA-12 samples.

	T_g (°C)	T_c (°C)	T_m (°C)	χ_c (%)	χ_m (%)
SLS 0° orientation	55.4	137.7	183.1	34.4	31.1
				Average	
				32.8 ± 2.3	
SLS 90° orientation	54.6	140.2	184.0	34.7	30.7
				Average	
				32.7 ± 2.8	
IM	50.6	151.3	180.7	37.1	36.8
				Average	
				37 ± 0.2	

Dynamic Mechanical Analysis (*DMA*) gave information about the loss modulus, the storage modulus and the loss factor (*tanδ*). *Figure 5-5* shows the evolution of these parameters from –110 °C to 170 °C for *SLS* PA-12 at 0° orientation in *Figure 5-5.a*, for *SLS* PA-12 at 90° orientation in *Figure 5-5.b* and for *IM* PA-12 in *Figure 5-5.c*. The storage modulus plot gives a full picture of the load-bearing characteristics of the material as a function of changes in temperatures, while *tanδ* curves identify the regions where relatively large changes in properties occur over relatively narrow bands of temperatures and, consequently, related

with material transition stages. Two obvious transitions at the ranges between 50 °C and 60 °C and between -60 °C and -70 °C are found independently of the processing technique in *Figure 5-5*. They are defined as the α and β relaxations, respectively.

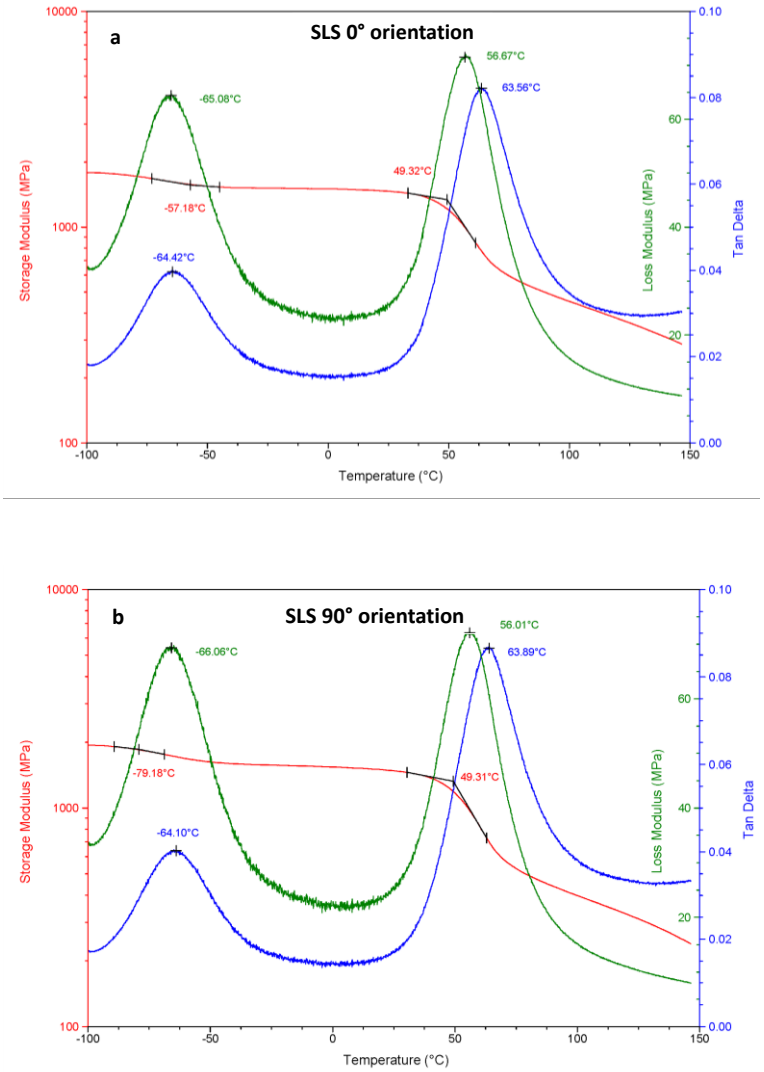

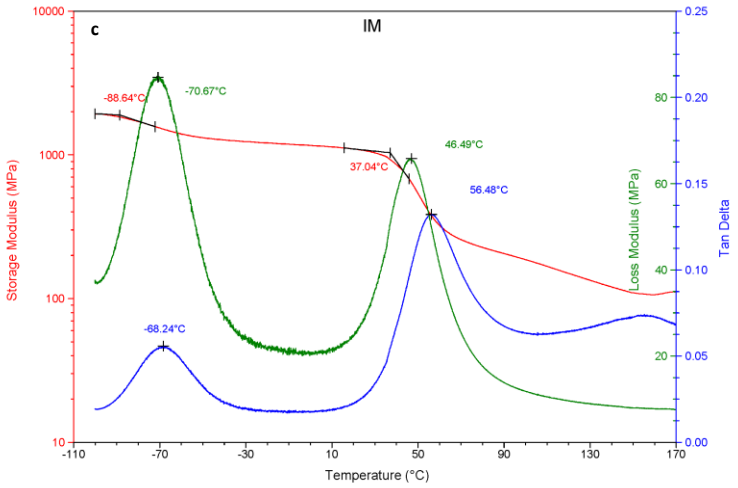

Figure 5-5. Thermal scans obtained from DMA tests containing the Storage Modulus, the Loss Modulus and the tanδ from -110 °C to 170 °C for: (a) SLS PA-12 at 0° orientation (b) SLS PA-12 at 90° orientation and (c) IM PA-12.

As known, the α-relaxation corresponds to the glass transition temperature, T_g, and displays the peak of greatest magnitude. The α-relaxation results from the rupture of hydrogen bonds between polymeric chains, which gives rise to the motion of long-chain segments in the amorphous region [165], [166]. On the other hand, the β-relaxation reflects the mobility of local hydrogen-bonded amide groups in the amorphous region and its appearance indicates that the material has good low temperature flexibility and cold endurance [165], [167]. *Table 5-5* collects the glass transition temperature and the β-transition temperature determined from the peaks of the $tan\delta$ curves. Firstly, these transitions are similar for both orientations in *SLS* specimens, confirming the no dependency with the manufacturing orientation. Nevertheless, both the glass transition temperature and the β-transition temperature in *IM* specimens shift to lower temperatures. This also occurred in *DSC* measurements (*Table 5-4*). The reason might be the faster crystallisation in the *IM* process, causing

an amorphous phase with more irregularly arranged molecular chain and better mobility, thus implying lower values of T_α and T_β [168].

Table 5-5 also shows the storage modulus at room temperature. As in other properties, there is no influence of the orientation on the storage modulus in *SLS* PA-12, but the value of the *IM* PA-12 specimens was almost 40% lower than the values of the *SLS* PA-12 samples. It is well settled that the Young´s moduli increase with the crystallinity degree [169], but the opposed behaviour observed in this case may be due to the presence of a no negligible skin layer of amorphous material together with a much smaller spherulitic structure.

Table 5-5. Transition temperatures, T_α and T_β, and storage modulus at room temperature obtained from DMA tests for IM PA-12 and for SLS PA-12 at 0° and 90° orientations.

	T_α (°C)	T_β (°C)	Storage modulus at 23°C (MPa)
SLS 0° orientation	63.6	-64.4	1472
SLS 90° orientation	63.9	-64.1	1488
IM	56.5	-68.2	1084

5.5 MECHANICAL PROPERTIES

Figure 5-6 and *Figure 5-7* show characteristic engineering stress-strain curves of *SLS PA-12* at 0° and 90° orientations, respectively, obtained from tensile tests at -50 °C, 23 °C and 50 °C. As expected, the mechanical response is strongly influenced by the temperature. At -50 °C, above T_β, *SLS* at 0° and 90° orientation presented semi-brittle behaviour due to the activation of mobility of side groups of the chain. For temperatures above T_g, that is, at 23 °C and 50 °C, the material displayed a ductile behaviour. As usually, the ductility decreased but the stiffness and the strength increased as the temperature reduced.

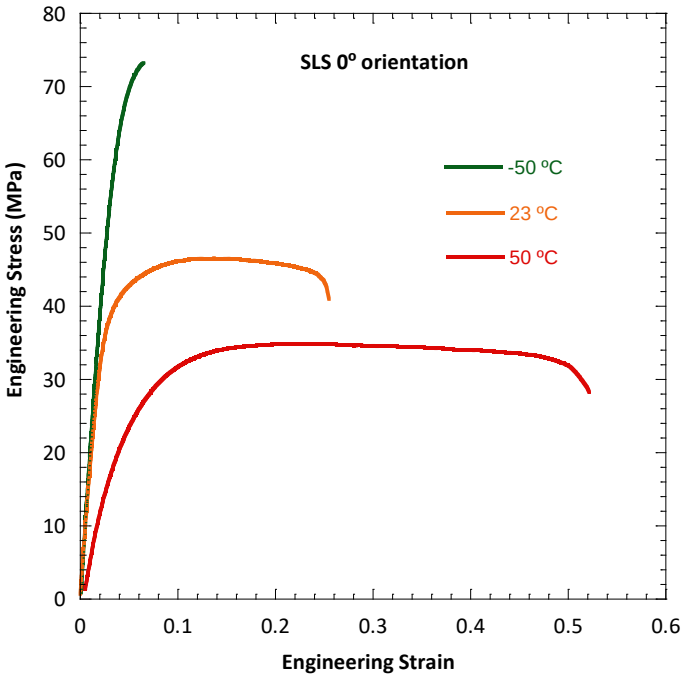

Figure 5-6. Characteristic engineering stress-strain curves at -50 °C, 23 °C and 50 °C obtained from tensile tests in SLS PA-12 at 0° orientation.

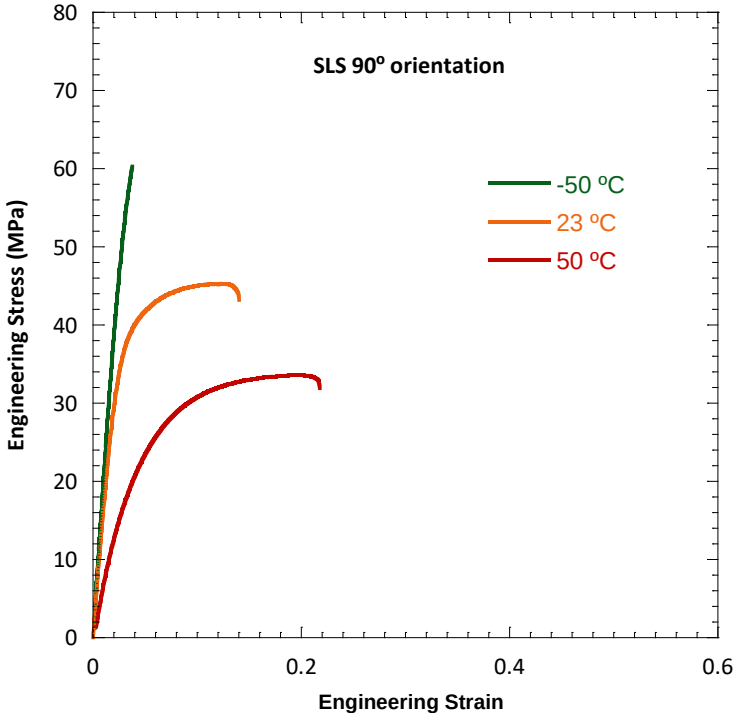

Figure 5-7. Characteristic engineering stress-strain curves at -50 °C, 23 °C and 50 °C obtained from tensile tests in SLS PA-12 at 90° orientation.

Figure 5-8 analyses the effect of orientation and manufacturing process on the tensile behaviour, showing clear differences. Firstly, *SLS* PA-12 presented higher strength and stiffness but lower ductility than *IM* PA-12. In addition, it is easily observed that in *SLS* material, the mechanical response at both orientations is similar except for the ductility.

Figure 5-9, Figure 5-10*, Figure* 5-11 and *Figure* 5-12 show the evolution of Young´s modulus, tensile strength, elongation at break and Poisson´s ratio with temperature, orientation and manufacturing process, respectively. Regarding Young´s modulus (*Figure 5-9),* the values decrease with the temperature increase, being this reduction more accentuated at 50 °C, due to the nearness to T_g (*Table 5-4*).

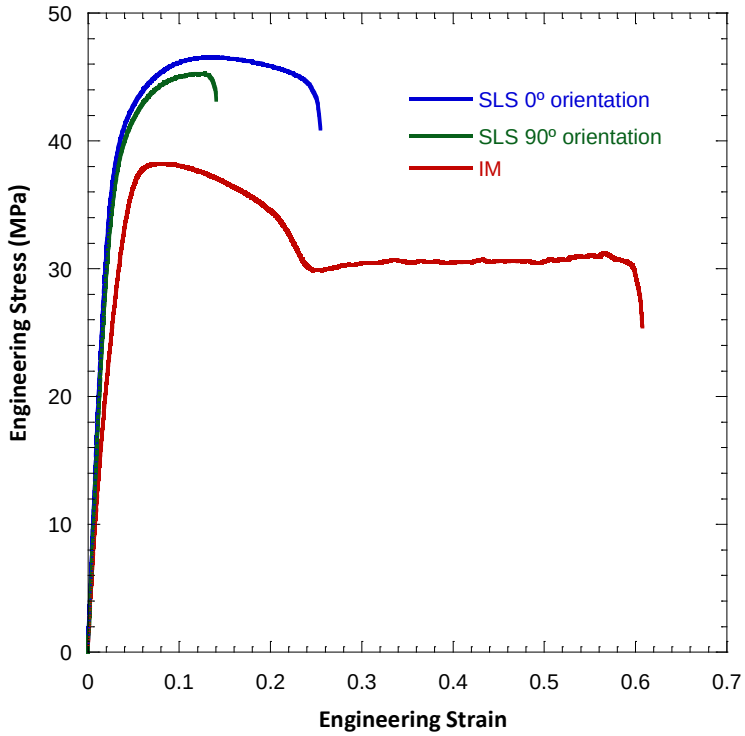

Figure 5-8. Characteristic engineering stress-strain curves at 23 °C obtained from tensile tests of IM PA-12 and of SLS PA-12 at 0° and 90°orientations.

For *SLS* PA-12, there were hardly differences in the Young's modulus with the orientation for the same temperature. On the other hand, *IM* PA-12 exhibited the lowest Young's modulus at room temperature, being 20% lower than the larger one corresponding with *SLS* PA-12 at 0° orientation.

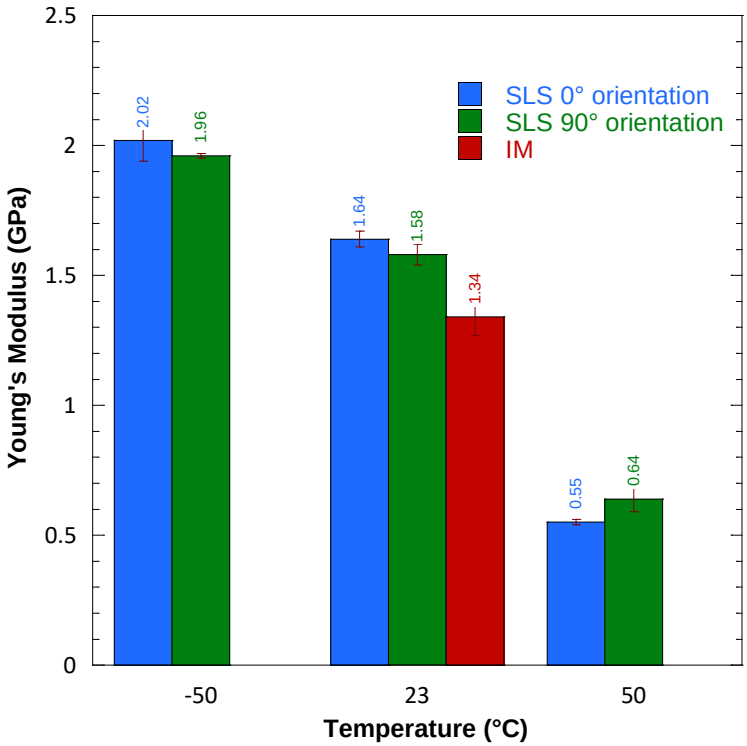

Figure 5-9. Evolution of the Young's modulus with temperature in SLS PA-12 at 0° and 90° orientations and with the manufacturing process at 23 °C.

The tensile strength followed the same trend as the Young's modulus (*Figure* 5-10): the higher the temperature, the lower the tensile strength at both orientations in *SLS* PA-12, and the lowest value at room temperature was obtained for *IM* PA-12. Concerning the orientation, *SLS* PA-12 at 0° orientation showed higher values than at 90° orientation, but the differences reduced as the temperature rose till reaching similar values at 50 °C.

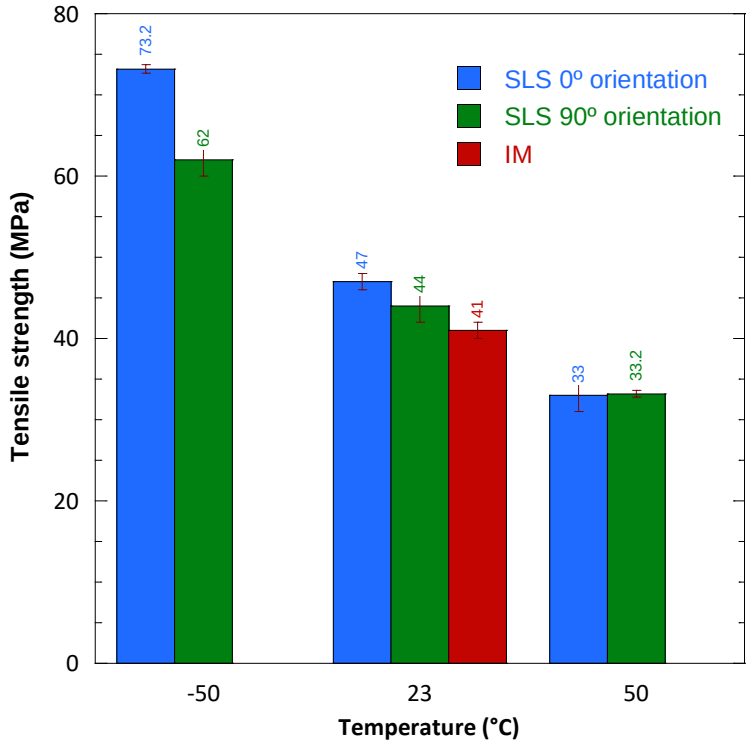

Figure 5-10. Evolution of the tensile strength with temperature in SLS PA-12 at 0° and 90° orientations and with the manufacturing process at 23 °C.

When analysing the influence of the temperature on the elongation at break (*Figure 5-11*) in *SLS* PA-12, the values of this parameter increases with temperature rising independently of the orientation. Nevertheless, the elongation at break at 0° orientation was more elevated than at 90° orientation at any temperature, registering the higher difference at 50 °C, with values at 0° orientation 3 times larger than those at 90° orientation. The proximity of 50 °C to the T_g of the material was the reason of this significant increase because the mobility of large scale coordinated motions of the polymer chains occurs, resulting in a massive relaxation of the material. At room temperature, the elongation at break of *IM* PA-12 is more than twice the value measured in *SLS* PA-12 at 0° orientation.

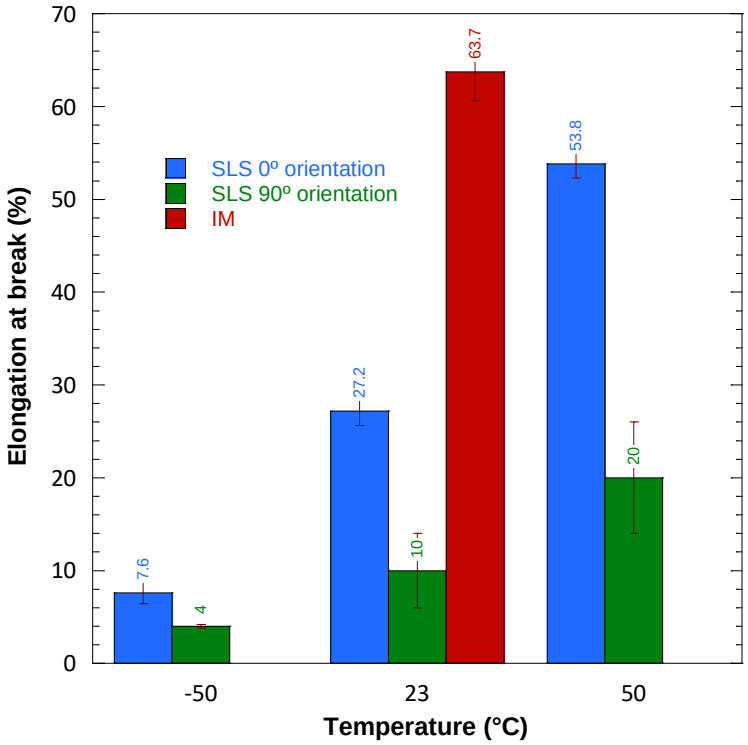

Figure 5-11. Evolution of the elongation at break with temperature in SLS PA-12 at 0° and 90° orientations and with the manufacturing process at 23°C.

Regarding the Poisson's ratio, *Figure* 5-12 shows increments with temperature, having the 0° orientation the largest value for *SLS* PA-12 at the three tested temperatures but being overtaken by the value of *IM* PA-12 at room temperature.

These results match with the existing bibliography (*section 2.2.1, Table 2-1*). Firstly, the Young's modulus and the tensile strength of *IM* PA-12 were smaller than those of *SLS* PA-12 despite the higher crystallinity degree of the former (Table 5-4). *Crist et al.* [141], [169] stated the opposite trend, the higher the crystallinity degree the higher the elastic modulus and the tensile strength. Nevertheless, the presence of an amorphous skin layer with significant dimensions in the *IM* PA-12 is an important factor to have in mind. Also, a

different spherulite size between *SLS* PA-12 and *IM* PA-12 seems to affect the elongation at break [170]. Results obtained in *SLS* specimens at 23°C are analogous to those of Seltzer et al. [31], Caulfied et al. [33], Stichel et al. [34], Munguia et al. [118], [119], Xu et al.[161], Mousa [171] and Hao et al. [172]. Finally, the results obtained in *IM* PA-12 are comparable to those reported by Hooreweder et al. [30].

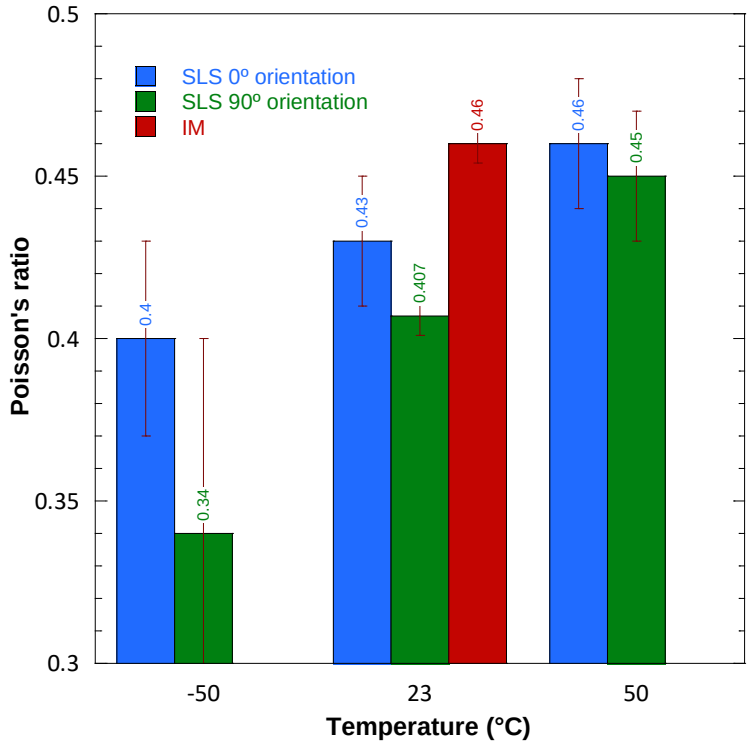

Figure 5-12. Evolution of the Poisson's ratio with temperature in SLS PA-12 at 0° and 90° orientations and with the manufacturing process at 23 °C.

5.5.1. Tensile tests fractographies

SEM fractographies were taken from the fracture surfaces of the tensile test specimens to study the effect of temperature, orientations and manufacturing processes, identifying the micromechanisms of deformation and fracture.

Figure 5-13 and *Figure 5-14* show the fracture surfaces at -50 °C, 23 °C and 50 °C of *SLS* PA-12 at 0° and 90° orientations, respectively. The common trend observed in both orientations was an increment in the surface smoothness with lower temperatures. However, there are several differences between the *SLS* orientations.

There is no influence of the orientation on the morphology of the fracture surfaces at -50 °C (*Figure 5-13.a* and *Figure 5-14.a*). The morphology was irregular, identical to those observed by other authors [173]. The similarity of the fracture morphology is consistent with the values of the tensile parameters, specially the elongation at break (*Figure* 5-11), which were identical at this low temperature for both orientations.

At 23 °C (*Figure 5-13.b* and *Figure 5-14.b*), the fracture surface at 0° orientation is much rougher than those resulting from tests at -50 °C, being characterized by the presence of voids surrounded by amorphous filaments of PA-12, which had been stretched and finally broken along the crack growth direction. These features are associated with the nucleation, growth and coalescence of crazes, which is a phenomenon commonly observed in thermoplastic polymer fractures [174].

SLS 0° orientation

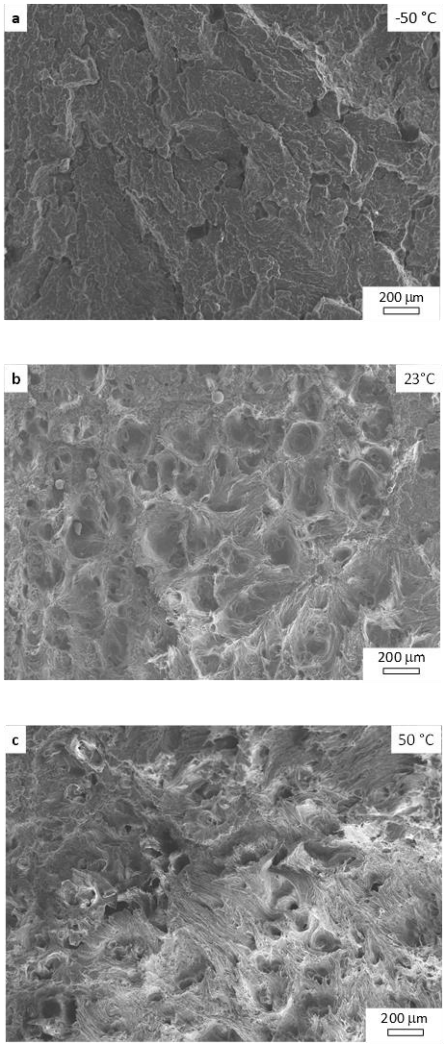

Figure 5-13. Fracture surfaces from tensile tests of SLS PA-12 at 0° orientation at different temperatures: (a) -50°C, (b) 23°C and (c) 50°C

SLS 90° orientation

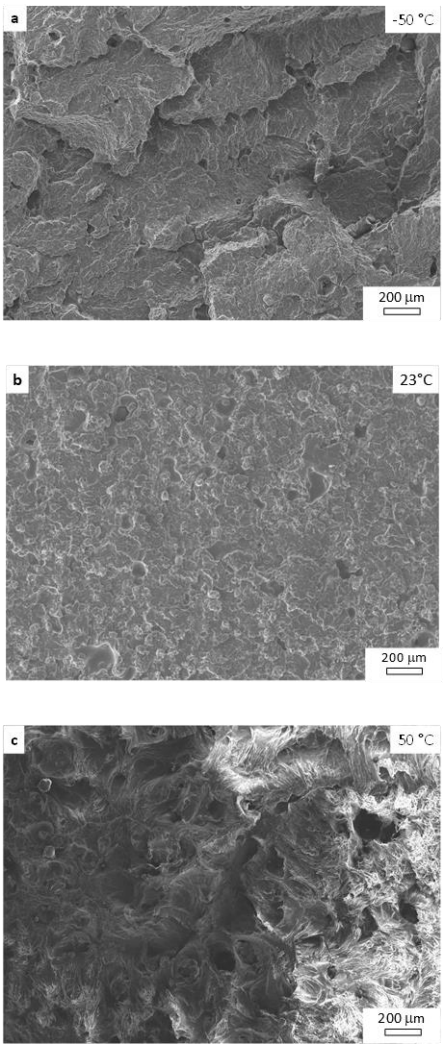

Figure 5-14. Fracture surfaces from tensile tests of SLS PA-12 at 90° orientation at different temperatures: (a) -50°C, (b) 23°C and (c) 50°C

The nucleation site could be at defects as pores or interspherulitic areas. The stretched filaments surrounding voids are displayed in *Figure 5-15*. On the other hand, the 90° orientation exhibits a plain surface with no evidence of plastic deformation of filaments but where pores and unmolten particles are

discernible. This distinct morphologies at different loading directions are in accordance with the elongation at break values (*Figure* 5-11*)*, specifically the increase in surface roughness goes hand in hand with the increase in the elongation at break.

Finally, the fractographies of specimens tested at 50 °C (*Figure 5-13*.c and *Figure 5-14.c*) show a much higher ductile deformation of the amorphous filaments than at 23 °C, and when comparing the orientations, the specimens tested at 0° orientation presented more tearing than at 90° orientation. In this case, the ductile behaviour is enhanced with the closeness to the material T_g (*Table 5-4*). The high mobility of the molecular boosts the ductile tearing along the load direction at both orientations. Once again, this fractographic morphologies agree with the elongation at break results (*Figure* 5-11), which are the highest of all the tested temperatures and with values at 0° orientation more than twice those measured at 90° orientation.

To determine the effect of the processing technique, *Figure 5-16* shows the fracture surface of *IM* PA-12. The panoramic view (*Figure 5-16.a)* evidences that the failure starts at a surface defect (outlined in black dashed line) followed by macroscopic plastic deformation of the gage length with the formation of a necking zone which propagates along the specimen. The high level of plastic deformation undergone by the amorphous filaments is in agreement with the high values of elongation at break (*Figure 5-11)*. The detailed view (*Figure 5-16.b*) clearly denotes the stretched gage length broken after ductile tearing.

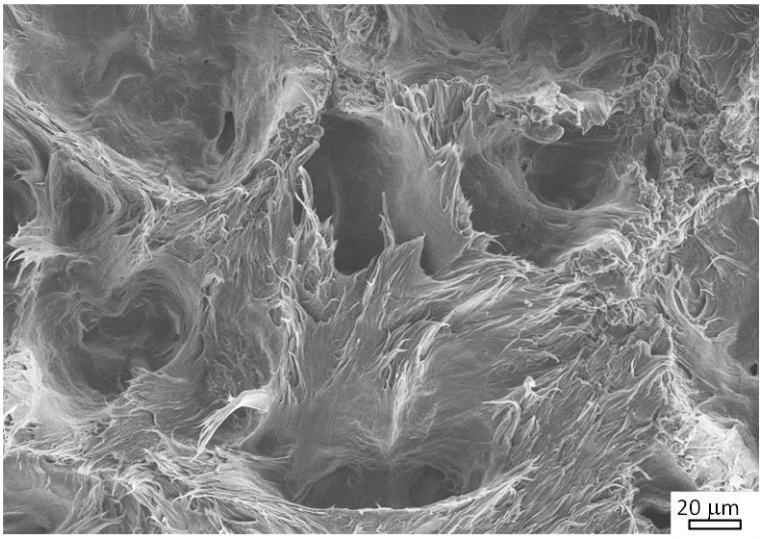

Figure 5-15. Detail of crazing mechanism: voids surrounded by amorphous stretched and broken PA-12 filaments.

Moreover, there is complete lack of defects in form of pores or unmolten particles. Therefore, the crazing mechanism together with the presence of internal defects may be the reason why the ductility at failure of the *SLS* PA-12 is much lower than that of *IM* PA-12 [168].

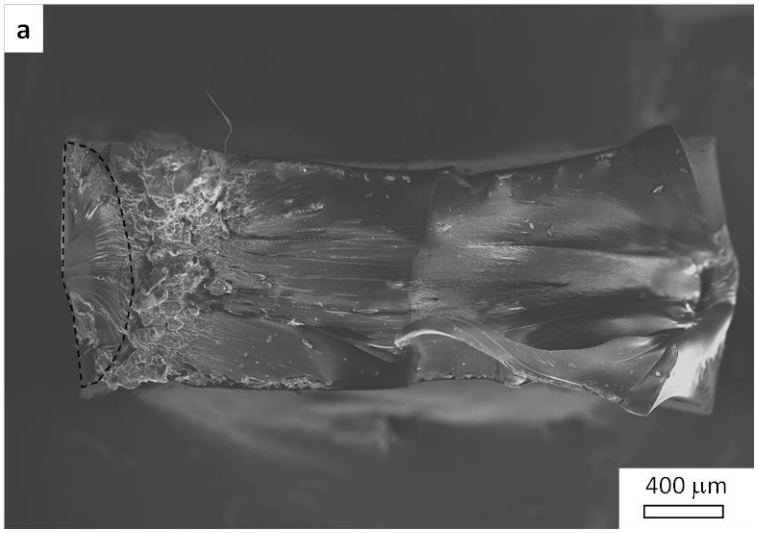

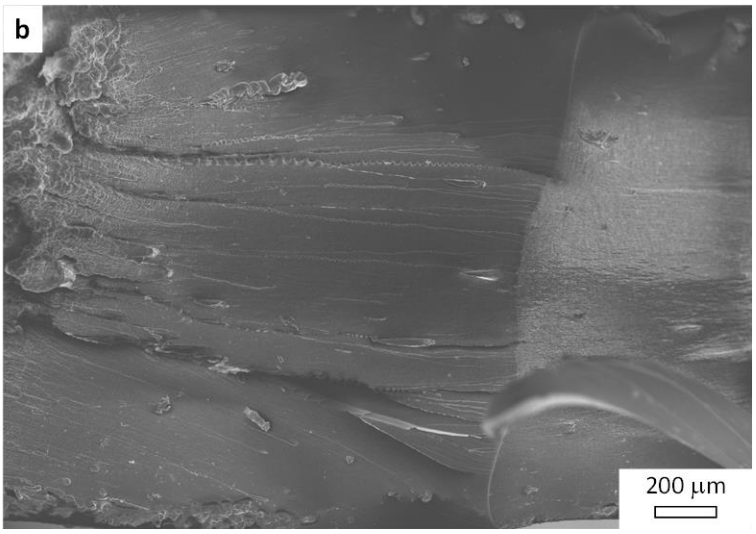

Figure 5-16. Fracture surfaces from tensile tests of IM PA-12 at 23°C: (a) panoramic view with the surface defect starter of failure delimited with a dotted line, (b) detail of ductile tearing.

5.6 FRACTURE BEHAVIOUR

For the determination of the fracture parameters, different approaches were applied depending on the mechanical response of the material at each experimental condition as described in the *section 4.6.2.*

Figure 5-17 shows the representative load-displacement records obtained from fracture tests at -50 °C of *SLS* PA-12 at 0° and 90° orientations. Despite the semi-brittle behaviour, all the requirements of the *LEFM* approach were fulfilled, so the recommendations of ISO 13856 standard [149] were followed to determine the critical stress intensity factor, K_{IC}, and the critical energy release rate, G_{IC}.

Figure 5-18 displays the representative load-displacement records obtained from fracture tests at 23 °C of *IM* PA-12 and of *SLS* PA-12 at 0° and 90° orientations.

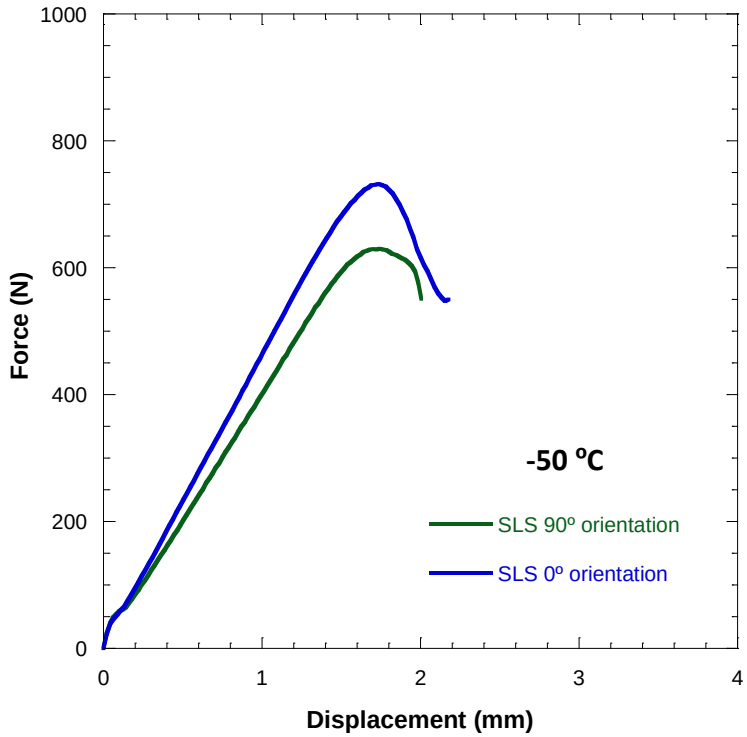

Figure 5-17. Representative load-displacement curves obtained from fracture tests at -50 °C of SLS PA-12 at 0° and 90° orientations.

The difference in stiffness is mainly due to the different initial crack lengths. The behaviour of *IM* PA-12 specimens and both orientations of *SLS* PA-12 samples was also semi-brittle but, at this temperature, not all the tests verified the linearity criterion, because there were some tests which deviated from the linearity, as the $\frac{P_{max}}{P_Q}$ ratio exceeded narrowly 10%. Therefore, the two approaches, *LEFM* and *NLFM*, were applied at 23 °C despite most of the tests complied with the *LEFM* requirements. The normalization method described in ASTM E1820 standard [150] was followed to determine the J-R curve and the energy at crack growth initiation, J_{IC}, and the G_{IC} values provided by *LEFM* were also calculated.

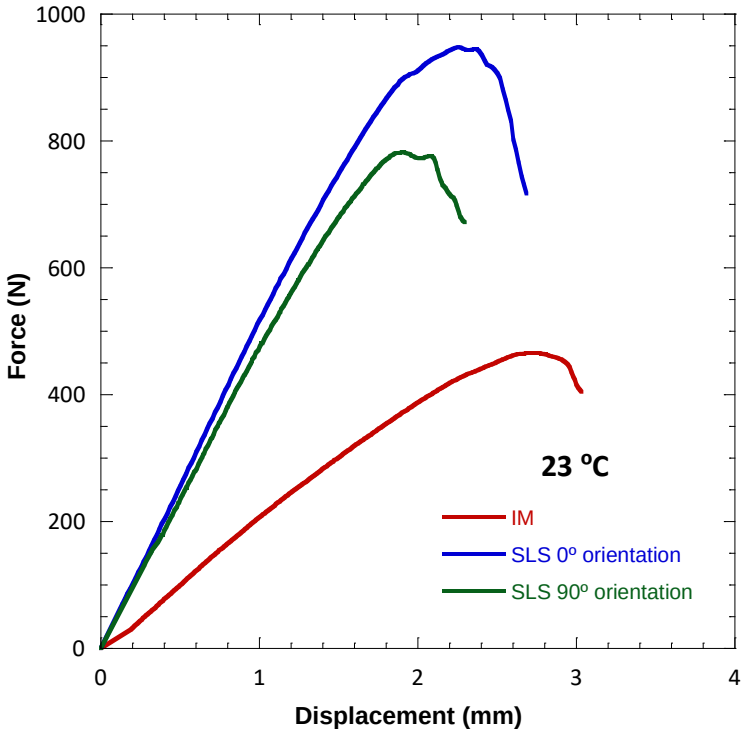

Figure 5-18. Representative load-displacement curves at 23 °C obtained from fracture tests of IM PA-12 and of SLS PA-12 at 0° and 90° orientations.

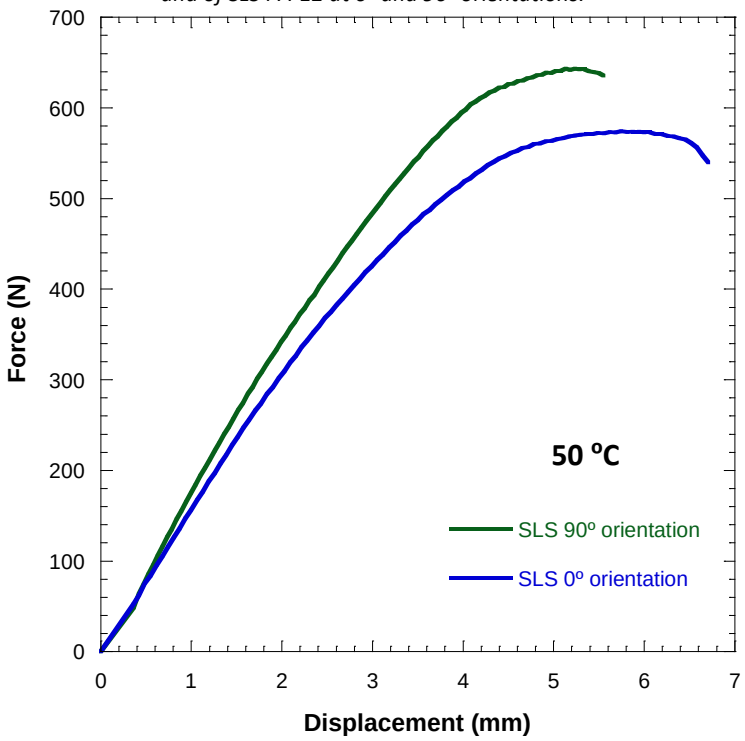

Figure 5-19. Representative load-displacement curves at 50 °C obtained from fracture tests of SLS PA-12 at 0° and 90° orientations.

Finally, *Figure 5-19* includes the representative load-displacement records of the fracture test at 50 °C of *SLS* PA-12 at 0° and 90° orientations. The non-linearity was so high that the application of *NLFM* approach was undoubtful and the normalization method was used to determine the J-R curve and J_{IC} values.

Figure 5-20 shows the evolution of the fracture toughness in terms of the stress intensity factor, K_{IC}, when computable, with the temperature, the load orientation for *SLS* PA-12 and the manufacturing technique. Firstly, all the values were in plane strain conditions. As expected, K_{IC} values decrease as the temperature increases in *SLS* PA-12. Regarding the effect of the orientation, the values of K_{IC} obtained at 90° orientation were lower than at 0° orientation. The values of K_{IC} at 23 °C computed in this investigation were comparable to those obtained by Seltzer et al. [31] and by Salazar et al. [39], but higher than those obtained by Linul et al. [46]. The discrepancy in this case has to do with the low density of the parts measured by the latter, correlated with the values of the manufacturing parameters employed.

Attending to the effect of the manufacturing technique at 23 °C, no differences between *IM* PA-12 and *SLS* PA-12 results were found.

Within the computation of the fracture parameters under the *NLFM* approach, *Figure 5-21* and *Figure 5-22* show the J-R curves at 23 °C and 50 °C of SLS PA-12 at 0° and 90° orientations, respectively. Firstly, the J-R curves at 50 °C were all above those at 23 °C independently of the load direction with respect to the layered structure. Secondly, for the very same temperature, the J-R curves of *SLS* PA-12 at 0° orientation were above and steeper than those of *SLS* PA-12 at 90° orientation.

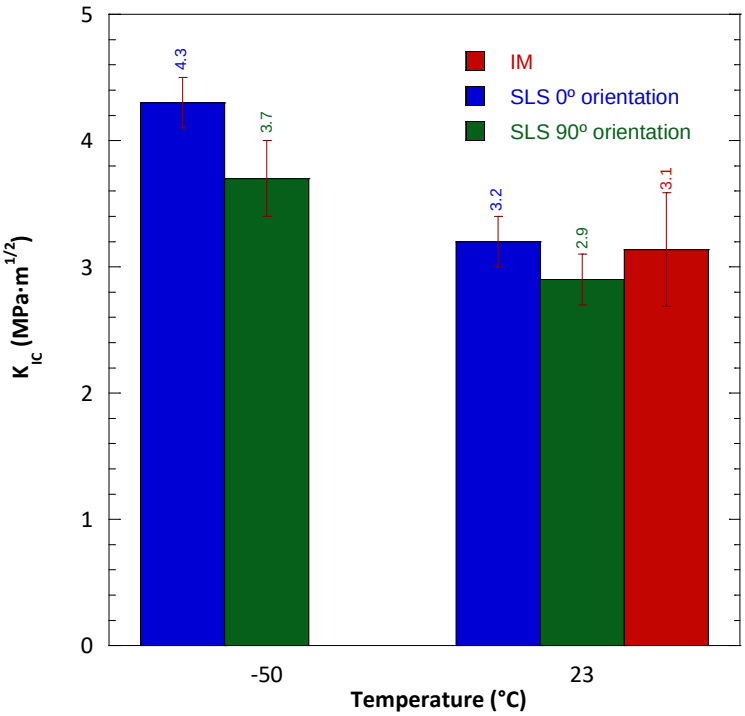

Figure 5-20. Fracture toughness of SLS PA-12 at 0° and 90° orientations determined at -50 ℃ and at 23 ℃ and of IM PA-12 at 23 ℃.

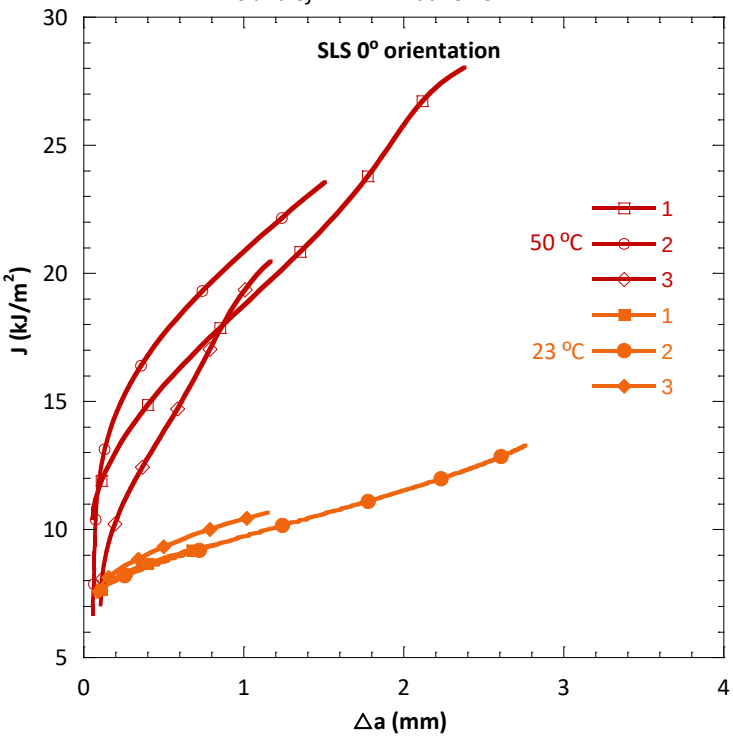

Figure 5-21. Influence of the temperature in SLS PA-12: J-R curves at 23 °C and 50 °C of SLS PA-12 at 0° orientation.

To investigate the effect of the manufacturing process, *Figure 5-23* compares the J-R curves at 23 °C of *SLS* PA-12 at 0° and 90° orientations with those obtained from *IM* PA-12. Firstly, regarding *SLS* materials, the energy needed to produce the stable crack growth at 0° orientation is higher than that at 90° orientation, being the latter less resistant against crack growth. Secondly, the J-R curves of *IM* PA-12 presented a high dispersion but in average the behaviour was in between that of *SLS PA-12* at 0° orientation and that of *SLS PA-12* at 90° orientation.

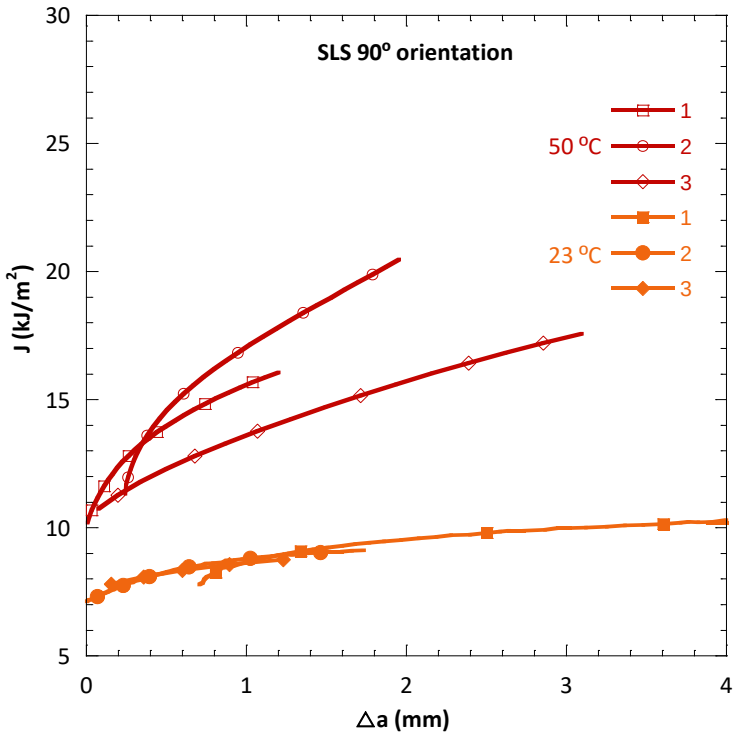

Figure 5-22. Influence of the temperature in SLS PA-12: J-R curves at 23 °C and 50 °C of SLS PA-12 tested at 90° orientation.

Table 5-6 collects the quantification of all these differences, more specifically, the values of the exponent N_J and of the parameter C_J of the potential law with the form $J = C_J \Delta a^{N_J}$, which has been used to fit the experimental values. Firstly, the exponent N_J and the parameter C_J increased when the temperature

increased at both orientations of *SLS* PA-12. Secondly, at the same temperature, the higher values of the exponent N_J of *SLS* PA-12 at 0° orientation in comparison with those of *SLS* PA-12 at 90° orientation confirm the trend observed graphically.

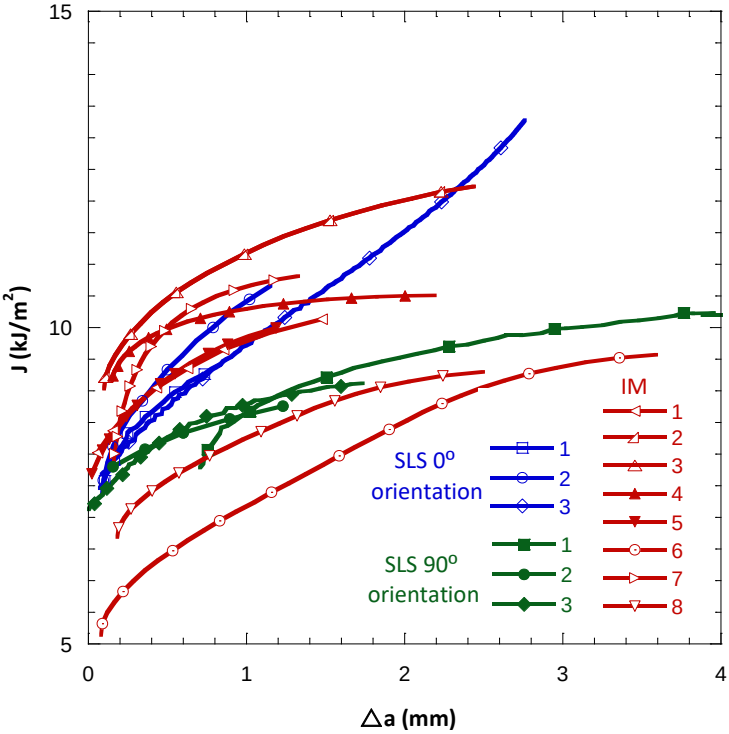

Figure 5-23.Influence of the manufacturing process at 23 °C: J-R curves of SLS PA-12 at 0° and 90° orientations and of IM PA-12.

Finally, although *IM* PA-12 exhibits an average behaviour between that of *SLS* PA-12 at 0° orientation and that of *SLS* PA-12 at 90° orientation, the curves were more like those of *SLS* PA-12 at 90° orientation, implying similar N_J coefficients.

Figure 5-24 shows the energy at crack growth initiation, J_{IC} and G_{IC}, as a function of temperature, orientation for *SLS* PA-12 and processing technique at 23 °C. Regarding the effect of the temperature in *SLS* PA-12, there is an important increment in the J_{IC} values obtained at 50 °C, which nearly doubled those at 23 °C.

Table 5-6. Fitting values of the experimental J-R curves to the power law equation $J = C_J \Delta a^{N_J}$ at 23 °C and 50 °C of SLS PA-12 tested at 0° and 90°orientations and of IM PA-12 tested at 23 °C.

	***SLS* 0° orientation**			***SLS* 90° orientation**			***IM***		
	Specimen ID	C_J	N_J	**Specimen ID**	C_J	N_J	**Specimen ID**	C_J	N_J
23 °C	**1**	9.53	0.01	***1***	8.56	0.14	***1***	9.70	0.07
							2	9.74	0.08
	2	10.3	0.13	***2***	8.61	0.06	***3***	11.22	0.09
							4	10.25	0.05
							5	7.52	0.17
	3	10.2	0.18	***3***	8.66	0.06	***6***	10.84	0.15
							7	8.32	0.12
	Average	10.0 ± 0.4	0.14 ± 0.04	***Average***	8.61 ± 0.05	0.08 ± 0.05	***Average***	9.6 ± 1.3	0.10± 0.04
50 °C	**1**	20.1	0.26	***1***	15	0.1			
	2	21.7	0.31	***2***	14	0.14			
	3	18.8	0.40	***3***	17	0,25			
	Average	20.2 ± 1.5	0.32 ± 0.07	***Average***	15.3 ± 1.5	0.13 ± 0.09			

This behaviour can be explained considering that 50 °C is close to the T_g of the material (*Table 5-4*), so the viscous state plays a notable role in the fracture behaviour, requiring more energy for crack growth initiation.

It can be remarkable the similarity of G_{IC} and J_{IC} obtained at 23 °C for *SLS* PA-12 at 0° and 90° orientations, without statistical differences between them. Meanwhile at -50 °C and at 50 °C, the fracture energy of *SLS* PA-12 at 0° orientation is higher than that of *SLS* PA-12 at 90° orientation.

Finally, the values of G_{IC} and J_{IC} of *IM* PA-12 were higher than those of *SLS* PA-12, showing the best crack growth initiation resistance.

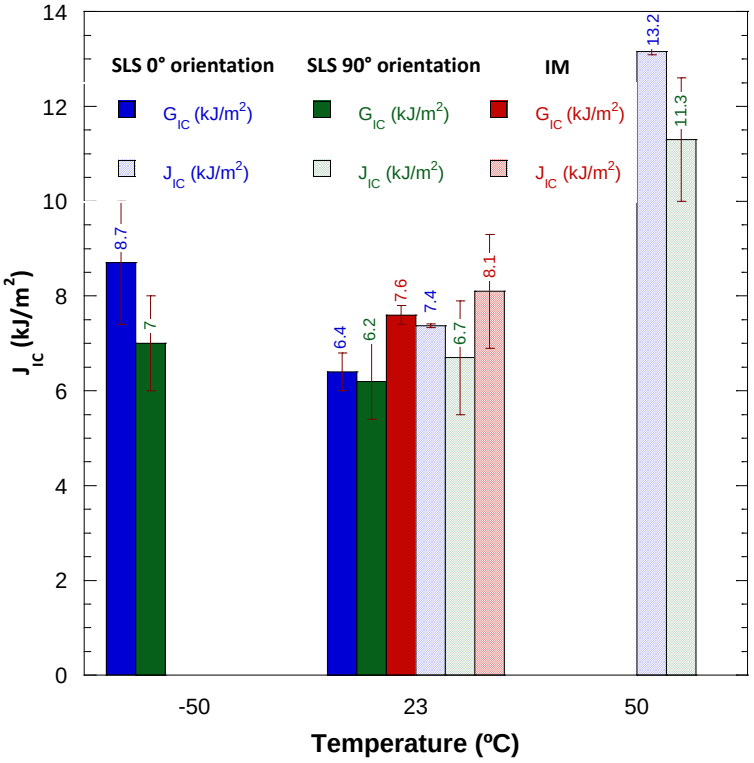

Figure 5-24. Energy at crack growth initiation as a function of the testing temperature and the orientation in SLS PA-12. The influence of the manufacturing technique at 23°C is also displayed including the values obtained from IM PA-12 fracture specimens.

5.6.1. Fractographic analysis of fracture tests

Figure 5-25 and Figure 5-26 display the fracture surfaces obtained from fracture tests carried out at -50 °C, 23 °C and 50 °C of *SLS* PA-12 at 0° and 90° orientations, respectively. It is important to mention that all *SLS* PA-12 fracture surfaces presented defects in form of pores or unmolten powder particles.

Independently of the orientation, the morphology of the fracture surfaces at -50 °C (*Figure 5-25.a* and *Figure 5-26.a*) and at 23 °C (*Figure 5-25.b* and *Figure 5-26.b*) presented small differences. The characteristic feature is a patchwork pattern with more evident deformed borders at 23 °C. However, at 50 °C the degree of plastic deformation is more pronounced with presence of voids

SLS 0° orientation

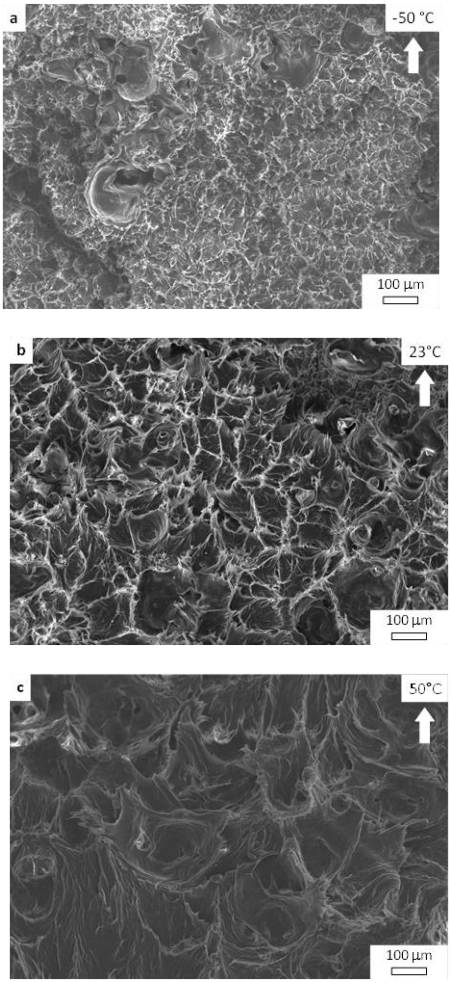

Figure 5-25. Fracture surfaces of SLS PA-12 at 0° orientation tested at: (a) -50°C, (b) 23°C and (c) 50°C. The arrow shows the crack growth direction.

SLS 90° orientation

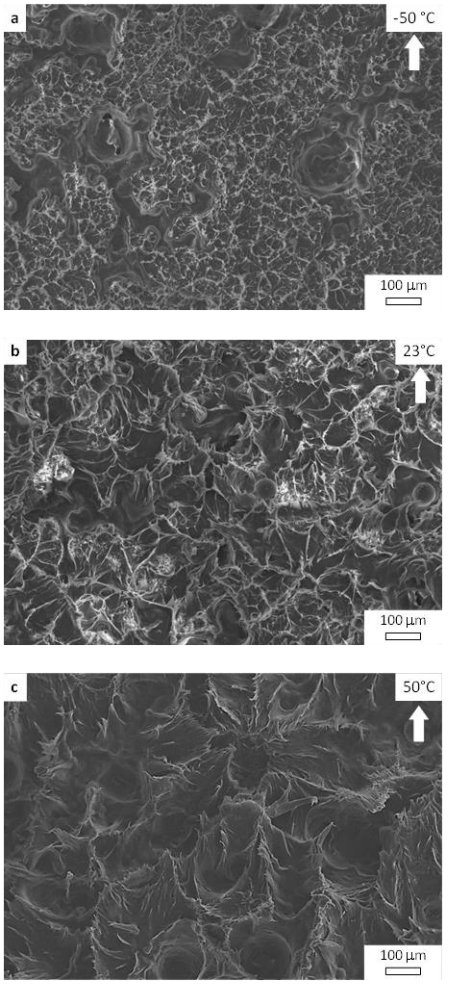

Figure 5-26. Fracture surfaces of SLS PA-12 at 90° orientation tested at: (a) -50°C, (b) 23°C and (c) 50°C. The arrow shows the crack growth direction.

However, at 50 °C the degree of plastic deformation is more pronounced with presence of voids through the ductile tearing of the amorphous filaments along the crack propagation direction (*Figure 5-25.c* and *Figure 5-26.c*). This fractographic analysis agrees with the fracture toughness values collected in *Figure 5-24.*

No differences could be detected between the fracture surfaces of the *SLS* specimens tested at 0° and 90° orientations at all the testing temperatures. This fact matches with the indistinguishable values of the fracture energy at both orientations, except for those at 50 °C (*Figure 5-24*).

The dominant failure mechanism is crazing, characterized by the nucleation of microvoids followed by their growth (*Figure 5-27*) and final coalescence, leaving behind craters with more or less stretched amorphous filaments. The evolution of this damage mechanism during crack growth advancement leaves the patchwork pattern previously described. As the temperature rises, the dimples associated with crazing can be less visible due to the high elongation of surrounding filaments along the crack propagation direction.

Comparing this fractographic morphology with the analysis carried out by Karger-Kocsis and Friedrich in injection molded polyamide 6.6 [80], the nucleation sites of the craze micromechanism could be related with defects as pores or unmolten particles as well as the crystalline structure.

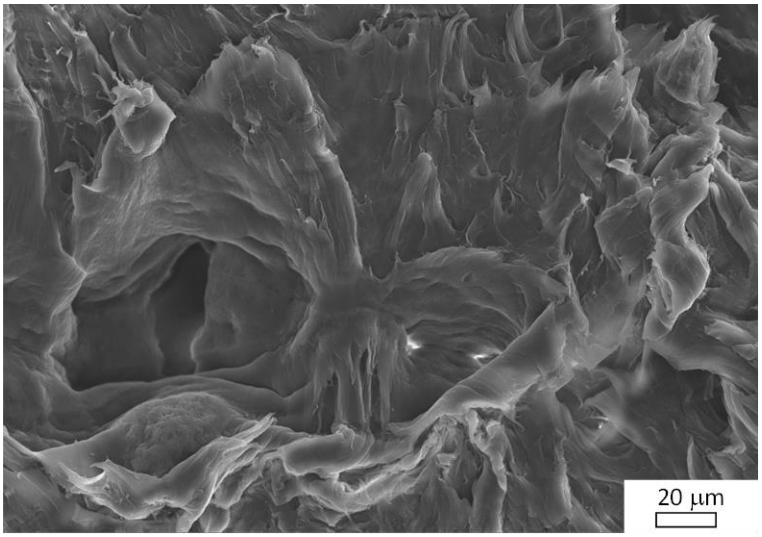

Figure 5-27. Detail of "Crazes" observed at 23°C.

Figure 5-28 shows the fracture surface of *IM* PA-12. In this case, the patchwork pattern is much finer and more homogeneous than that observed in *SLS* PA-12 (*Figure 5-25* and *Figure 5-26*), and what is more, the fracture surfaces were free of unmolten particles or defects.

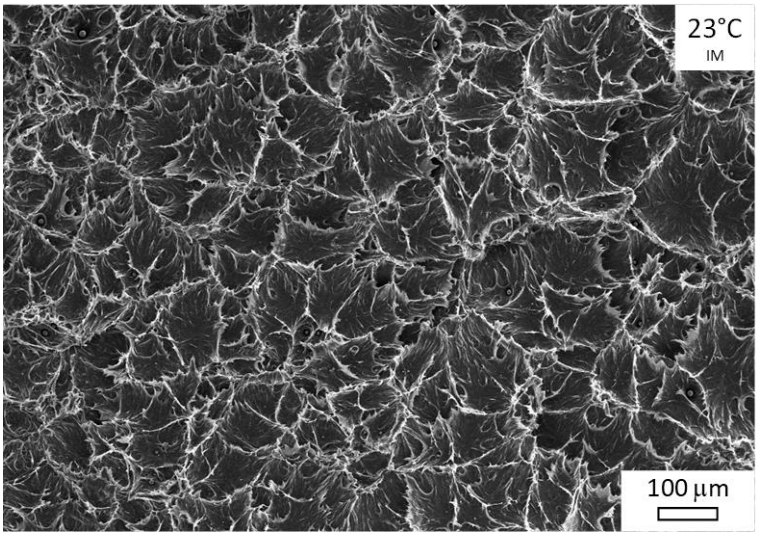

Figure 5-28. Fracture surface obtained from fracture tests of IM PA-12 at 23°C.

The finer size of the patch in the *IM* samples could be related to the small size of the crystalline structure (*Table 5-3*), together with the lack of processing defects, providing higher values of the fracture toughness (*Figure 5-24*). As stated by Salazar et al. [175], the decrease of the crystalline size favors the number and flexibility of the molecular chains in charge of holding together the lamellae bundles and consequently, improves the fracture energy. The reason is that the fracture toughness is governed, among other factors, by the energy required for the deformation and break of these tie molecules. Therefore, the higher the number of tie molecules, the higher the fracture energy.

5.7 FATIGUE CRACK GROWTH BEHAVIOUR

Figure 5-29 shows the fatigue crack growth curves as a function of the control parameter $\Delta\sqrt{G}$ of *SLS* PA-12 at 0° orientation (*Figure 5-29.a)* and at 90° orientation (*Figure 5-29.b)*, and of *IM* PA-12 (*Figure 5-29.c)*. The log-log plots of $\frac{da}{dN}$ versus $\Delta\sqrt{G}$ graphs displayed in *Figure 5-29* only shows region II, a linear relationship between the crack growth rate and the control parameter described by the Paris law (or *eq. (2-2)*) and region III, dependent on the fracture toughness K_{IC} as the crack growth rates approach instability. The reason is that these curves were achieved from constant load amplitude tests or $\Delta\sqrt{G}$-increasing tests.

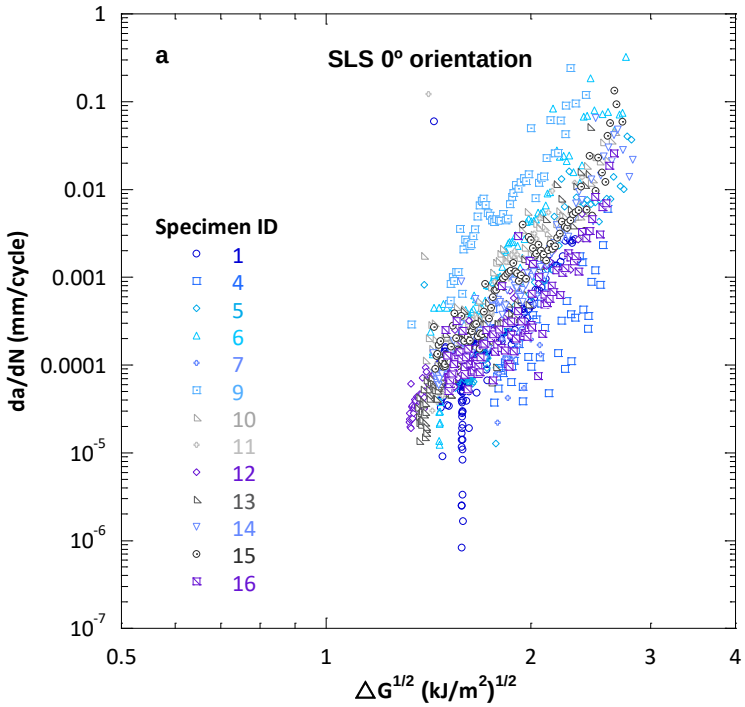

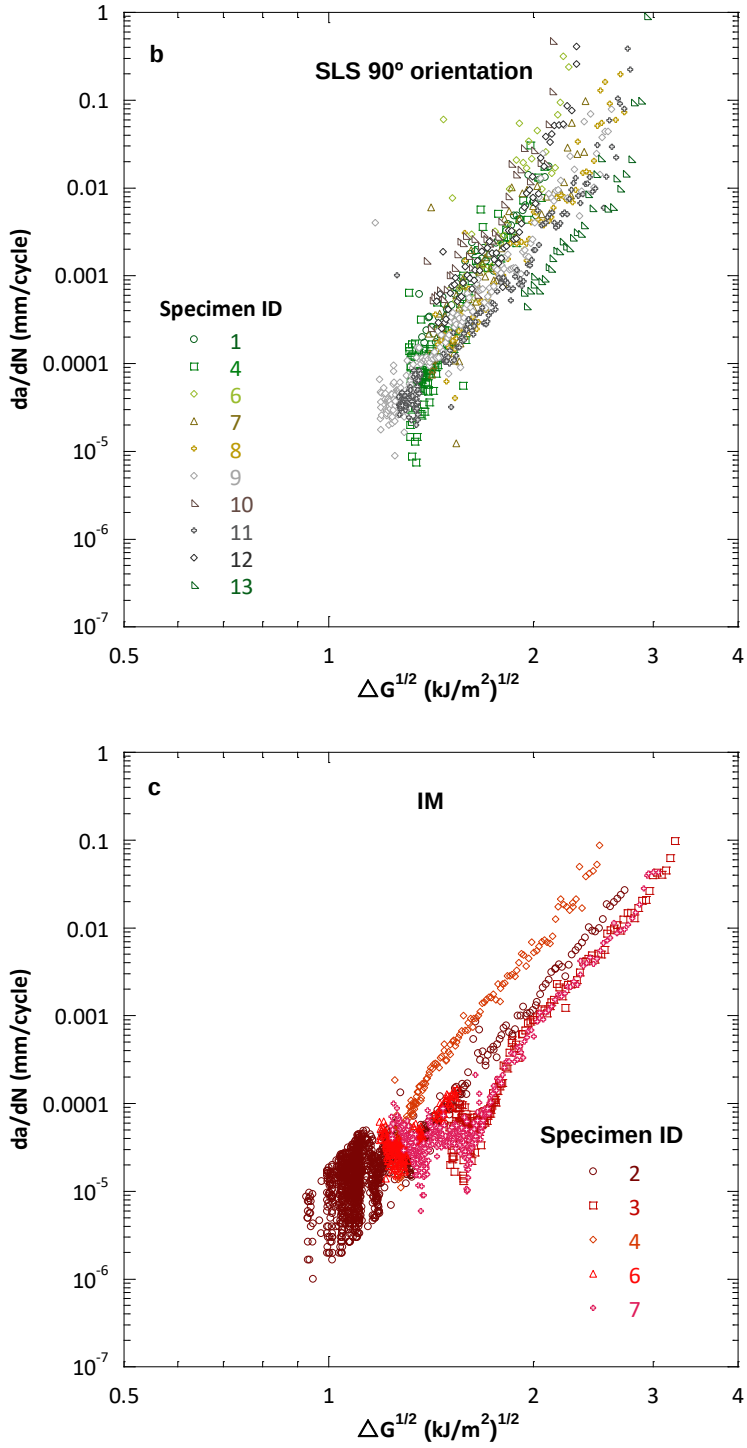

Figure 5-29. Fatigue crack growth curves of PA-12 manufactured by SLS at (a) 0° orientation and (b) at 90°orientation and (c) by IM.

The figures show the common scatter due to extrinsic factors like the experimental ones, such as material and geometry variability or variation in the testing conditions, and intrinsic factors as the probabilistic nature of the fatigue phenomenon itself [176]. For the characterization of region I and the determination of the control parameter threshold value, $(\Delta\sqrt{G})_{th}$, $\Delta\sqrt{G}$-decreasing tests were performed starting at a specific $\Delta\sqrt{G}$ level to guarantee some data overlap and consequently, to confirm the fatigue crack growth behaviour.

The experimental curves were fitted to equation *(2-2)* and the average values are shown in *Table 5-7*.

Table 5-7.Fatigue parameters of SLS PA-12 at 0° and 90° orientations and of IM PA-12. From $\Delta\sqrt{G}$-decreasing tests, threshold values of the control parameter $(\Delta\sqrt{G})_{th}$. From $\Delta\sqrt{G}$-increasing tests average values of A and n parameters from Paris law (eq. (2-2)), maximum value of the crack driving force before break, $(\sqrt{G})_{max,c}$, equivalent stress intensity factor of $(\sqrt{G})_{max,c}$, $\boldsymbol{K}_{max,c}$. Fracture toughness values, $\boldsymbol{K}_{IC}$, are also displayed (Figure 5-20).

	$\Delta\sqrt{G}$-decreasing	**$\Delta\sqrt{G}$-increasing**				**Fracture tests**
	$(\Delta\sqrt{G})_{th}$ (kJ/m²)$^{1/2}$	A	n	$(\sqrt{G})_{max,c}$ (kJ/m²)$^{1/2}$	$K_{max,c}$ (MPa·m$^{1/2}$)	K_{IC} (MPa·m$^{1/2}$)
SLS 0° orientation	1.3 ± 0.1	6·10^{-6}	9 ± 2	2.6 ± 0.2	3.7 ± 0.3	3.2 ± 0.2
SLS 90° orientation	1.1 ± 0.2	10·10^{-6}	10 ± 2	2.5 ± 0.3	3.6 ± 0.5	2.9 ± 0.2
IM	1.0 ± 0.2	5·10^{-6}	9.0 ± 0.5	3.0 ± 0.3	3.7 ± 0.4	3.1 ± 0.5

From the $\Delta\sqrt{G}$-increasing tests, the maximum values of the control parameter of the last cycle before catastrophic failure, $(\sqrt{G})_{max,c}$, their equivalent values in term of the stress intensity factor, $K_{max,c}$, and the fracture toughness, K_{IC}, determined from fracture tests and contained in *Figure 5-20*, have been also

included to facilitate the analysis. Furthermore, the threshold values of the crack driving force, $\left(\Delta\sqrt{G}\right)_{th}$, obtained from $\Delta\sqrt{G}$-decreasing tests are also displayed.

Moreover, to shed more light to the study, *Figure 5-30* gathers in one single diagram the fatigue crack propagation behaviour of *SLS* PA-12 at 0° and at 90° orientations and of *IM* PA-12. The characteristic dispersion of each material and condition has been represented with an envelope.

All this information reveals that the fatigue crack growth behaviour is very similar independently of orientation and manufacturing technique but there are some point differences worth mentioning. The effect of the load direction with regard to the layered structure of *SLS* PA-12 on the fatigue crack growth behaviour is obvious as *SLS* PA-12 at 0° orientation shows higher threshold values and smaller values of the exponent of the Paris law than those of *SLS* PA-12 at 90° orientation. Therefore, it can be concluded that the fatigue crack growth resistance is worse when the load is applied along the building direction, that is, at 90° orientation.

When analysing the influence of the manufacturing process, the threshold values of *IM* PA-12 are the smallest, but the steepness of the Paris law curve is similar to that of *SLS* PA-12 at 0° orientation. So, the fatigue crack growth behaviour of *IM* PA-12 is in between those of *SLS* PA-12 at 0° and at 90° orientations.

The region III of the fatigue crack growth life is characterized by the maximum value of the control parameter of the last cycle before rupture. Independently

of the material or testing condition, the values were around 10% higher than the fracture toughness measured via standard fracture tests.

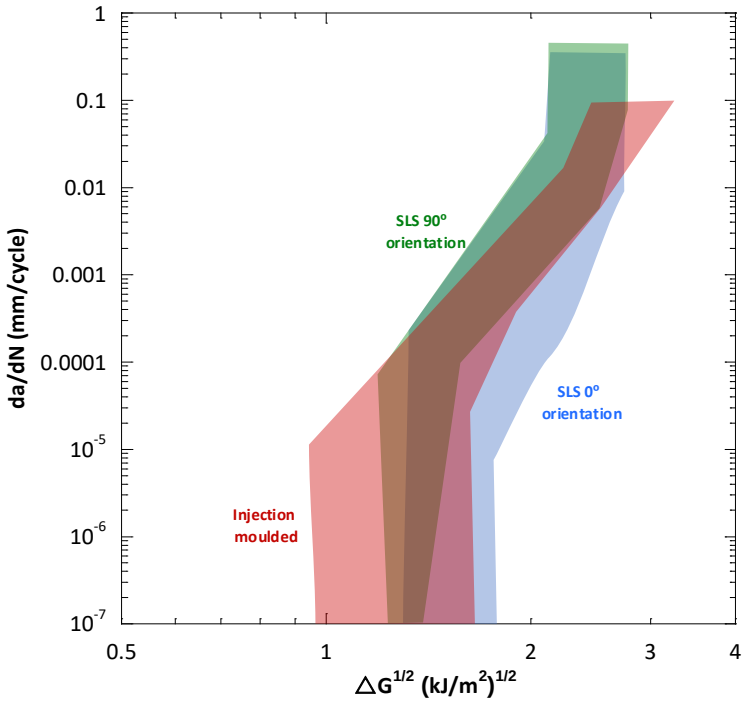

Figure 5-30. Fatigue crack growth behaviour comparison for PA-12 manufactured by SLS at 0° orientation (blue) and at 90°orientation (green) and by IM (red).

There is scarce literature regarding this topic in the literature. In principle, the exponents of the Paris law of *SLS* PA-12 are smaller than those obtained by Salazar et al. [39]. Nevertheless, it is worth mentioning that these authors employed ΔK as the crack driving force and the starting PA-12 powder and manufacturing machine were different to those used for the processing of the materials under study. Although Blattmeier et al. [124] analysed the influence of the load direction with respect to the layered structure in *SLS* PA-12, they observed no differences in the fatigue crack propagation of specimens tested at 0° and 90° orientations. And their curves are difficult to compare to those in the present work because firstly, the control parameter is ΔK and there are

no fitting values to a Paris-law equation and secondly, those curves were not obtained under constant load amplitude tests. Finally, the only works focused on the fatigue crack propagation of *IM* PA-12 are those of Blattmeier et al. [124] and Boukhili et al. [79]. The former obtained a fatigue crack growth behaviour of *IM* PA-12 clearly worse than that of *SLS* PA-12 and the latter realized that ΔK is not a valid crack driving force and also did not include the fitting values of the Paris-law equation.

5.7.1. Fractographic analysis from fatigue crack growth tests

The panoramic view of the fracture surfaces of *SLS* PA-12 at 0° and 90° orientations and of *IM* PA-12 are displayed in *Figure 5-31.a, Figure* 5-31.*b* and *Figure* 5-31.*c*, respectively. The arrow indicates the crack growth direction.

Firstly, the most characteristic feature of the fracture surfaces of S*LS* PA-12 is the high number of pores evenly distributed over the entire surface (*Figure 5-31.a, Figure* 5-31.*b)*. According to Caulfield et al. [33], these pores are the result of the lack of powder particles melting during sintering, producing a poor fusion in the surrounding area. Another important feature is the discernible horizontal lines with an equidistant separation of 200 µm observed in the low magnification analysis of the fracture surfaces of *SLS* PA-12 at 0° orientation (*Figure 5-31.a).* This distance matches with the manufacturing layer thickness (*Table 4.2*) so, the sintering among layers was defective as the fusion and sintering of one layer with the one underneath was not complete. Some authors have associated these lines with a low energy density supplied during the manufacturing process [33], [37].

Secondly, when comparing the 0° and 90° orientations, the fracture surfaces obtained at 90° orientation (*Figure 5-31.b*) was much smoother than that at 0°

orientation (*Figure 5-31.a*). The crack tends to propagate along one single layer but when a coalescence of pores or defects occurs, this can lead to the jump of the crack to adjacent layers. This could explain the worse fatigue crack propagation at 90° orientation.

Thirdly, the panoramic view of the fracture surfaces of the *IM* PA-12 samples is completely smooth and plain, a striking contrast when compared to the morphology of *SLS* PA-12 (*Figure 5-31.c).*

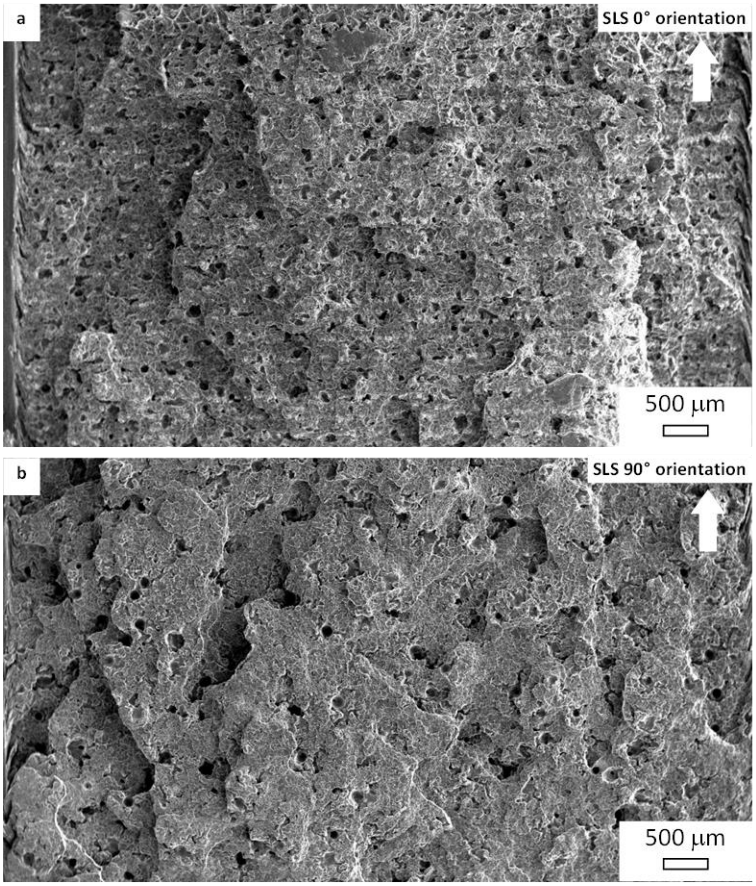

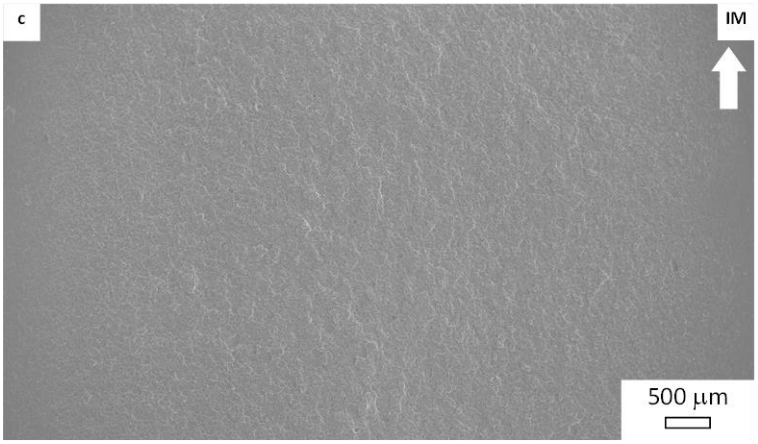

Figure 5-31. Panoramic view of the fracture surfaces obtained from fatigue crack growth tests of PA-12 manufactured by (a) SLS at 0°orientation, (b) SLS at 90° orientation (b) and (c) IM. The arrow points out the crack growth direction.

In order to identify the deformation and fracture mechanisms, *Figure 5-32.a* , *Figure 5-32.b* and *Figure 5-32.c* show detailed fracture surfaces of *SLS* PA-12 at 0° and 90° orientations and of *IM* PA-12, respectively. Independently of the manufacturing technique or the orientation, the mechanism of deformation and failure is the formation, growth and coalescence of crazes, followed by a fibrillation of the amorphous phase till final rupture.

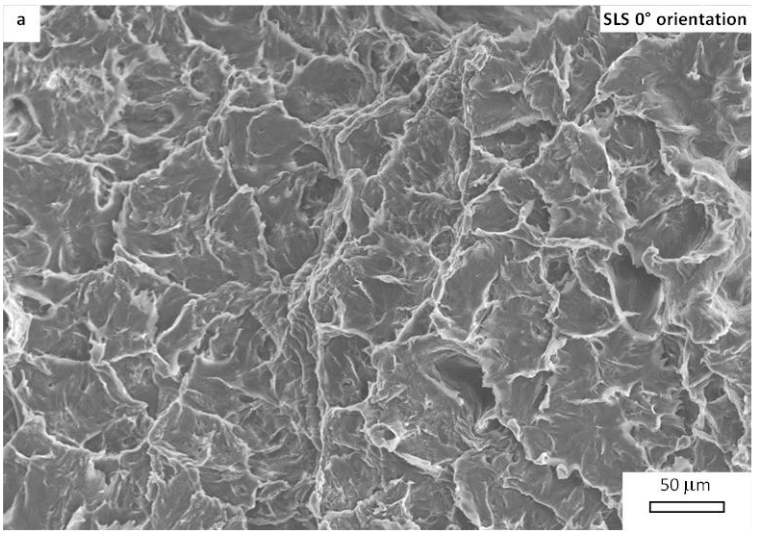

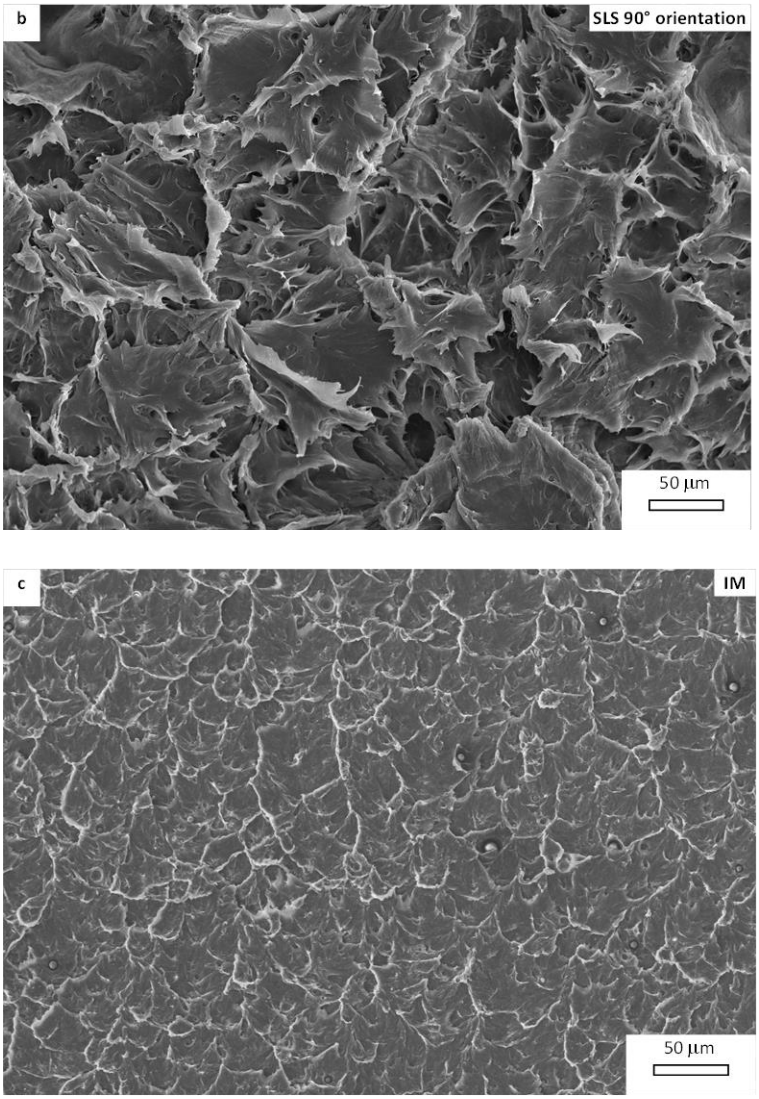

Figure 5-32. Detail of the fracture surfaces obtained from fatigue crack growth tests of PA-12 manufactured by (a) SLS at 0°orientation, by (b) SLS at 90° orientation (b) and (c) by IM.

This type of damage progression leaves as marks the patchwork pattern displayed in *Figure 5-33*, being the only difference, the size of the craters and the more or less plastic deformation of the amorphous filaments surrounding them. In general, the stretched amorphous filaments are the most prominent in the *SLS* PA-12 at 0° orientation (*Figure 5-33.a*), less significant in the *SLS* PA-

12 at 90° orientation (*Figure 5-33.b*) and not so remarkable in *IM* PA12 (*Figure 5-33.c*).

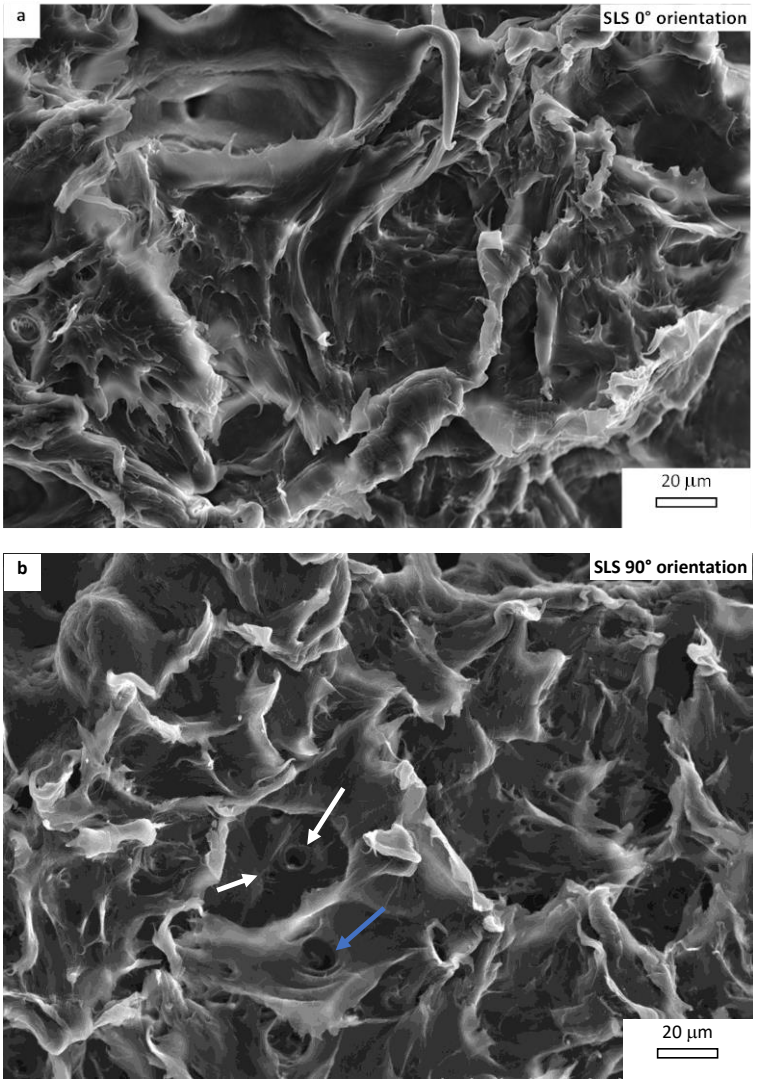

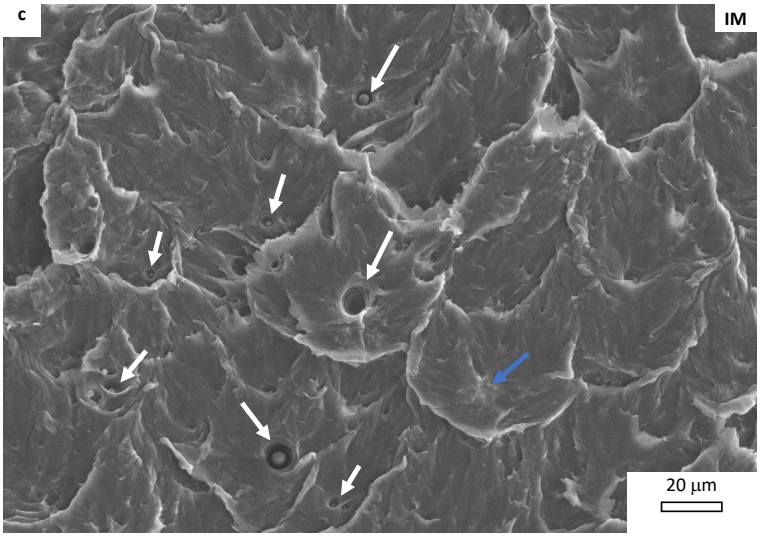

Figure 5-33. Detail of the patchwork structure due to craze formation of PA-12 manufactured by SLS at 0° orientation (a) and at 90° orientation (b) and by IM (c). The nucleation sites of damage initiation are pointed out by arrows. The white arrows point to unmolten particles or the voids left behind by them and the blue arrows point to spherulitic nuclei.

It is in these deformed amorphous filaments where fatigue striations were observed (*Figure 5-34*), being less numerous in the *IM* PA-12 (*Figure 5-34.c*) compared with SLS ones (*Figure 5-34.a* and *Figure 5-34.b*).

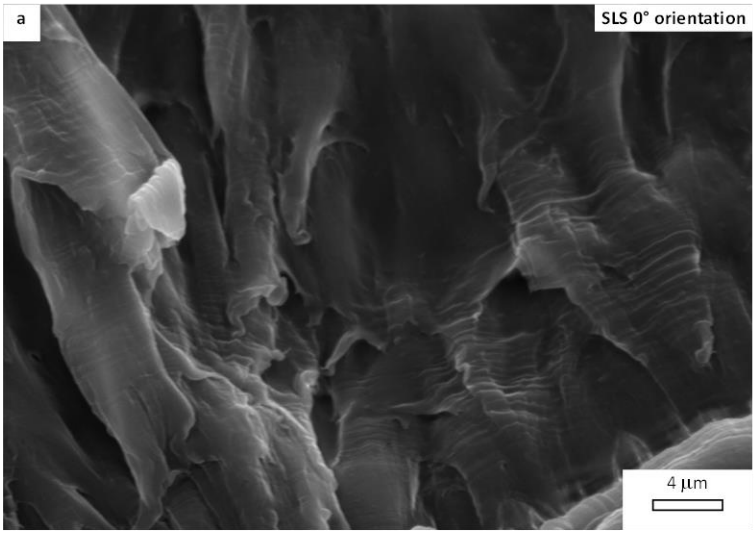

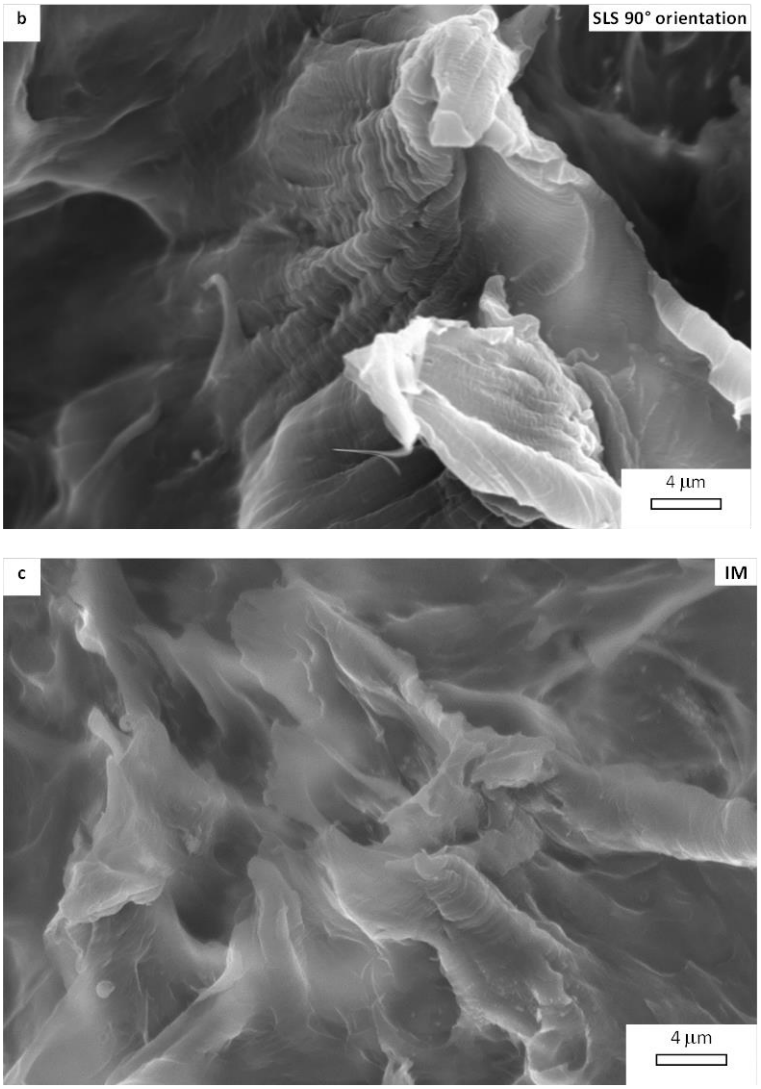

Figure 5-34. Fatigue river markings in amorphous filaments left behind the crack growth that surround the dimples generated after craze nucleation, growth and coalescence of (a) SLS PA-12 at 0° orientation, (b) SLS PA-12 at 90° orientation and of (c) IM PA-12.

Therefore, the rough fracture surface (Figure 5-31.a, and Figure 5-32.a) together with the high deformed amorphous filaments in *SLS* PA-12 at 0° orientation (*Figure 5-34.a*) seems to be the reason of the best fatigue crack growth behaviour.

A more in-depth analysis of the nucleation and progression of the mechanism of failure during fatigue could be performed thanks to the fractographic analysis at high magnification shown in *Figure 5-35.*

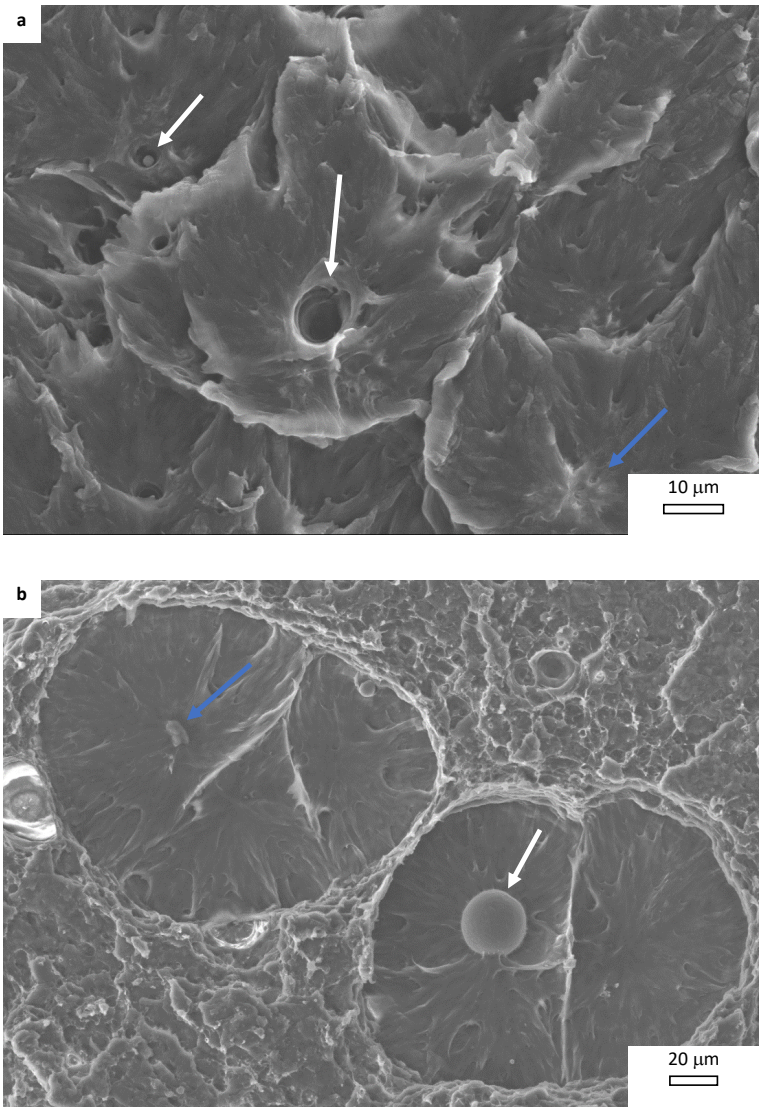

Figure 5-35. Detail of the micromechanism of failure, where the craters left behind the fatigue crack path are originally generated by unmolten particles (pointed out by white arrows) or by spherulitic nuclei in form of ill-defined discs (a) or irregular rectangles (b), that act as damage precursors (pointed out by blue arrows).

In this patchy surface, pores and in most cases, some unmolten particles at the centre of the craters are observed and shown with white arrows pointing at the particles in *Figure 5-33.b* and *Figure* 5-33.*c* for *SLS* at 90° orientation and for *IM* PA-12, respectively, and in *Figure 5-35*. These defects act as nucleation sites during the crazes formation being not the only responsible of the failure initiation. The crystalline structure plays an important role in the initiation damage during cycling loading as pointed out by several authors [162], [177], [178].

During fatigue, the high deformation occurring at the crack tip is the origin of void nucleation between the crystalline lamellae within the spherulite, oriented perpendicularly or at angle of approximately 45° to the applied load direction [177]. This leads to an intra-spherulitic or trans-spherulitic failure in the equatorial plane, exposing in some occasions the nucleus of the spherulite, which has the appearance of an irregular rectangle (pointed out by a blue in *Figure 5-33.b and Figure 5-35.b*) or an ill-defined disc (pointed out by a blue arrow in *IM* PA-12 in *Figure 5-33.c and in Figure 5-35.a*).

Some authors have linked the dimensions of the patchwork patterns with the spherulite sizes. In this case, the crater size was around 50 µm for *SLS* PA-12 and 20-30 µm for *IM* PA-12 which is coincident with the spherulitic dimensions collected in *Table 5-3*. The bigger discrepancy was in *IM* PA-12. However, the fractographic analysis has shown that in *IM* PA-12, the damage was related with the spherulitic structure in a way that the micromechanism of failure is linked not only to individual spherulites but also to spherulite colonies when the former are extremely fine.

5.8 FATIGUE LIFE ANALYSIS

The results of the fatigue life tests carried out according to the ASTM D7791 standard recommendations are presented in the *Figure 5-36*. The tensile strength represented as the value at one cycle was also included, as well as the tests which reached 10^6 cycles without failure (run-outs). A first look at the graph evidences not big differences between either distinct orientations or manufacturing processes. Nevertheless, some dissimilarities are important to highlight.

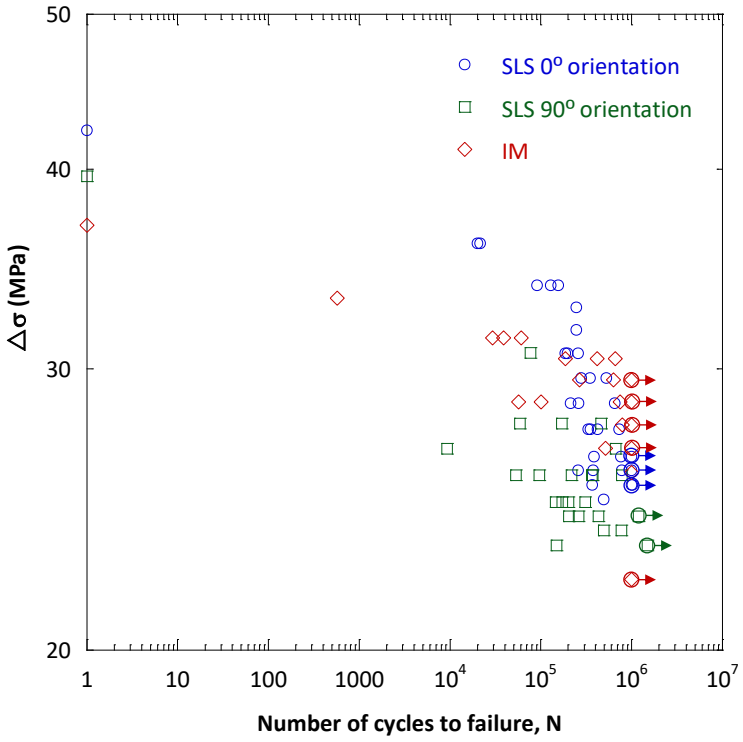

Figure 5-36. Lifetime fatigue curves of IM PA-12 and SLS PA-12 0 °and 90 °orientations. ○→ symbol represents run-outs, that is, tests which reached 10^6 cycles without break.

SLS PA-12 at 0° orientation exhibited better fatigue life resistance than at 90° orientation despite the similarity in the porosity percentage (*Table 5-1*) and in the surface roughness values (*Table 5-2*). The weak interlayer strength seems

to be behind this behaviour, as the defective sintering among layers as well as its physical discontinuity has been observed in the fractographic analysis (*Figure 5-31.a*).

Attending to the manufacturing process, *IM* PA-12 presented a mixed behaviour, that is, showed a better fatigue resistance than *SLS* PA-12 at both orientations near 10^6 cycles but a lower fatigue life resistance when the number of cycles to break was around 10^5. At those number of cycles, the behaviour of *SLS* PA-12 at 0° orientation is above that of *IM* PA-12.

In order to fit these results to the Basquin's equation, the average values of the number of cycles to failure for each load level were considered and represented in *Figure 5-37*. Attending to the values of the R^2 coefficient resulting from the fitting of the experimental values to the Basquin's law (*eq. (*4-28)), the scatter for all materials and conditions was in general very high, especially for *SLS* PA-12 at 90° orientation.

Table 5-8 gathers the Basquin coefficients of *SLS* PA-12 at 0° and 90° orientations and of *IM* PA-12. While the exponents of m_B of *SLS* at both orientations were similar, there is a big difference with that of the *IM* PA-12 which was one half.

Table 5-8. Basquin constants from S-N curves of IM PA-12 and SLS PA-12 at 0° and at 90° orientations.

	B_B	m_B
SLS 0° orientation	111.1	-0.11
SLS 90° orientation	83.1	-0.09
IM	54.4	-0.05

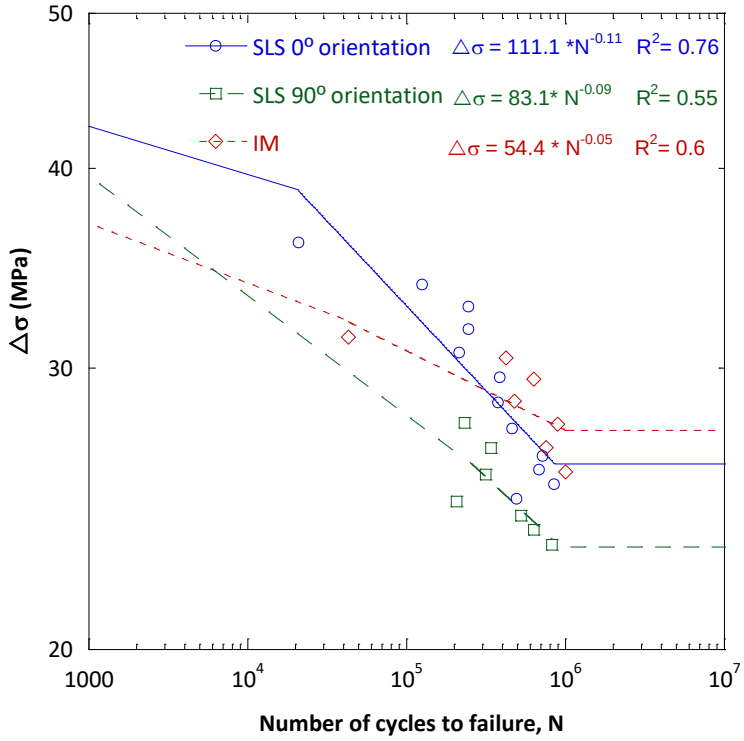

Figure 5-37. Lifetime fatigue curves IM PA-12 and SLS PA-12 at 0 °and at 90 °orientations representing the average values of each load level. The fitting of the experimental results to the Basquin type equation $\Delta\sigma = B_B N^{m_B}$ is also displayed.

For the determination of the fatigue limit at 10^6 cycles, *Figure 5-38.a*, *Figure* 5-38.*b* and *Figure* 5-38.*c* show the up-and-down fatigue test results of *SLS* PA-12 at 0° orientation, *SLS* PA-12 at 90° orientation and *IM* PA-12, respectively. These graphs represent the run-out tests with a green circle and the failure tests with a red cross. In order to obtain more accurate results, in case of *SLS* PA-12 at 0° orientation, after 6 tests, the initial stress step between run-out and failure was reduced to one half of the initial value, followed by a second reduction of a 2.5 % of the initial value, analysing a total of 5 stress amplitudes. For *SLS* PA-12 at 90° orientation, only a first reduction of the step from 2.5%σ_T to 1.25%σ_T was implemented, with a total of 4 stress amplitudes. In case of *IM* PA-12, two step reductions were carried out, beginning with the first one of

11.5%σ_T and followed by a second one of 2.5%σ_T. The total number of stress amplitudes examined were 6.

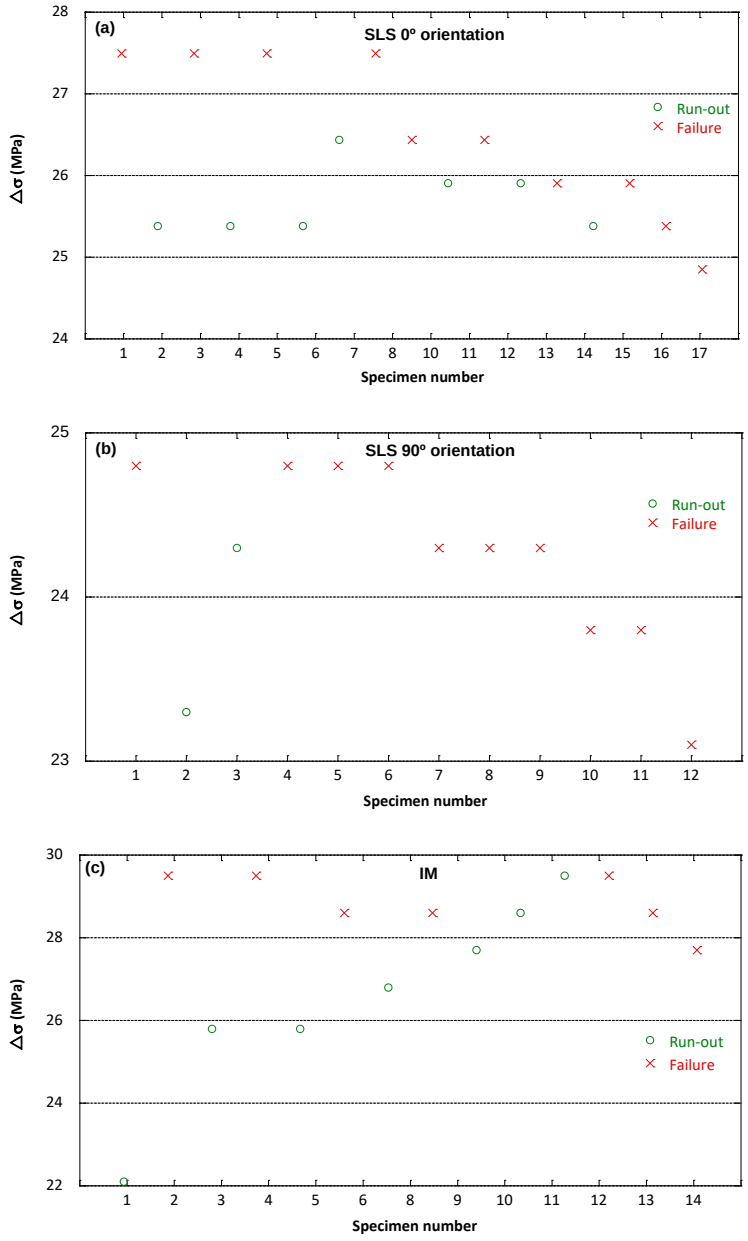

Figure 5-38. Up-and-down fatigue tests for the estimation of the fatigue limit at 10^6 cycles: (a) SLS PA-12 at 0° orientation, (b) SLS PA-12 at 90°orientation and (c) IM PA-12. The representations include run-out tests ○ and failure ones ×.

Table 5-9 displays the fatigue lifetime results used in the estimation of the fatigue limit at 10^6 cycles for both orientations of *SLS* PA-12 and of *IM* PA-12. It shows the number of failure tests, the number of "Run-outs" tests for each stress level, $\Delta\sigma_i$, and the fatigue limit at 10^6 cycles, $\Delta\sigma_{fl}$, resulting from the application of the maximum likelihood method assuming a normal distribution, as described in the previous chapter.

Table 5-9. Results of the fatigue lifetime test for the determination of the fatigue limit at 10^6 cycles, $\Delta\sigma_{fl}$, of SLS PA-12 at 0° and 90° orientations and of IM PA-12, including the stress amplitude, $\Delta\sigma_i$, number of failure tests, f_i, and of run-outs, r_i.

Manufacturing orientation	$\Delta\sigma_i$ (MPa)	Number of failure tests, f_i	Number of Run-out tests, r_i	$\Delta\sigma_{fl}$ (MPa)
0°	24.8	1	0	26 ± 1
	25.4	1	3	
	25.9	3	2	
	26.5	2	1	
	27.5	4	0	
		$\sum f = 11$	$\sum r = 6$	
		n = 17		
90°	23.3	1	1	23 ± 1
	23.8	2	0	
	24.3	3	1	
	24.8	4	0	
		$\sum f = 10$	$\sum r = 2$	
		n = 12		
IM	22.1	0	1	28 ± 1
	25.8	0	2	
	26.8	0	1	
	27.7	1	1	
	28.6	3	1	
	29.5	3	1	
IM		$\sum f = 7$	$\sum r = 7$	
		n = 14		

SLS PA-12 at 0° orientation had a statistical fatigue limit at 10^6 cycles 13% higher than the one at 90° orientation. However, *IM* PA-12 had the highest fatigue limit, being 8% higher than the one of *SLS* PA-12 at 0° orientation.

5.8.1. Fractographic analysis of fatigue life tests

A panoramic view of the fracture surfaces of *SLS* PA-12 at 0° and 90° orientations and of *IM* PA-12 are shown in *Figure 5-39.a, Figure 5-39.b* and *Figure 5-39.c*, respectively. The white arrow indicates the crack growth direction on each specimen and, in all cases, the cracks propagated from the left side of the images to the right. It is obvious the influence of the manufacturing technique on the fractographic analysis of the broken specimens tested for the stress life fatigue curves characterization. While the fracture surfaces of *SLS* PA-12 maintained the initial cross-sectional dimensions, all the *IM* PA-12 fracture surfaces undergone a strong reduction of the initial cross section area despite the testing conditions were under High Cycle regime.

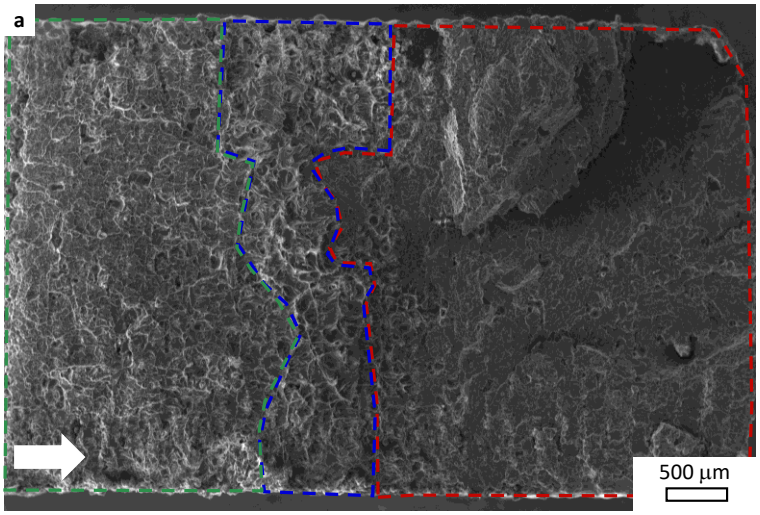

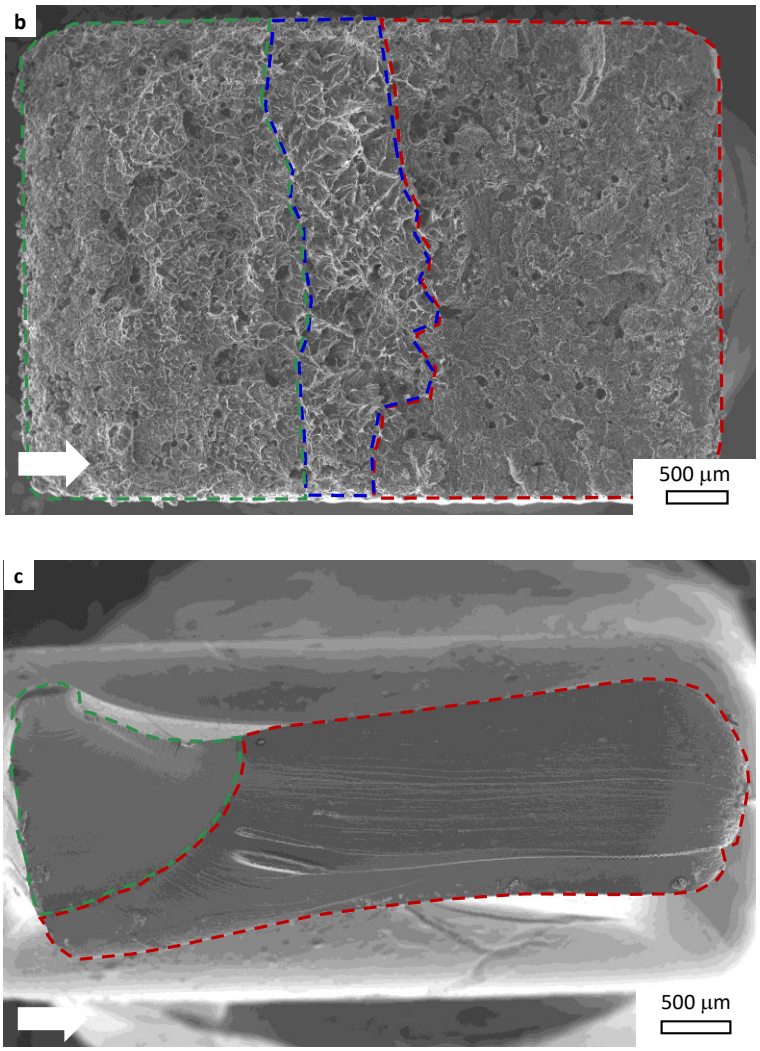

Figure 5-39. Panoramic views of (a) SLS PA-12 at 0° orientation (a) SLS PA-12 at 90° orientation and (c) IM PA-12, identifying different: Region I or subcritical crack growth zone outlined with a dashed green line, Region II or transition region delineated with a dotted blue line and region III or unstable crack growth region surrounded with a dotted red line.

Moreover, while in all *SLS* PA-12 fracture surfaces three different areas were distinguishable and outlined by three different colours over the surfaces, in *IM* PA-12, only two zones were discernible. For all the cases, the zone delimited by the dashed green line is the subcritical crack growth area, which is followed

by a transition region outlined in dashed blue line (only observed in *SLS* PA-12), and finally, the unstable crack growth region delineated in dashed red line.

For *SLS* PA-12, the subcritical area was characterized by a patchy irregular surface, unequivocal morphological sign of nucleation, growth and coalescence of crazes in both the early stages of formation of the macroscopic crack and subsequent propagation. The crater size of the marks left by this damage advancement was of around 50 µm, which matches with the spherulitic size determined in section *5.3* (*Figure 5-40*). This fact revealed a hampered crack growth due to the presence of spherulites in a trans-spherulitic growth mode. Therefore, the crack was nucleated at some point of the surface, favoured by the high roughness (*Table 5-2*), and once generated progressed through the spherulites and in many cases, going through their equatorial plane. This mechanism of failure was also observed in the fracture surfaces of *SLS* PA-12 obtained from tensile tests (*section 5.5.1*), from fracture toughness tests (*section 5.6.1*) and from fatigue crack growth tests (*section 5.7*).

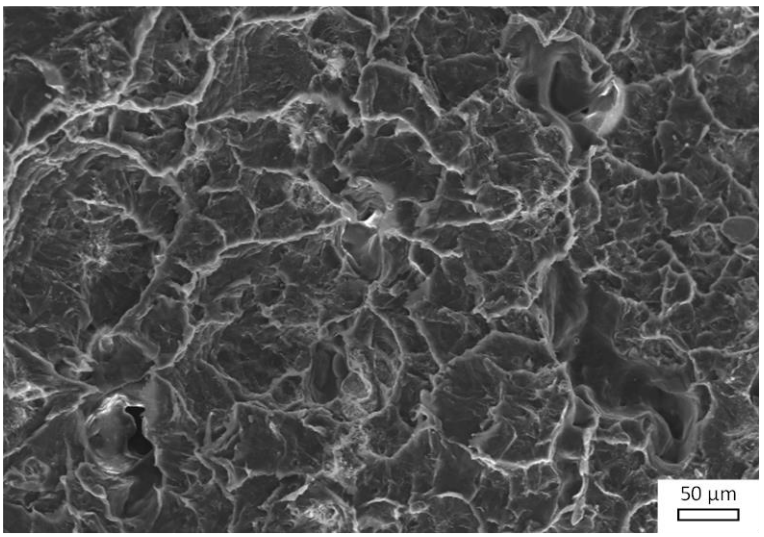

Figure 5-40. Morphology of the subcritical crack growth zone of SLS PA-12.

The only difference between 0° and 90° orientations in *SLS* PA-12 was that this area seemed to be rougher in the samples tested at 0° orientation that in those tested at 90° orientation.

In case of *IM* PA-12, the crack also nucleated at some point at the surface, belonging to the skin layer due to the presence of small sink marks (*Figure 5-39.c*). The morphology of the subcritical crack growth area is completely different to that observed in *SLS* PA-12, characterized by fatigue striations bowed out in the direction of the crack propagation (*Figure 5-41*). The fatigue striations spacing became larger as moving away from the surface defect responsible of the crack nucleation.

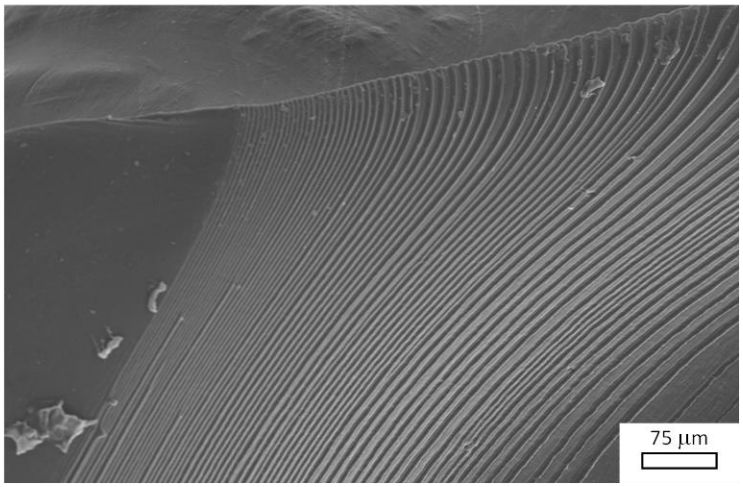

Figure 5-41. Morphology of the subcritical crack growth zone of IM PA-12.

In *SLS* PA-12, following the subcritical crack growth zone, a transition region, was observed and outlined in dashed blue line in *Figure 5-39.a* and *Figure 5-39.b*, and shown in detail in *Figure 5-42*. This region was characterised by a high ductile tearing of amorphous filaments around dimples, which in some cases could be hidden by the plastic deformation. The amorphous filaments were aligned along the crack propagation direction and fatigue striations were

only observed on them (*Figure 5-43)*. No differences were appreciated between *SLS* PA-12 at 0° and at 90° orientations. Moreover, the transition region was not observed in none of the fracture surfaces of *IM* PA-12.

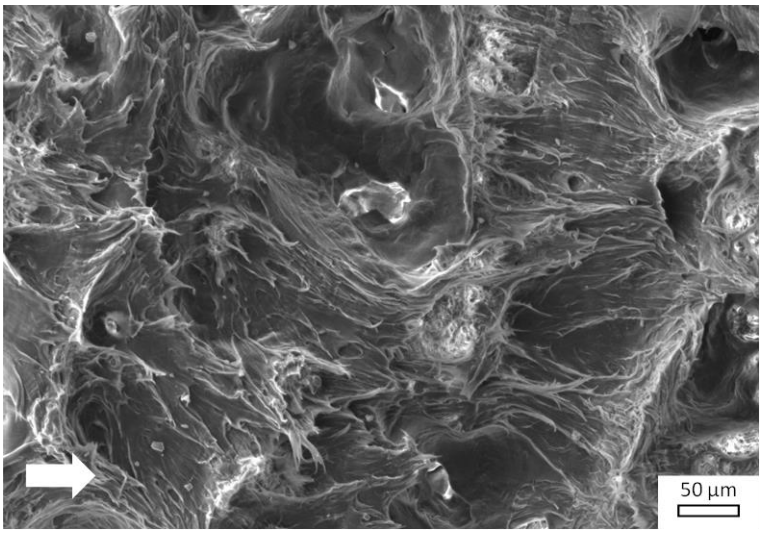

Figure 5-42. Transition region: the filaments of amorphous PA-12 suffered high elongation along crack propagation direction.

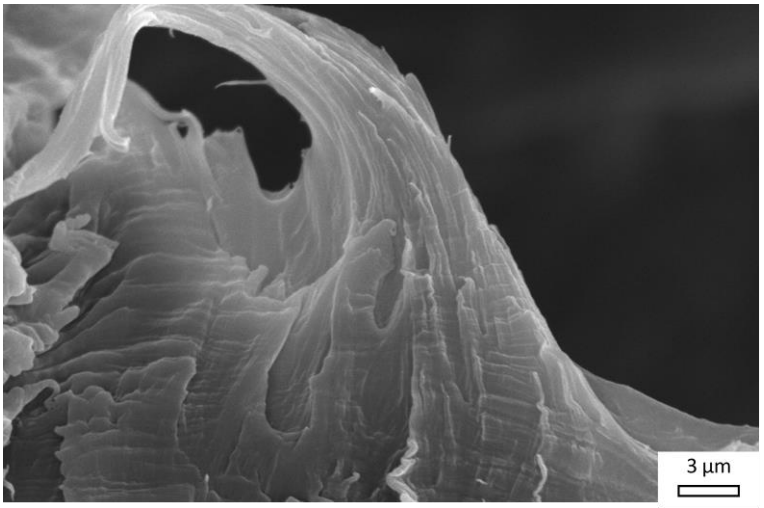

Figure 5-43. Fatigue marks visible in the high elongated filaments in the transition region.

In *SLS* PA-12, following the transition region, the unstable crack growth region, outlined in dotted red line in *Figure 5-39.a* and *Figure 5-39.b* was found. The

border between these two regions was continuous (*Figure 5-44.a*) and the morphology was plain, with an irregular pattern and with no trace of distinguishable elongation of amorphous material (*Figure 5-44.b*). No differences in this zone were discernible between both orientations in *SLS* PA-12.

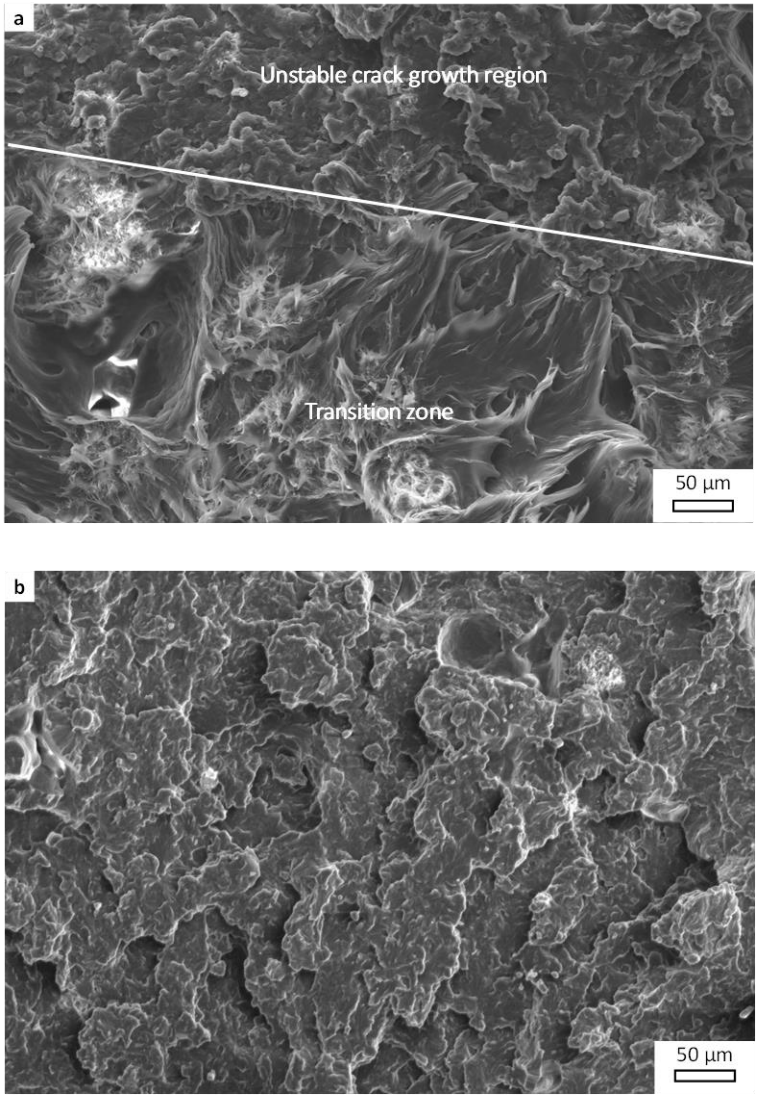

Figure 5-44. (a) Border between the transition zone and the unstable crack growth region, and (b) morphology of the unstable crack growth area of SLS PA-12.

Finally, *Figure 5-45* shows a detail of the unstable crack growth zone of *IM* PA-12 outlined in dotted red line in *Figure 5-39.c*. The surface was smooth and plain with no characteristic feature except for some very fine river markings along the crack growth direction.

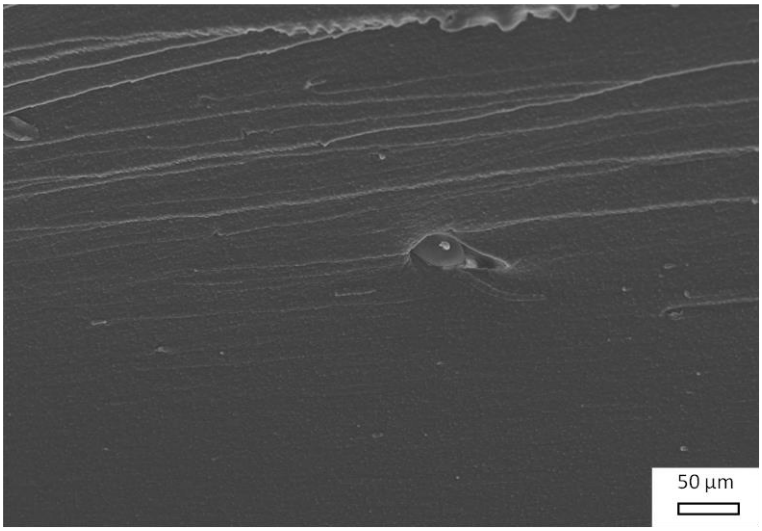

Figure 5-45. Morphology of the unstable crack growth region of IM PA-12.

5.8.2. Application of the Fracture Mechanics approach to the fatigue life tests

The fractographic analysis of the broken specimens revealed a scheme of the damage progression till catastrophic failure occurring during the fatigue life tests. The nucleation of the crack occurred at some point at the surface, as a consequence of the high roughness in *SLS* PA-12 specimens or of the amorphous skin layer in *IM* PA-12 samples. The crack propagation occurred till reaching a critical value, coincident with the extension of the subcritical crack growth zone, a. At that moment, brittle failure occurred at the remnant ligament, giving rise a plastic deformation zone at the crack tip (transition region) followed by an undamaged polyamide (unstable crack growth zone) in

SLS PA-12. However, in *IM* PA-12, only unstable crack growth area was observable but with evident plastic deformation along the gage length of the sample due to a pronounced reduction of the initial cross-sectional area. Just because the non-negligible plastic deformation along the gage length in *IM* PA-12, damage modelling using the Fracture Mechanics approach was only applied to *SLS* PA-12 at 0° and 90° orientations.

*Table 5-10. Estimation of the fracture toughness of SLS PA-12 at 0°orientation from fatigue life tests damage modelling including the stress ration, $\frac{\sigma_{max}}{\sigma_T}$, the length of subcritical crack growth, a, the estimated value of the energy at growth initiation, J_C. *The average value in bold was calculated without the results at stress levels of 0.8 and 0.85.*

$\frac{\sigma_{max}}{\sigma_T}$	a (mm)	J_C (kJ/m^2)
0.58	2.41	6.65
0.60	1.87	8.08
0.61	2.0 ± 0.2	6.7 ± 0.4
0.63	1.66	6.11
0.65	1.8 ± 0.1	6.9 ± 0.9
0.68	1.7 ± 0.1	6.8 ± 0.1
0.7	1.7 ± 0.1	7.3 ± 0.6
0.73	1.55	7.24
0.75	1.81	8.09
0.78	1.55	9.19
0.8	1.4 ± 0.1	10.2 ± 0.2
0.85	0.9 ± 0.1	12 ± 1
		7.1 ± 0.8*

From the sketch of the different zones delineated in *Figure 5-39.a* and *Figure 5-39.b*, the fatigue life specimens with the subcritical crack growth area could be fitted in with SENT configuration at the instant of failure. So, the results obtained from the application of the Fracture Mechanics approach using data

from the last cycle are shown in *Table 5-10* and *Table 5-11* for *SLS* PA-12 at 0° and 90° orientations, respectively.

Table 5-11. Estimation of the fracture toughness of SLS PA-12 at 90°orientation from fatigue life tests damage modelling including the stress ration, $\frac{\sigma_{max}}{\sigma_T}$, the length of subcritical crack growth, a, the estimated value of the energy at growth initiation, J_C.

$\frac{\sigma_{max}}{\sigma_T}$	a (mm)	J_C (kJ/m^2)
0.60	2.0	6.47
0.65	1.9 ± 0.2	5.5 ± 0.4
0.7	1.82	6.79
0.78	1.56	7.53
		6.0 ± 0.8

From the analysis of the results, several points are remarkable and worth discussing. Firstly, a common trend can be observed for both orientations, the length of the subcritical crack growth is lower as the applied stress level increases. Secondly, the estimated energy at crack growth initiation values are in accordance with those achieved in standardized fracture tests shown in *section 5.6* for both orientations. Nevertheless, some deviations were obtained in *SLS* PA-12 at 0° orientation for the high stress levels of 0.8 and 0.85. For these testing conditions, the estimated values of J_c were extremely high and were not included in the computation of the average value displayed in bold in *Table 5-10*. To ascertain the possible reason of these overestimated values of J_C at those stress levels, the hysteresis loops of the last cycle before failure were examined. *Figure 5-46* shows the hysteresis loops of the last cycle before failure of the fatigue life tests carried out at stress ratios of 0.7 and 0.85 of *SLS* PA-12 at 0° orientation. The main difference is that, while for the stress ratio of 0.7, the loading and unloading parts of the cyclic load-displacement record overlap, for the stress ratio of 0.85 an area within the loop is noticeable. This

area represents dissipative energy per unit of volume due to viscoelasticity and/or plasticity, which can be the reason of the overestimation of the fracture parameters.

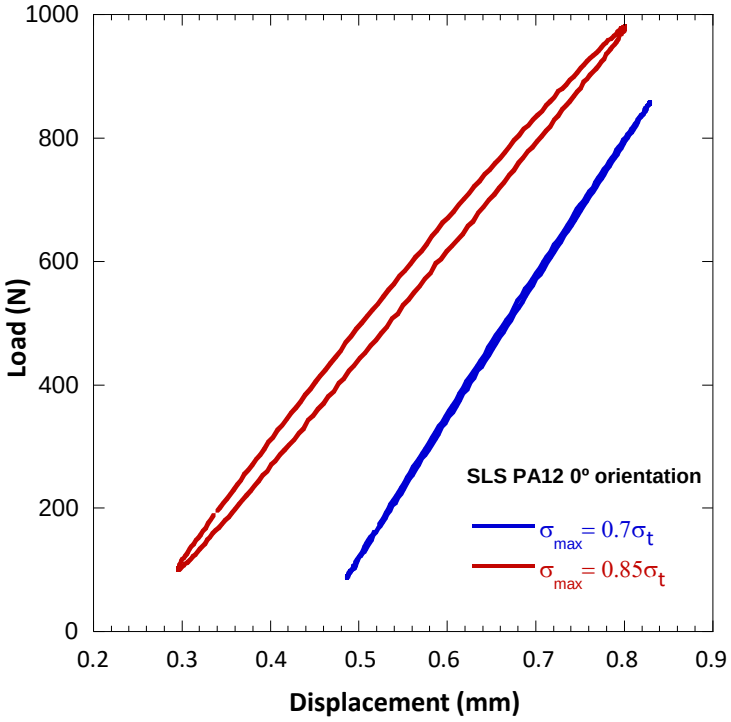

Figure 5-46. Hysteresis loops obtained from the cyclic load-displacement records of the last cycle before rupture of the tests at stress ratios of 0.7 and 0.85 performed in PA-12 at 0° orientation.

Another method to check the validity of the results is to determine the crack length from the unloading part of the load-displacement record of the last cycle using the following expression for SENT configuration [179]:

$$\frac{a}{W} = 2.072 - 16.411U + 29.6U^2 - 211.67U^3 + 236.857U^4 + 27.371U^5 - 179.74U^6 - 86.28U^7 + 171.764U^8 \quad (5\text{-}1)$$

with U the normalized compliance obtained from the unloading part of the cyclic load-displacement record using equation (4-24). The calculations yield results which differed from the measured lengths of the subcritical crack growth zone in *Table 5-10* utmost 20% for stress level lower than 0.8 and more than 90% for stress level higher than 0.80.

Chapter 6.

Discussion

In this chapter, the experimental results obtained in this thesis have been analysed and discussed with a global perspective. Three aspects of the fracture and fatigue behaviour have been considered: static residual strength, infinite fatigue life and finite fatigue life.

6.1 RESIDUAL STRENGTH DIAGRAMS

Kitagawa-Takahashi diagram can be extended to the static failure occurring at one cycle. In this failure diagram for static loading, the limit in the *MSC* regime is taken as the tensile strength, σ_t, and the prediction for *LC* regime is calculated with the fracture toughness, K_{IC}, being the allowable nominal stress given by:

$$\sigma = \frac{K_{IC}}{\sqrt{\pi a}} \qquad (6\text{-}1)$$

El Haddad model is also suitable for this static case, introducing the characteristic length, l_0^S, for the static response:

$$\sigma_{Hd} = \frac{K_{IC}}{\sqrt{\pi(a + l_0^S)}} \qquad (6\text{-}2)$$

where:

$$l_0^S = \frac{1}{\pi}\left(\frac{K_{IC}}{\sigma_t}\right)^2 \qquad (6\text{-}3)$$

Figure 6-1 shows the residual strength curves, in continuous line, and the modified El Haddad model, in dashed line, of *SLS* PA-12 at 0° and at 90° orientations and of *IM* PA-12.

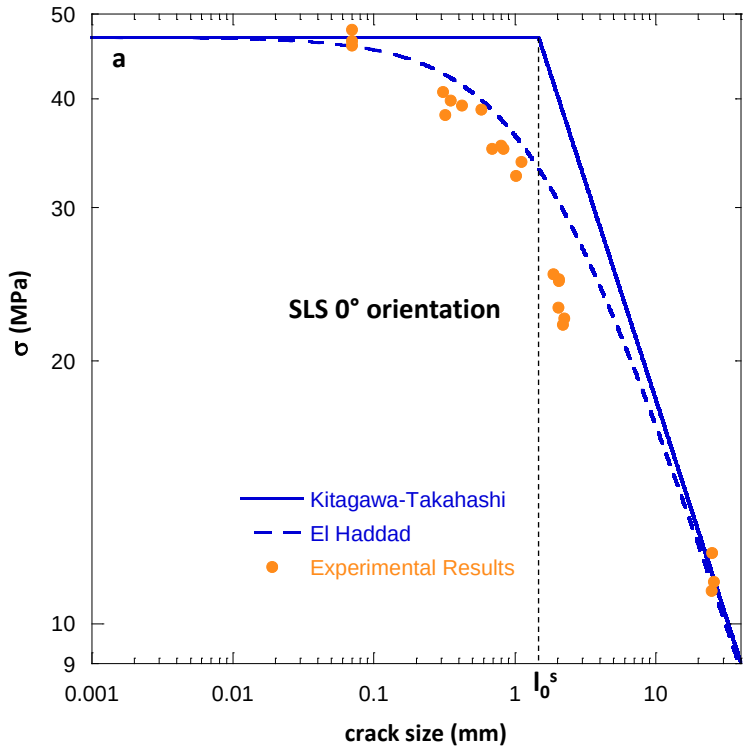
a
SLS 0° orientation
σ (MPa)
50
40
30
20
10
9
0.001
0.01
0.1
1
10
l_0^s
crack size (mm)
Kitagawa-Takahashi
El Haddad
Experimental Results

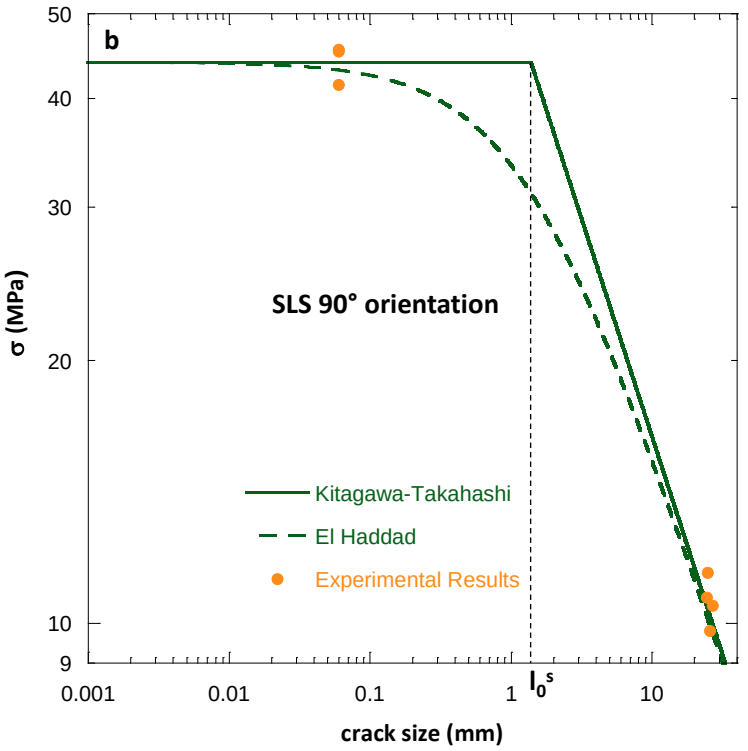
b
SLS 90° orientation
σ (MPa)
50
40
30
20
10
9
0.001
0.01
0.1
1
10
l_0^s
crack size (mm)
Kitagawa-Takahashi
El Haddad
Experimental Results

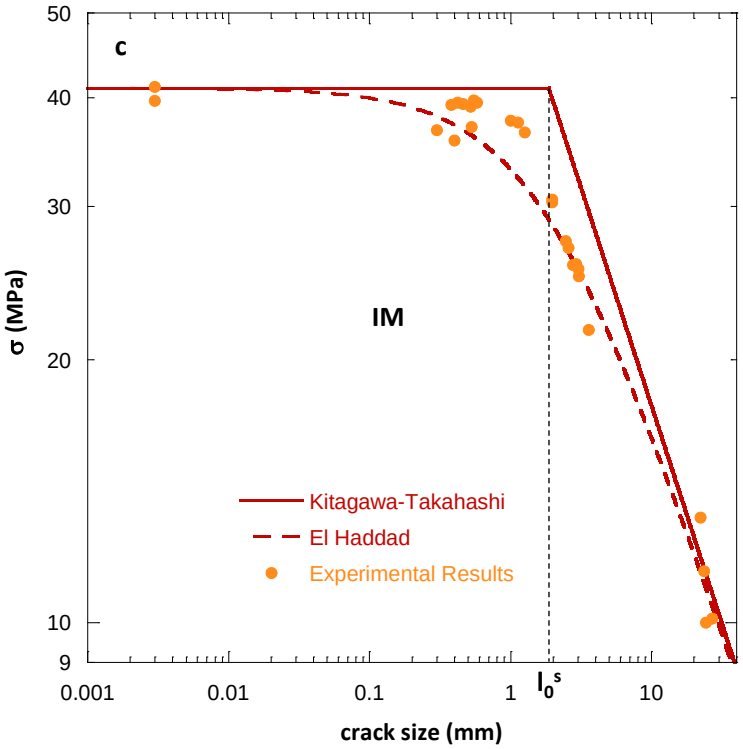

Figure 6-1. Residual strength diagrams including modified Kitagawa-Takahashi (continuous line) and El Haddad predictions (dashed line) of: a) SLS PA-12 at 0° orientation b) SLS PA-12 at 90° orientation and c) IM PA-12. Experimental data obtained from fracture tests and tensile tests carried out in plain specimens and samples with small and medium-size cracks are included as filled orange circles.

Experimental data from tensile tests and fracture tests presented in *sections 5.5* and *5.6*, respectively, were also included. The former was assigned a defect of equal size to the surface roughness shown in *section 5.2.* The diagrams were completed with the results obtained from monotonic loading tests carried out in specimens with small and medium-size crack lengths in the range between 0.2 and 3 mm for *SLS* at 0° orientation and for *IM* PA-12.

To get an easier visual comparison of the materials, *Figure 6-2* displays the three residual strength curves for static loading all together. *SLS* PA-12 in the *MSC* regime shows higher allowable stresses, due to their higher tensile

strengths, but the three materials present similar behaviours at *LC* regime. Differences in l_0^S for each material are also distinguished.

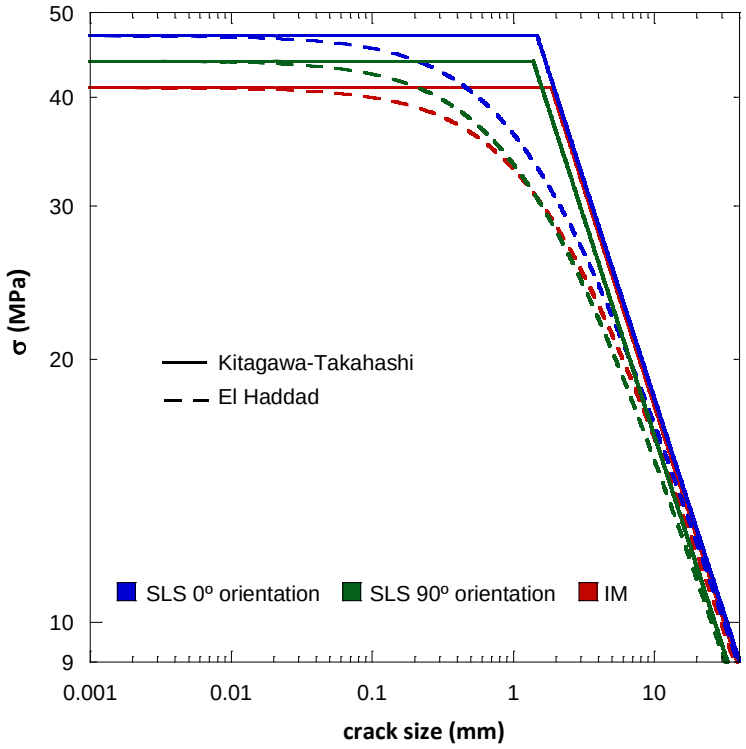

Figure 6-2 Residual strength diagrams including modified Kitagawa-Takahashi (continuous line) and El Haddad predictions (dashed line) for static loading of SLS PA-12 at 0° orientation (blue), SLS PA-12 at 90° orientation (green) and IM PA-12 (red).

The characteristic static lengths l_0^S are shown in *Table 6-1*. As it can be seen, both *SLS* PA-12 orientations have a similar l_0^S value, which is clearly smaller than that of *IM PA-12*.

A normalized diagram may help to unify all the results corresponding to different materials in just one curve. *Figure 6-3* contains the same information as the three curves presented in *Figure 6-1* but, in this case, the Y-axis was normalized by the tensile stress of each material and the X-axis was also normalized by the l_0^S values contained in *Table 6-1.*

Table 6-1.Characteristic static length, l_0^s.

Processing technique	Orientation	l_0^s(mm)
SLS	**0° orientation**	1.5
	90° orientation	1.4
IM	-	1.9

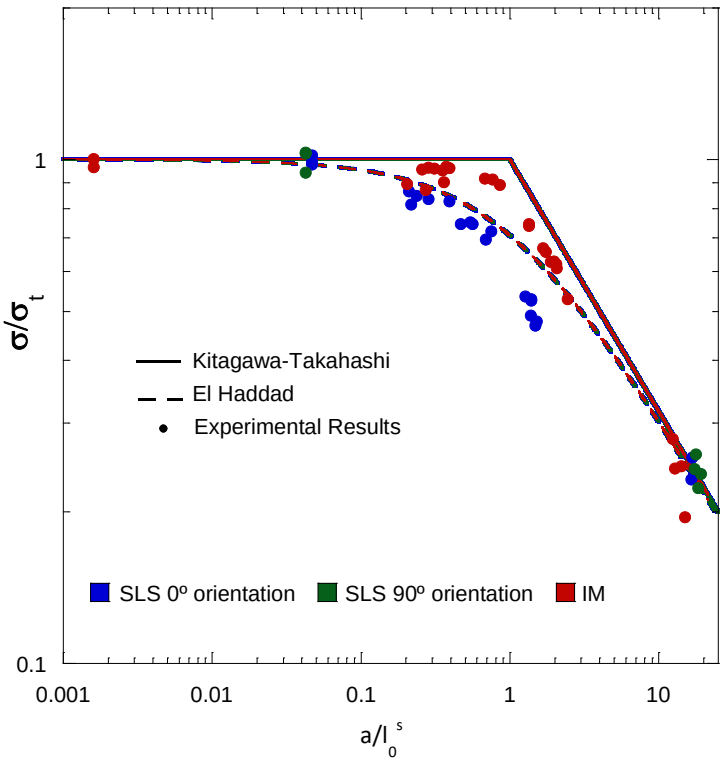

Figure 6-3. Normalized residual strength diagrams including modified Kitagawa-Takahashi (continuous line) and El Haddad predictions (dashed line) of SLS PA-12 at 0° orientation (blue), SLS PA-12 at 90° orientation (green) and IM PA-12 (red). Experimental data obtained from fracture tests and tensile tests carried out in plain specimens and samples with small and medium-size cracks are included as filled circles.

Figure 6-3 displays the prediction capabilities of the empirical models as the modified Kitagawa-Takahashi and El Haddad regarding the static strength of the PA-12 manufactured by different techniques. The diagram is a prediction

of the frontier between the integrity and the failure regimes and, consequently, the modified Kitagawa-Takahashi is too conservative. The modified El Haddad model provides better predictions as the experimental data tend to fall on the model curves.

6.2 INFINITE FATIGUE LIFETIME

The Kitagawa Takahashi diagrams including the predictions of El Haddad model for infinite fatigue lifetime have been constructed from the values of fatigue limit $\Delta\sigma_{fl}$ at 10^6 cycles and crack propagation threshold $\left(\Delta\sqrt{G}\right)_{th}$. As the stress range for infinite fatigue lifetime is calculated from the threshold stress intensity factor, ΔK_{th} (*eq. (2-4)*), all the data expressed in terms of the control parameter $\Delta\sqrt{G}$ were transformed using the following expression:

$$\Delta K = \Delta\sqrt{G}\sqrt{\frac{2E}{B\frac{dg}{d\alpha}}f(\alpha)} \qquad (6\text{-}4)$$

Figure 6-4 displays the Kitagawa-Takahashi diagrams of *SLS* and *IM* PA-12 specimens. Experimental data from $\Delta\sqrt{G}$-decreasing Fatigue Crack Propagation tests (*FCP* Results) have been depicted with filled orange circles, and the results employed for the calculation of the fatigue limit have been also drawn, the run-outs as diamonds and the failures as crosses. Despite the fatigue life tests were carried out in plain specimens, a defect size was assigned equal to the surface roughness measured and displayed in *section 5.2*. For *SLS* PA-12 at 0° orientation (*Figure 6-4.a)* and for the *IM* PA-12 (*Figure 6-4.c),* fatigue tests on specimens with small cracks were included.

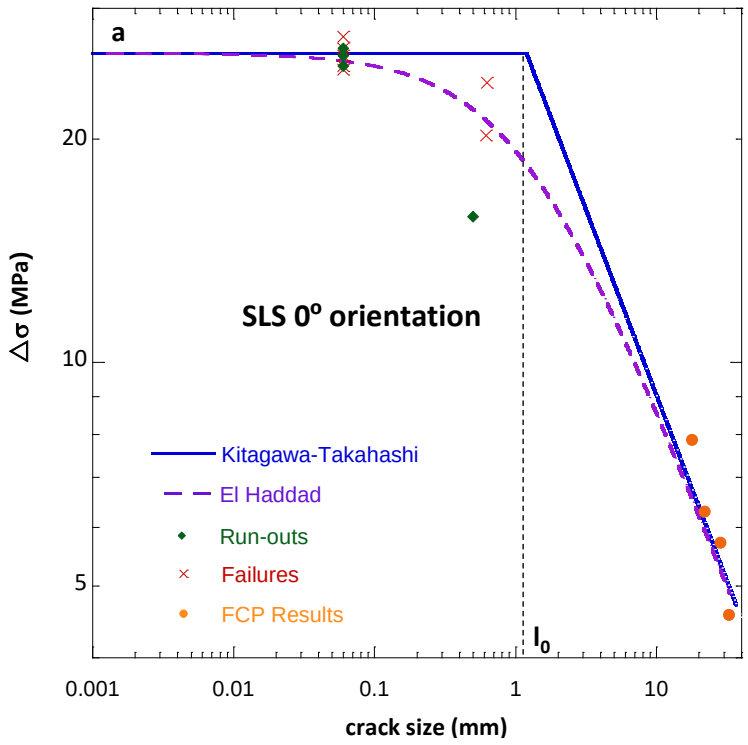
a
SLS 0º orientation
Δσ (MPa)
20
10
5
Kitagawa-Takahashi
El Haddad
Run-outs
Failures
FCP Results
l0
0.001
0.01
0.1
1
10
crack size (mm)

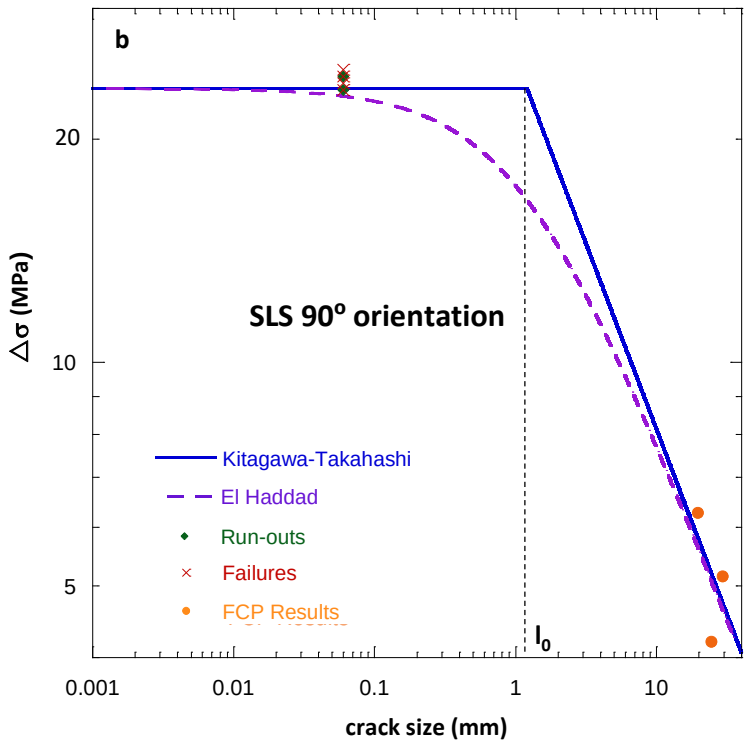
b
SLS 90º orientation
Δσ (MPa)
20
10
5
Kitagawa-Takahashi
El Haddad
Run-outs
Failures
FCP Results
l0
0.001
0.01
0.1
1
10
crack size (mm)

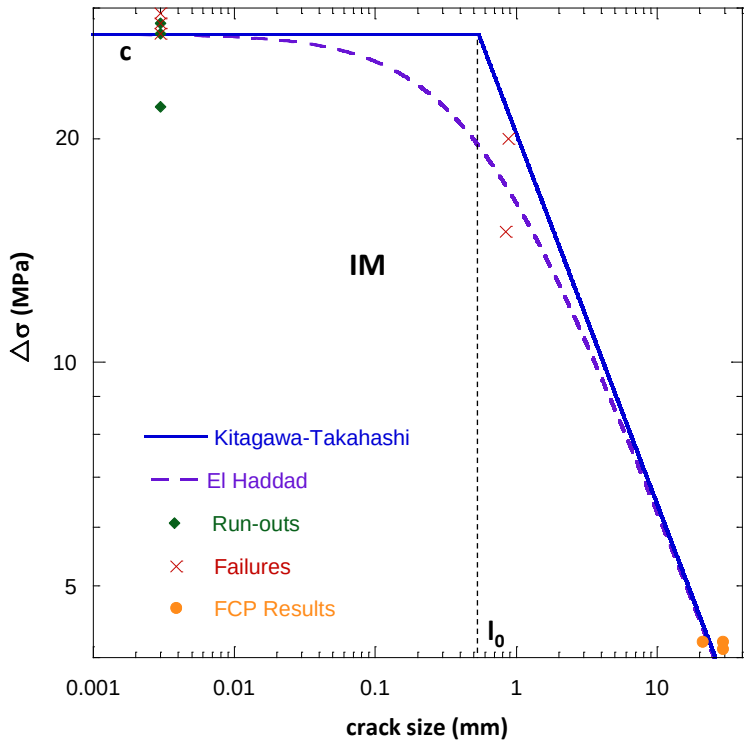

Figure 6-4. Kitagawa-Takahashi diagram (blue line) including El Haddad empirical model (purple line) of a) SLS PA-12 at 0° orientation, b) SLS PA-12 at 90° orientation and c) IM PA-12.ex Experimental data from $\Delta\sqrt{G}$-decreasing tests are plotted with orange filled circles, and the run-outs and failures of the tests employed for the fatigue limit determination are plotted as diamonds and crosses, respectively.

A characteristic length, l_0, can be obtained from the intersection of *MSC* and *LC* estimations (*equation (2-6)*) in the Kitagawa-Takahashi diagrams. This length can be considered as the limiting dimension of a subcritical defect, above which the long crack ΔK_{th} becomes the control parameter. *Table 6-2* shows the values of l_0 for the materials under study. While there are no differences between the characteristic lengths of SLS PA-12 at 0° and 90° orientations, the value of IM PA-12 is much smaller. Comparing the static characteristic length, l_0^S, (*Table 6-1*) and l_0 (*Table 6-2*), the latter is always smaller, ranging the difference from 25% in *SLS* PA-12 up to 300% in *IM* PA-12.

Table 6-2. Characteristic length, l_0, for the materials under study.

Processing technique	Orientation	l_0(mm)
SLS	**0° orientation**	1.2
	90° orientation	1.21
IM	**IM**	0.54

Figure 6-5 displays the Kitagawa-Takahashi diagrams and El Haddad model. As observed, the behaviour of the three materials differ, being *IM* PA-12 the most resistant in the MSC regime.

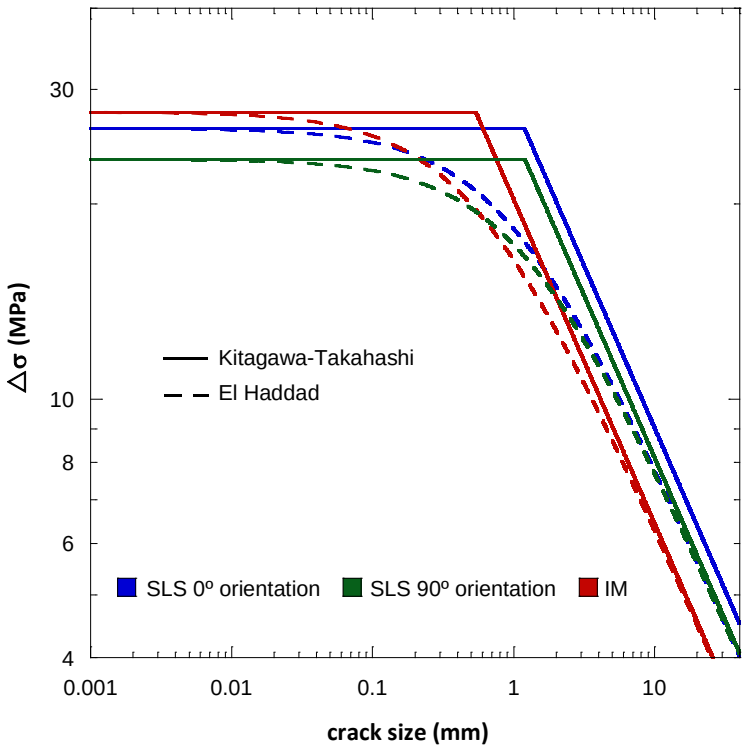

Figure 6-5. Kitagawa-Takahashi diagrams (continuous line) including El Haddad empirical models (dotted line) of SLS PA-12 at 0° orientation (blue), SLS PA-12 at 90° orientation (green) and IM PA-12 (red).

This could be accounted for the high number of defects in form of pores and unmolten particles present in *SLS* PA-12. On the other hand, in the *LC* regime, the trend is the opposite, as both *SLS* orientations undergo a better performance than *IM* PA-12. This may be linked to microstructural features. The spherulite size of *SLS* PA-12 is 4 times bigger than that of *IM* PA-12 (*Table 5-3*), and this could be the reason behind the higher long crack threshold values of the former.

The normalized diagram of *Figure 6-6* displays the complete behaviour of the PA-12 manufactured by different techniques. The stress range has been normalized by the corresponding fatigue limit values at 10^6 cycles for each material and the crack length by their characteristic length.

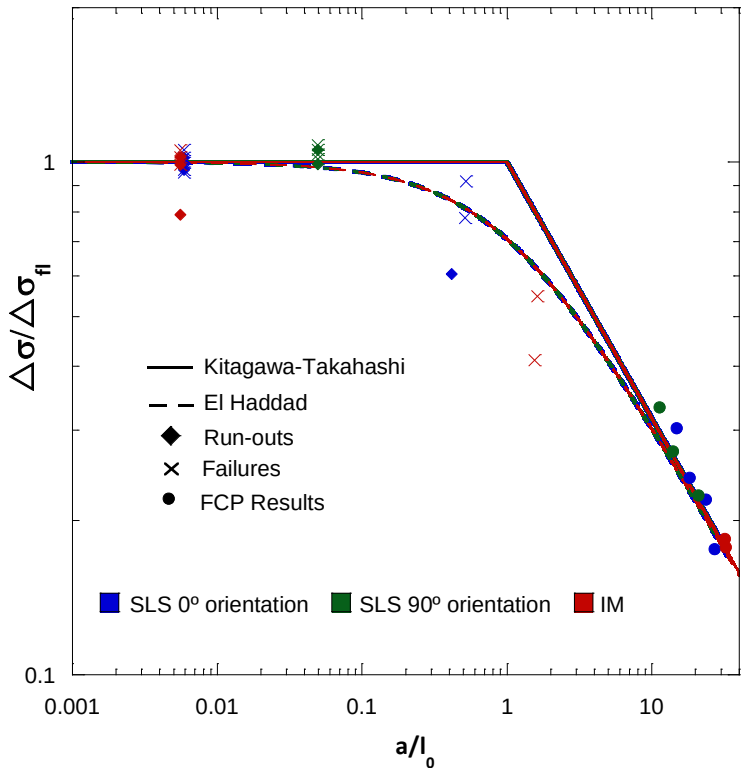

Figure 6-6. Kitagawa-Takahashi diagrams (continuous line) including El Haddad empirical models (dotted line) in normalized coordinates of SLS PA-12 at 0° orientation (blue), SLS PA-12 at 90° orientation (green) and IM PA-12 (red).

El Haddad model predictions are more accurate than those of the Kitagawa-Takahashi, especially for *SLS* PA-12. Nevertheless, for *IM* PA-12, El Haddad model does not seem to describe the PSC regime as some failures fall within the integrity zone.

6.3 FINITE FATIGUE LIFETIME

There are several authors (Larsen et al. [180], Ciavarella et al. [181]) who have included in the Kitagawa-Takahashi diagrams the residual strength curves and information about the finite fatigue lifetime. *Figure 6-7, Figure 6-8* and *Figure 6-9* display the Kitagawa-Takahashi diagrams (continuous line) and El Haddad model predictions (dashed line) for static and infinite fatigue lifetime of *SLS* PA-12 at 0° and 90°orientations, and of *IM* PA-12, respectively.

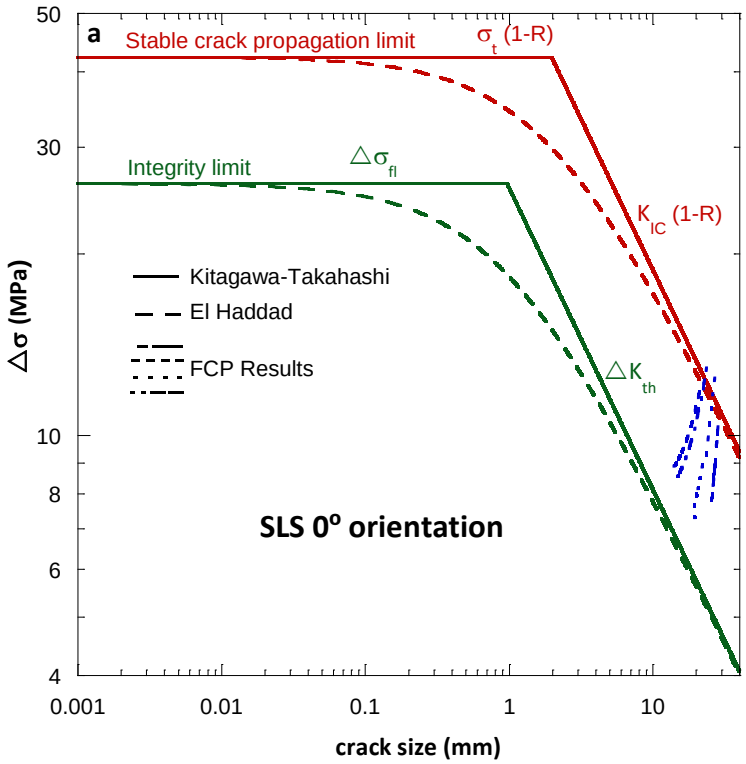

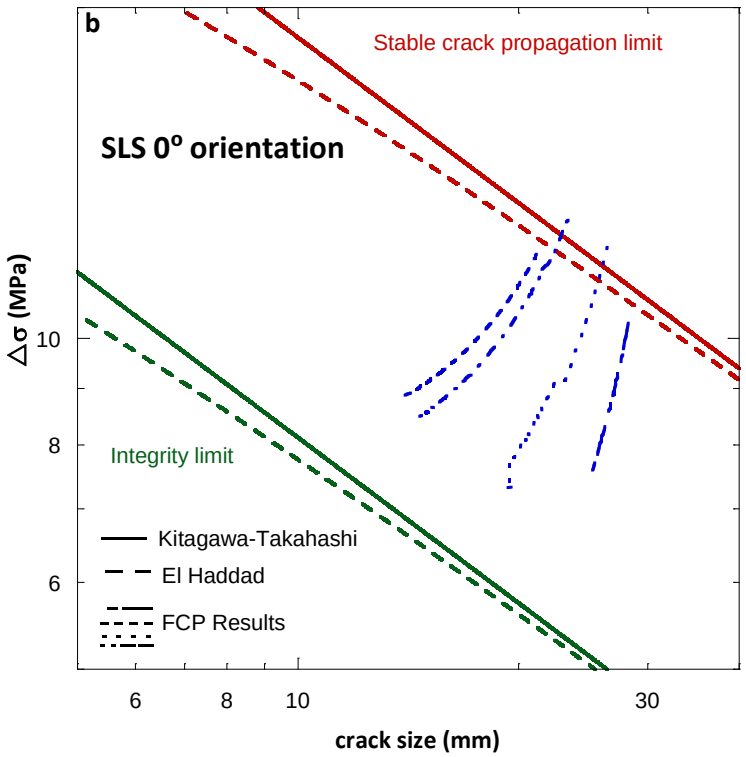

Figure 6-7. Kitagawa-Takahashi diagrams (continuous lines) including El Haddad empirical models (dotted lines) for infinite fatigue lifetime in green and for fracture at one cycle in red of SLS PA12 at 0° orientation: a) full diagrams and b) detail of LC regime with Fatigue Crack Propagation Results obtained from $\Delta\sqrt{G}$-increasing tests.

Red colour is used to represent the static boundary conditions and the infinite fatigue lifetime boundary below which no crack propagates is displayed in green. Between these two limits, finite fatigue life can be predicted by means of a combination of the lifetime fatigue curves and the crack growth propagation curves. In fact, in the LC regime, the Fatigue Crack Propagation curves obtained from $\Delta\sqrt{G}$-increasing tests (*FCP* Results) have been plotted in blue dotted lines.

With the aim of comparing the finite fatigue lifetime band, defined as tensile strength to fatigue limit ratio in *MSC* zone or fracture toughness to long crack threshold in *LC* regime, *Figure 6-10* displays all together the modified Kitagawa-Takahashi diagrams of *SLS* PA-12 at both orientations and of *IM* PA-12. In metals, the tensile strength to fatigue limit ratio tends to remain roughly constant, independently of the microstructure [182]. This is not the case for these materials. While this ratio holds constant independently of the orientation in *SLS* PA-12, it is reduced for *IM* PA-12. This supports the fact that the band size between these two limiting conditions in the MSC regime seems to be related to the defects population, which are more numerous in *SLS* PA-12.

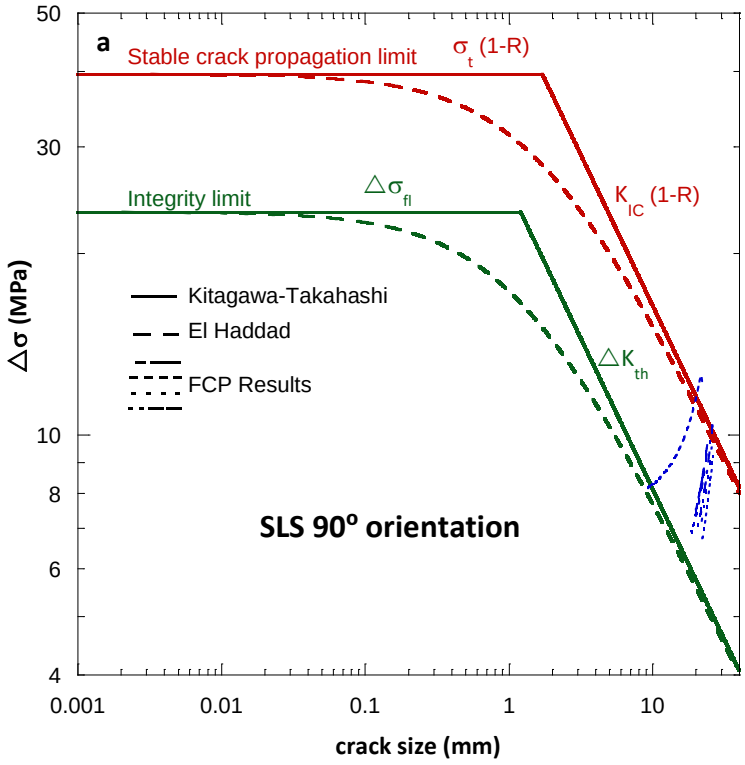

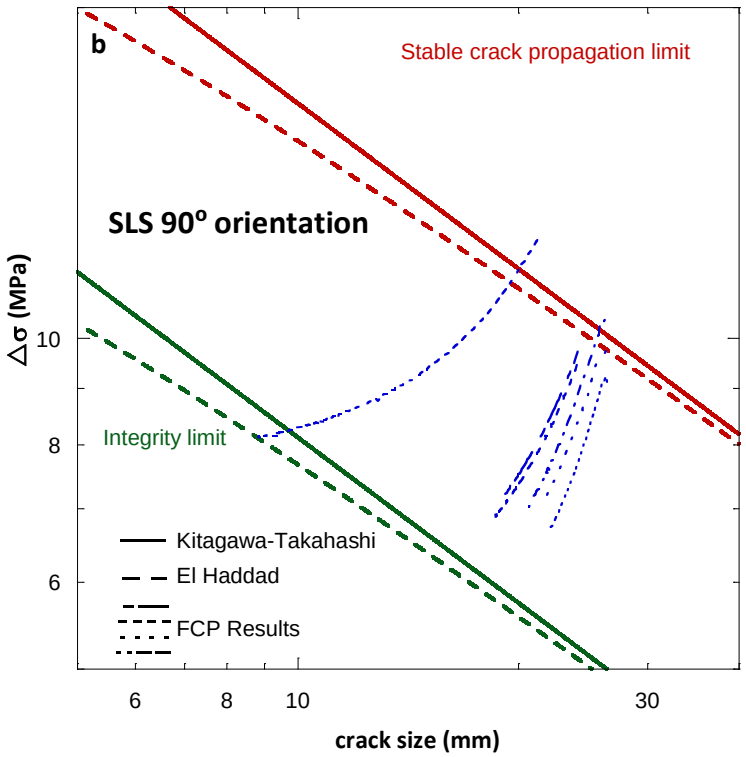

Figure 6-8. Kitagawa-Takahashi diagrams (continuous lines) including El Haddad empirical models (dotted lines) for infinite fatigue lifetime in green and for fracture at one cycle in red of SLS PA12 at 90° orientation: a) full diagrams and b) detail of LC regime with Fatigue Crack Propagation Results obtained from $\Delta\sqrt{G}$-increasing tests.

On the oher hand, in metals, the fracture toughness and the threshold values are closely related to microstructure [182]. In this study, in the *LC* regime, the fracture toughnes to long crack threshold values ratio of *IM* PA-12 was much higher than that of *SLS* PA-12, being hardly differences between 0° and 90° orientations in the former.

The fracture toughness is dependent on the spherulite size, being higher as the spherulite size is smaller, especially appreciated when the fracture values are expressed in terms of the J-integral (*Figure 5-24*). Nevertheless, although the threshold propagation values are lower in *IM* PA-12 and this could be linked to the smaller spherulitic dimension, this topic still needs further investigation.

Ciavarella et al. [181] extended the Kitagawa-Takahashi diagrams for finite life predictions by analogy in the construction of the originals. Therefore, for finite life N, the stress range for each crack length is obtained as the minimum of the stress range resulting from the Basquin law and the integrated form of the Paris law as follows:

$$\Delta\sigma(N,a) = min\left(\begin{array}{c}\left(\frac{B_B}{N}\right)^{\frac{1}{m_B}},\\ \left(\left(\frac{n-2}{2}\right)A\pi^{\frac{n}{2}}N\right)^{-\frac{1}{n}} a^{\frac{1}{n}-\frac{1}{2}}\end{array}\right) \qquad (6\text{-}5)$$

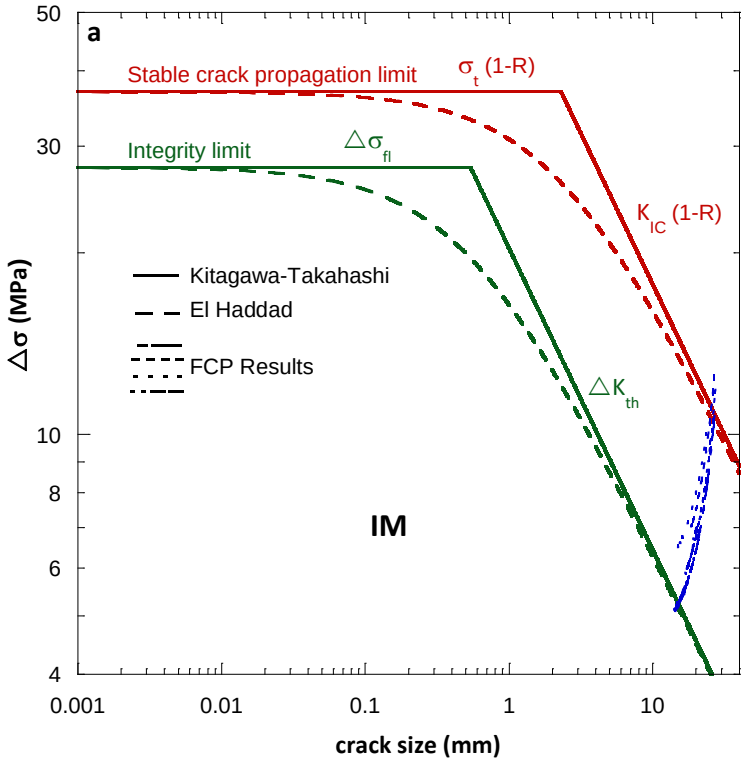

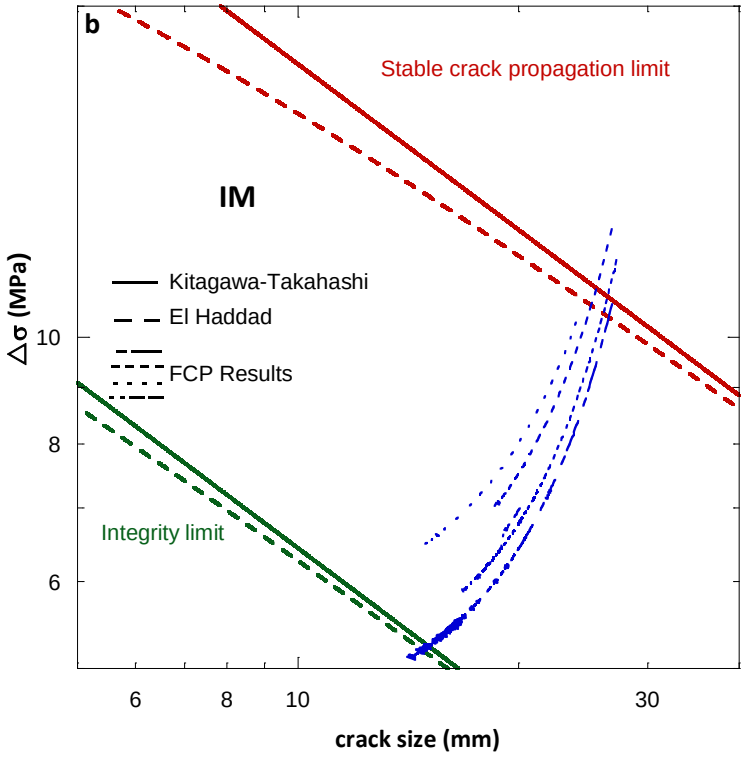

Figure 6-9. Kitagawa-Takahashi diagrams (continuous lines) including El Haddad empirical models (dotted lines) for infinite fatigue lifetime in green and for fracture at one cycle in red of IM PA12: a) full diagrams and b) detail of LC regime with Fatigue Crack Propagation Results obtained from $\Delta\sqrt{G}$-increasing tests.

In this case, the key issue is the transition from the Basquin dominated regime to the Paris dominated zone, which for a specific number of cycles, N, it is obtained by equating the stress range obtained from the Basquin law and the integrated form of the Paris law. In terms of crack size, l_t, it is given by [181]:

$$l_t(N) = \left(\left(\frac{n-2}{2} \right) A \pi^{\frac{n}{2}} B_B^{\frac{n}{m_B}} N^{m_B - \frac{n}{m_B}} \right)^{\frac{2}{2-n}} \qquad (6\text{-}6)$$

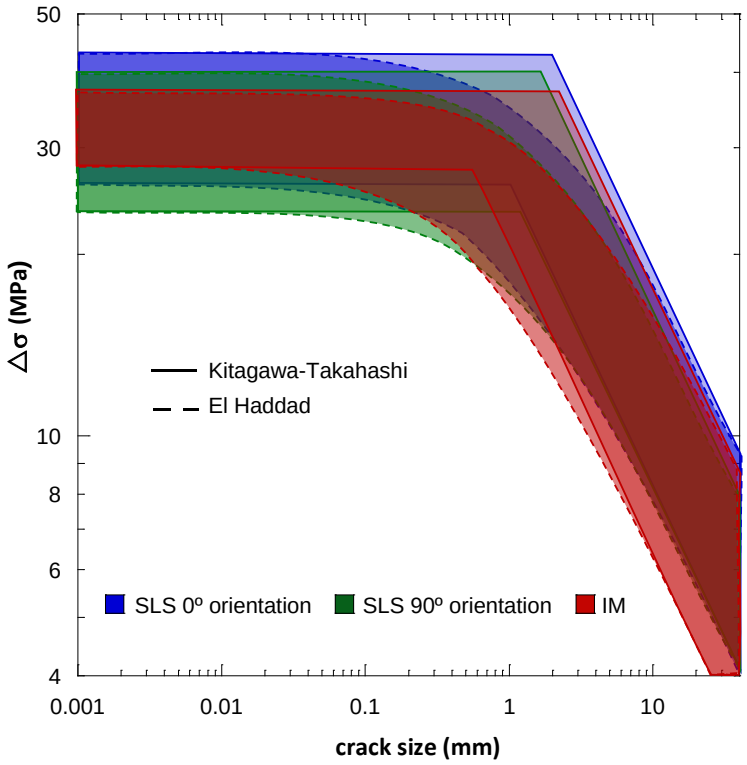

Figure 6-10. Schematic Kitagawa-Takahashi of SLS PA-12 at 0° orientation in blue, SLS PA-12 at 90° orientation in green and IM PA-12 in red.

As a way of example, *Figure 6-11 shows* the fatigue maps including finite life predictions for fatigue lifetimes of 10.000 cycles and 100.000 cycles of *SLS* PA-12 at 0° and 90°orientations and of *IM* PA-12. Normalized coordinates have been used, that is, the Y-coordinates have been divided by σ_t, and the X-coordinates by l_0^S, $l_t(N)$ or l_0 for static, finite life for a given number of cycles N and infinite life cases, respectively. Little differences were observed among the different materials, only that the region of possible crack propagation is smaller for *IM* PA-12.

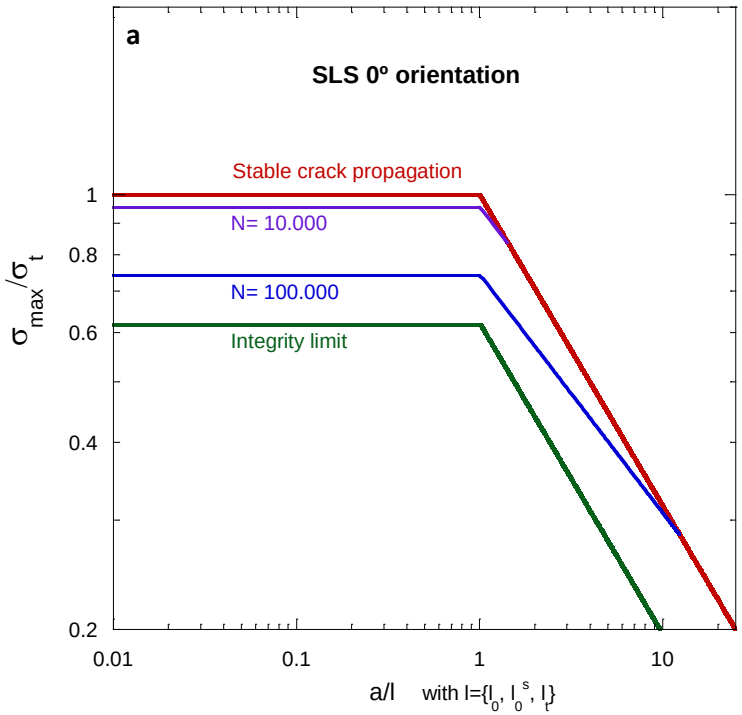
a
SLS 0º orientation
Stable crack propagation
N= 10.000
N= 100.000
Integrity limit
1
0.8
0.6
0.4
0.2
σmax/σt
0.01
0.1
1
10
a/l with l={l0, l0s, lt}

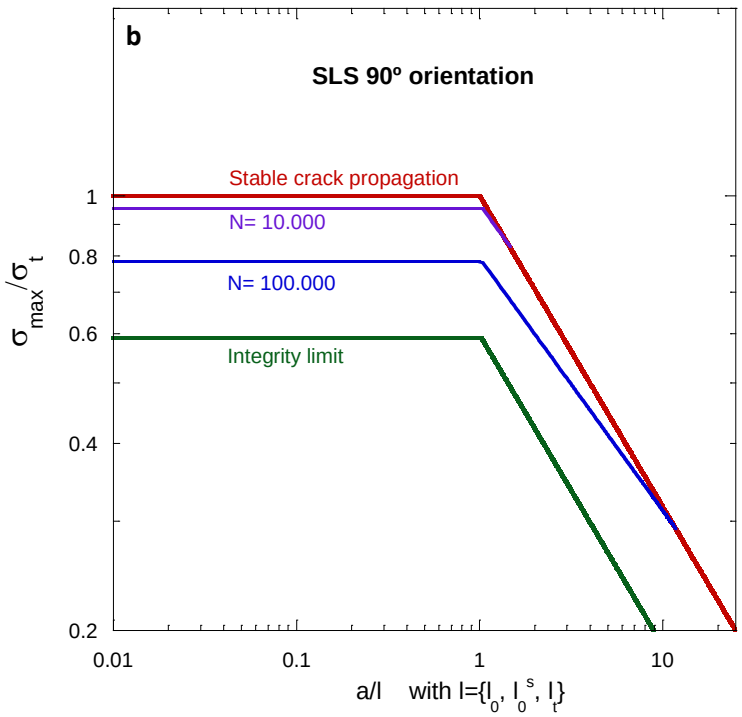
b
SLS 90º orientation
Stable crack propagation
N= 10.000
N= 100.000
Integrity limit
1
0.8
0.6
0.4
0.2
σmax/σt
0.01
0.1
1
10
a/l with l={l0, l0s, lt}

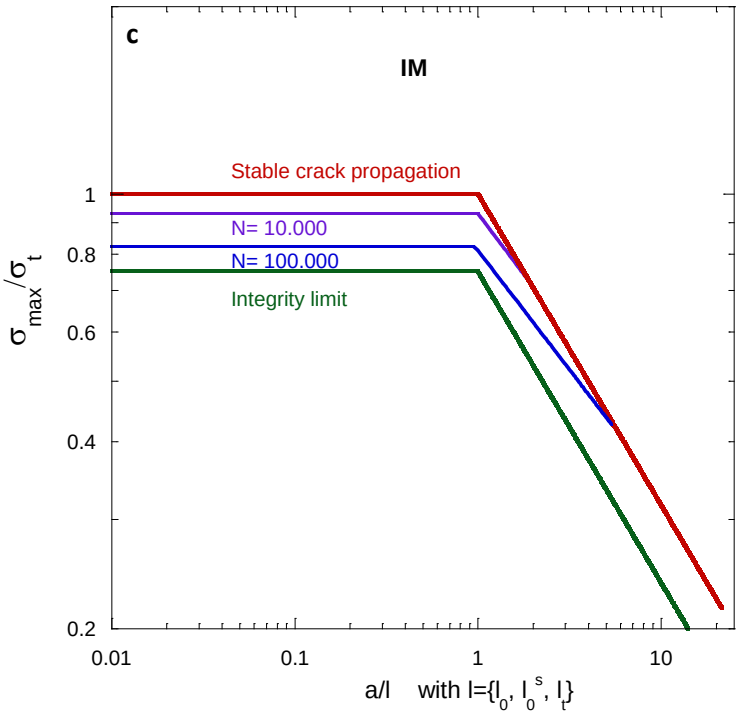

Figure 6-11. Maps of fatigue in normalized coordinates with extended Kitagawa-Takahashi diagrams to finite life with 10.000 cycles in purple and 100.000 cycles in blue between the boundary conditions for fracture and one cycle in red and infinite fatigue life in green of (a) SLS PA-12 at 0° orientation, (b) SLS PA-12 at 90° orientation and (c) IM PA-12.

6.4 ON THE PHYSICAL MEANING OF L_0

Especially in metals, many authors have tried to give a physical meaning to the characteristic lengths. When the values of l_0 are small, some authors have linked them to microstructural characteristics. El Haddad related them with the crystallographic grain size in steels and titanium alloys [127] and Ciavarella, also in steels, with the distance from the surface to the first microstructural barrier which the crack could found [181]. In other occasions, as in non-metals (building materials, composites or some polymers) or in materials with no microstructure because they are amorphous, the characteristic length can be associated with the size of the damage zone. In this case, the characteristic length can range from only some hundreds of microns to millimetres, being

mostly at least one order of magnitude larger than the microstructural features as there can be many factors involved in the creation and growth of the damage.

For the materials under study, the characteristic lengths could be associated neither with any microstructure feature (spherulite size, skin layer dimension, surface roughness, etc) nor with damage zone size. Therefore, further research should be done in this topic to elucidate if the values of l_0 obtained could be related to material properties or failure processes.

Chapter 7.

Conclusions

The main conclusion of this work is that the fatigue behaviour of PA-12 processed via *SLS* and *IM* was rather similar, which guarantees the use of parts fabricated by *SLS* in structural applications. Nevertheless, some particular differences were observed due to the presence of defects and microstructural features (spherulite size, anisotropy) induced by the processing technique. To endorse this statement, the following partial conclusions obtained from each of the characterisations carried out are detailed below.

- The thermal studies revealed that the degree of crystallinity of *SLS* samples was 10% lower than that of *IM*, with slightly higher transition temperatures.
- The morphological analysis showed that the spherulite size of the *SLS* was 50 ± 10 μm while in *IM* it was significantly lower, 13 ± 3 μm. Moreover, the *IM* specimens displayed a skin-core morphology, with an amorphous skin layer size of 14% of the total thickness of the specimen.
- *IM* specimens were almost full dense, while *SLS* specimens exhibited 4% of porosity. The surface roughness of *SLS* PA-12 at both orientations were 20 times larger than that of *IM* PA-12.
- Regarding the tensile properties, the most pronounced difference is found in the elongation at break, which could reach values in IM PA-12 up to 3 times higher than those measured in *SLS* at 0° orientation. Comparing *SLS* orientations, the elongation at break is again the main difference, from 10% at 90° to 30% at 0° orientations.
- All samples exhibited a non-linear fracture response with quite similar fracture toughness values independently of orientation and manufacturing technique. Nevertheless, the J-R curves of *SLS* at 0° orientation were above those of SLS at 90° orientation, being IM curves

in between. The energy at crack growth initiation was the highest for *IM* PA-12, with hardly differences between the two distinct orientations of *SLS* PA-12. This result is linked to the spherulite size: the higher the fracture toughness, the lower the spherulite size.

- The fatigue behaviour at R=0.1 and a frequency of 1 Hz was again very analogous independently of orientation and manufacturing technique, but it is worth pointing out that SLS PA-12 at 0° orientation presented the best fatigue performance of either plain specimens or fracture mechanics specimens, SLS at 90° orientation the worst and IM PA-12 had an intermediate behaviour. Behind this may be the low interlayer strength and the population of defects induced by the SLS technique.
- Regarding the fatigue limit and the long crack threshold values, *IM* PA-12 showed the highest fatigue limit and the lowest long crack threshold. Between *SLS* orientations, 0° orientation presented highest fatigue limit and threshold values than 90° orientation. These trends observed are again a consequence of the presence of defects, surface roughness and microstructural features such as spherulite size.
- The fatigue behaviour of PA-12 was described using the Kitagawa-Takahashi and El Haddad models. The predictions given by El Haddad model were more accurate than those of the Kitagawa-Takahashi diagram, especially for *SLS* PA-12 samples. The characteristic length that defines the limit between the short and long crack regimes was the lowest for *IM* PA-12, being scarce the differences between the two orientation of *SLS* PA-12.
- The Kitagawa-Takahashi and El Haddad models have been extended to include finite fatigue lifetime predictions. The tensile strength to fatigue

limit ratios showed that in the microstructural short crack region the lower interval of stress range values between integrity and critical crack propagation occurred in IM PA-12. The opposite trend was observed in the long crack regime.

- The mechanism of deformation and failure of *SLS* PA-12 for all testing configurations was the nucleation, growth and coalescences of crazes, promoted by the high population of defects in form of pores and or unmolten powder particles. This very same mechanism was observed in IM PA-12 in fracture mechanics specimens, that is, those used for fracture toughness and fatigue crack propagation characterisations. Nevertheless, for the plain specimens used for tensile tests and the determination of the S-N curves, the dominant mechanism was ductile tearing with necking formation and propagation along the gage length up to catastrophic failure.

Chapter 8.

Future work

The results obtained in this doctoral thesis suggest the need to complete the investigation carried out in some issues and to deepen the study in others. The proposed topics for future work are detailed below.

- To complete the experimental program to dispose a larger number of data specially for physically short crack regime.
- To deepen in the experimental methodology more adequate for the determination of the fatigue limit and long crack thresholds.
- To study the effect of stress ratio and the frequency on the diagrams of fatigue of polymers, taking into account thermal damage and viscoelasticity.
- To research the effect of the microstructural features (degree of crystallinity, spherulite size, skin-layer) on the fatigue parameters as the threshold values, the lifetime fatigue curves or the Paris law region.
- To analyse the physical meaning of the characteristic lengths and search relationships with the microstructural features or the damage process zone.
- To extend the analysis of design against fatigue to notched polymeric samples, using the Aztori-Lazzarin diagrams as a generalisation of the Kitagawa-Takahashi approach.

BIBLIOGRAPHY

[1] ASTM INTERNATIONAL, "ASTM F2792-12a," *Rapid Manuf. Assoc.*, pp. 1–3, 2013, doi: 10.1520/F2792-12A.2.

[2] P. Kocovic, *3D Printing and Its Impact on the Production of Fully Functional Components*. 2017. doi: 10.4018/978-1-5225-2289-8.

[3] K. Narsimlu, A. G. Pathak, A. G. Mulky and C. Yavarna, "A Market Analysis on impact of additive layer manufacturing technologies on aerospace and defense supply chain," *Int. J. Manag.*, vol. 8, no. 2, pp. 171–187, 2017.

[4] D. M. J. Cotteleer, "3D opportunity: Additive manufacturing paths to performance, innovation, and growth," *LLP Online*, 2014, [Online]. Available: http://cellular3d.com/images/marketresearch/SIMT_AM_Conference_Keynote-Oct2014.pdf

[5] M. Stöcker and J. Mitchell, "From rapid prototyping to rapid manufacturing," *Auto Technol.*, vol. 2, pp. 38–39, 2002.

[6] R. I. Noorani, *Rapid prototyping: principles and applications*. Wiley, 2005.

[7] N. Hopkinson, R. J. M. Hague and P. M. Dickens, *Rapid Manufacturing: An Industrial Revolution for the Digital Age*. 2006. doi: 10.1002/0470033991.ch9.

[8] Wohlers Associates, *Wohlers Report*. 2019.

[9] M. Bhuvanesh Kumar and P. Sathiya, "Methods and materials for

additive manufacturing: A critical review on advancements and challenges," *Thin-Walled Struct.*, vol. 159, no. October 2020, p. 107228, 2021, doi: 10.1016/j.tws.2020.107228.

[10] C. de Vries, "Volkswagen Autoeuropa: Maximizing Production Efficiency with 3D Printed Tools and Fixtures," *Ultim. B.V.*, 2017.

[11] S. van de Staak, "Royal Netherlands Air Force: Speeding up maintenance with 3D printed tools," 2018.

[12] S. Publishing, *Additive Manufacturing Opportunities In Automotive*. 2018.

[13] B. Redwood, F. Schöffer and B. Garret, *The 3D Printing Handbook*. 2017.

[14] Dassault Sytèmes, "Introduction to 3D printing - additive processes." https://make.3dexperience.3ds.com/processes/3D-printing

[15] J. R. C. Dizon, A. H. Espera, Q. Chen and R. C. Advincula, "Mechanical characterization of 3D-printed polymers," *Addit. Manuf.*, vol. 20, pp. 44–67, 2018, doi: 10.1016/j.addma.2017.12.002.

[16] K. Deshmukh, A. Muzaffar, T. Kovářík, T. Křenek, M. B. Ahamed and S. K. K. Pasha, *Fundamentals and applications of 3D and 4D printing of polymers: Challenges in polymer processing and prospects of future research*. 2019. doi: 10.1016/B978-0-12-816805-9.00017-X.

[17] P. Dudek and A. Rapacz-Kmita, "Rapid prototyping: Technologies, materials and advances," *Arch. Metall. Mater.*, vol. 61, no. 2A, pp. 891–895, 2016, doi: 10.1515/amm-2016-0151.

[18] S. Yuan, F. Shen, C. K. Chua and K. Zhou, "Polymeric composites for powder-based additive manufacturing: Materials and applications," *Prog. Polym. Sci.*, vol. 91, pp. 141–168, 2019, doi: 10.1016/j.progpolymsci.2018.11.001.

[19] M. Schmid, A. Amado and K. Wegener, "Polymer powders for selective laser sintering (SLS)," *AIP Conf. Proc.*, vol. 1664, no. 2015, 2015, doi: 10.1063/1.4918516.

[20] D. Bourell *et al.*, "Materials for additive manufacturing," *CIRP Ann. - Manuf. Technol.*, vol. 66, no. 2, pp. 659–681, 2017, doi: 10.1016/j.cirp.2017.05.009.

[21] K. Dotchev and W. Yusoff, "Recycling of polyamide 12 based powders in

the laser sintering process," *Rapid Prototyp. J.*, vol. 15, no. 3, pp. 192–203, May 2009, doi: 10.1108/13552540910960299.

[22] D. Drummer, D. Rietzel and F. Kühnlein, "Development of a characterization approach for the sintering behavior of new thermoplastics for selective laser sintering," *Phys. Procedia*, vol. 5, no. PART 2, pp. 533–542, 2010, doi: 10.1016/j.phpro.2010.08.081.

[23] S. C. Ligon, R. Liska, J. Stampfl, M. Gurr and R. Mülhaupt, "Polymers for 3D Printing and Customized Additive Manufacturing," *Chem. Rev.*, vol. 117, no. 15, pp. 10212–10290, 2017, doi: 10.1021/acs.chemrev.7b00074.

[24] R. D. Goodridge, C. J. Tuck and R. J. M. Hague, "Laser sintering of polyamides and other polymers," *Prog. Mater. Sci.*, vol. 57, no. 2, pp. 229–267, 2012, doi: 10.1016/j.pmatsci.2011.04.001.

[25] K. S. R. Chandran, "Mechanical fatigue of polymers: A new approach to characterize the S-N behavior on the basis of macroscopic crack growth mechanism," *Polymer (Guildf).*, vol. 91, pp. 222–238, 2016, doi: 10.1016/j.polymer.2016.03.058.

[26] M. A. Castillo Acero, F. M. de la Escalera and Y. Essa, "Morphing Technology for Advanced Future Commercial Aircrafts," in *Morphing Wing Technologies*, A. Concilio, I. Dimino, L. Lecce and R. Pecora, Eds. Butterworth-Heinemann, 2018, pp. 585–618.

[27] J. Cheng, S. Lao, K. Nguyen, W. Ho, A. Cummings and J. Koo, "SLS processing studies of nylon 11 nanocomposites," *16th Solid Free. Fabr. Symp. SFF 2005*, no. January 2005, pp. 141–149, 2005.

[28] EOS, "Datasheet PA 2200." 2018.

[29] 3D Systems, "DuraForm PA." 2017. [Online]. Available: https://es.3dsystems.com/sites/default/files/2017-03/3D-Systems_DuraForm_PA_DATASHEET_USEN_2017.03.22_a_WEB.pdf

[30] B. Van Hooreweder, D. Moens, R. Boonen, J. P. Kruth and P. Sas, "On the difference in material structure and fatigue properties of nylon specimens produced by injection molding and selective laser sintering," *Polym. Test.*, vol. 32, no. 5, pp. 972–981, 2013, doi: 10.1016/j.polymertesting.2013.04.014.

[31] R. Seltzer, F. M. de la Escalera and J. Segurado, "Effect of water

conditioning on the fracture behavior of PA12 composites processed by selective laser sintering," *Mater. Sci. Eng. A*, vol. 528, no. 22–23, pp. 6927–6933, 2011, doi: 10.1016/j.msea.2011.05.045.

[32] R. D. Goodridge, R. J. M. Hague and C. J. Tuck, "Effect of long-term ageing on the tensile properties of a polyamide 12 laser sintering material," *Polym. Test.*, vol. 29, no. 4, pp. 483–493, 2010, doi: 10.1016/j.polymertesting.2010.02.009.

[33] B. Caulfield, P. E. McHugh and S. Lohfeld, "Dependence of mechanical properties of polyamide components on build parameters in the SLS process," *J. Mater. Process. Technol.*, vol. 182, no. 1–3, pp. 477–488, 2007, doi: 10.1016/j.jmatprotec.2006.09.007.

[34] T. Stichel *et al.*, "A Round Robin study for Selective Laser Sintering of polyamide 12: Microstructural origin of the mechanical properties," *Opt. Laser Technol.*, vol. 89, no. July 2016, pp. 31–40, 2017, doi: 10.1016/j.optlastec.2016.09.042.

[35] T. L. Starr, T. J. Gornet and J. S. Usher, "The effect of process conditions on mechanical properties of laser-sintered nylon," *Rapid Prototyp. J.*, vol. 17, no. 6, pp. 418–423, 2011, doi: 10.1108/13552541111184143.

[36] N. Lammens, M. Kersemans, I. De Baere and W. Van Paepegem, "On the visco-elasto-plastic response of additively manufactured polyamide-12 (PA-12) through selective laser sintering," *Polym. Test.*, vol. 57, pp. 149–155, 2017, doi: 10.1016/j.polymertesting.2016.11.032.

[37] S. Dupin, O. Lame, C. Barrès and J. Y. Charmeau, "Microstructural origin of physical and mechanical properties of polyamide 12 processed by laser sintering," *Eur. Polym. J.*, vol. 48, no. 9, pp. 1611–1621, 2012, doi: 10.1016/j.eurpolymj.2012.06.007.

[38] D. J. Hitt, B. Haworth and N. Hopkinson, "Fracture mechanics approach to compare laser sintered parts and injection mouldings of nylon-12," *Proc. Inst. Mech. Eng. Part B J. Eng. Manuf.*, vol. 225, no. 9, pp. 1663–1672, 2011, doi: 10.1177/0954405411402141.

[39] A. Salazar, A. Rico, J. Rodríguez, J. Segurado Escudero, R. Seltzer and F. Martin De La Escalera Cutillas, "Fatigue crack growth of SLS polyamide 12: Effect of reinforcement and temperature," *Compos. Part B Eng.*, vol. 59, pp. 285–292, 2014, doi: 10.1016/j.compositesb.2013.12.017.

[40] A. Salazar, A. Rico, J. Rodríguez, J. Segurado Escudero, R. Seltzer and F. Martin De La Escalera Cutillas, "Monotonic loading and fatigue response of a bio-based polyamide PA11 and a petrol-based polyamide PA12 manufactured by selective laser sintering," *Eur. Polym. J.*, vol. 59, pp. 36–45, 2014, doi: 10.1016/j.eurpolymj.2014.07.016.

[41] T. Brugo, R. Palazzetti, S. Ciric-Kostic, X. T. Yan, G. Minak and A. Zucchelli, "Fracture mechanics of laser sintered cracked polyamide for a new method to induce cracks by additive manufacturing," *Polym. Test.*, vol. 50, pp. 301–308, 2016, doi: 10.1016/j.polymertesting.2016.01.024.

[42] A. Salazar, J. Rodríguez, A. Segovia and A. B. Martínez, "Influence of the notch sharpening technique on the fracture toughness of bulk ethylene-propylene block copolymers," *Polym. Test.*, vol. 29, no. 1, pp. 49–59, 2010, doi: 10.1016/j.polymertesting.2009.09.004.

[43] A. B. Martínez, A. Salazar, N. León, S. Illescas and J. Rodríguez, "Influence of the notch-sharpening technique on styrene-acrylonitrile fracture behavior," *J. Appl. Polym. Sci.*, vol. 133, no. 32, pp. 1–14, Aug. 2016, doi: 10.1002/app.43775.

[44] M. Crespo, M. T. Gómez-del Río and J. Rodríguez, "Failure of SLS polyamide 12 notched samples at high loading rates," *Theor. Appl. Fract. Mech.*, vol. 92, pp. 233–239, Dec. 2017, doi: 10.1016/j.tafmec.2017.08.008.

[45] M. Crespo, T. Gómez-del Río and J. Rodríguez, "Failure of polyamide 12 notched samples manufactured by selective laser sintering," *J. Strain Anal. Eng. Des.*, vol. 54, no. 3, pp. 192–198, Apr. 2019, doi: 10.1177/0309324719847817.

[46] E. Linul, L. Marsavina and D. I. Stoia, "Mode I and II fracture toughness investigation of Laser-Sintered Polyamide," *Theor. Appl. Fract. Mech.*, vol. 106, no. December 2019, p. 102497, 2020, doi: 10.1016/j.tafmec.2020.102497.

[47] J. Schneider and S. Kumar, "Multiscale characterization and constitutive parameters identification of polyamide (PA12) processed via selective laser sintering," *Polym. Test.*, vol. 86, no. December 2019, p. 106357, 2020, doi: 10.1016/j.polymertesting.2020.106357.

[48] D. I. Stoia, L. Marşavina and E. Linul, "Correlations between Process Parameters and Outcome Properties of Laser-Sintered Polyamide,"

Polymers (Basel)., vol. 11, no. 11, p. 1850, Nov. 2019, doi: 10.3390/polym11111850.

[49] J. A. Hertzberg, R.W., Manson, *Fatigue of Engineering Plastics*. New York: Academic Press, New York, 1980.

[50] M. T. Takemori, "Polymer Fatigue.," *Annu. Rev. Mater. Sci.*, vol. 14, pp. 171–204, 1984, doi: 10.1146/annurev.ms.14.080184.001131.

[51] J. A. Sauer and G. C. Richardson, "Fatigue of polymers," *Int. J. Fract.*, vol. 16, no. 6, pp. 499–532, Dec. 1980, doi: 10.1007/BF02265215.

[52] R. I. Stephens, A. Fatemi, R. R. Stephens and H. O. Fuchs, *Metal Fatigue in Engineering*. 2000.

[53] R. W. Hertzberg, R. P. Vinci and J. L. Hertzberg, *Deformation and Fracture Mechanics of Engineering Materials*, 5th Editio. 2012.

[54] R. J. Crawford and P. P. Benham, "Cyclic stress fatigue and thermal softening failure of a thermoplastic," *J. Mater. Sci.*, vol. 9, no. 1, pp. 18–28, Jan. 1974, doi: 10.1007/BF00554752.

[55] D. Hülsbusch, A. Kohl, P. Striemann, M. Niedermeier, J. Strauch and F. Walther, "Development of an energy-based approach for optimized frequency selection for fatigue testing on polymers – Exemplified on polyamide 6," *Polym. Test.*, vol. 81, p. 106260, Jan. 2020, doi: 10.1016/j.polymertesting.2019.106260.

[56] V. Hirschberg, M. Wilhelm and D. Rodrigue, "Combining mechanical and thermal surface fourier transform analysis to follow the dynamic fatigue behavior of polymers," *Polym. Test.*, vol. 96, p. 107070, Apr. 2021, doi: 10.1016/j.polymertesting.2021.107070.

[57] J. D. Ferry, *Viscoelastic Properties of Polymers*, 3rd Editio. 1980.

[58] M. N. Riddell, G. P. Koo and J. L. O'Toole, "Fatigue mechanisms of thermoplastics," *Polym. Eng. Sci.*, vol. 6, no. 4, pp. 363–368, Oct. 1966, doi: 10.1002/pen.760060414.

[59] J. A. Sauer, E. Foden and D. R. Morrow, "Influence of molecular weight on fatigue behavior of polyethylene and polystyrene," *Polym. Eng. Sci.*, vol. 17, no. 4, pp. 246–250, Apr. 1977, doi: 10.1002/pen.760170407.

[60] M. Eftekhari and A. Fatemi, "On the strengthening effect of increasing cycling frequency on fatigue behavior of some polymers and their

composites: Experiments and modeling," *Int. J. Fatigue*, vol. 87, pp. 153–166, 2016, doi: 10.1016/j.ijfatigue.2016.01.014.

[61] J. A. Sauer and C. C. Chen, "Crazing and fatigue behavior in one- and two-phase glassy polymers," in *Crazing in Polymers*, Berlin/Heidelberg: Springer-Verlag, 1983, pp. 169–224. doi: 10.1007/BFb0024058.

[62] M. D. Skibo, R. W. Hertzberg and J. A. Manson, "Fatigue fracture processes in polystyrene," *J. Mater. Sci.*, vol. 11, no. 3, pp. 479–490, Mar. 1976, doi: 10.1007/BF00540929.

[63] S. Arad, J. C. Radon and L. E. Culvcr, "Fatigue Crack Propagation in Polymethylmethacrylate; the Effect of Loading Frequency," *J. Mech. Eng. Sci.*, vol. 14, no. 5, pp. 328–334, Oct. 1972, doi: 10.1243/JMES_JOUR_1972_014_040_02.

[64] R. W. Hertzberg, J. A. Manson and M. Skibo, "Frequency sensitivity of fatigue processes in polymeric solids," *Polym. Eng. Sci.*, vol. 15, no. 4, pp. 252–260, Apr. 1975, doi: 10.1002/pen.760150404.

[65] R. W. Hertzberg, M. D. Skibo, J. A. Manson and J. K. Donald, "Comments on 'A model of fatigue crack growth in polymers,'" *J. Mater. Sci.*, vol. 14, no. 7, pp. 1754–1759, Jul. 1979, doi: 10.1007/BF00569299.

[66] J. M. Schultz, "Fatigue behaviour of engineering polymers," *Treatise Mater. Sci. Technol.*, vol. 10, no. B, pp. 599–636, 1977.

[67] A. K. Shojaei and A. R. Wedgewood, "An anisotropic cyclic plasticity, creep and fatigue predictive tool for unfilled polymers," *Mech. Mater.*, vol. 106, pp. 20–34, Mar. 2017, doi: 10.1016/j.mechmat.2017.01.003.

[68] M. T. Takemori, "Shear and craze competition in subcritical fatigue crack growth: Fatigue lifetime inversions," *Polym. Eng. Sci.*, vol. 27, no. 1, pp. 46–54, Jan. 1987, doi: 10.1002/pen.760270108.

[69] J. L. Weaver and C. L. Beatty, "The effect of temperature on compressive fatigue of polystyrene," *Polym. Eng. Sci.*, vol. 18, pp. 1117–1126, 1978.

[70] H. Nishimura, A. Nakashiba, M. Nakakura and K. Sasai, "Fatigue behavior of medium-density polyethylene pipes for gas distribution," *Polym. Eng. Sci.*, vol. 33, no. 14, pp. 895–900, Jul. 1993, doi: 10.1002/pen.760331405.

[71] S. Hobeika, Y. Men and G. Strobl, "Temperature and Strain Rate

Independence of Critical Strains in Polyethylene and Poly(ethylene- c o -vinyl acetate)," *Macromolecules*, vol. 33, no. 5, pp. 1827–1833, Mar. 2000, doi: 10.1021/ma9910484.

[72] K. Noda, A. Takahara and T. Kajiyama, "Fatigue failure mechanisms of short glass-fiber reinforced nylon 66 based on nonlinear dynamic viscoelastic measurement," *Polymer (Guildf).*, vol. 42, no. 13, pp. 5803–5811, Jun. 2001, doi: 10.1016/S0032-3861(00)00897-1.

[73] F. Baltenneck, J.-P. Trotignon and J. Verdu, "Kinetics of fatigue failure of polystyrene," *Polym. Eng. Sci.*, vol. 37, no. 10, pp. 1740–1747, Oct. 1997, doi: 10.1002/pen.11822.

[74] J. G. Williams, "A model of fatigue crack growth in polymers," *J. Mater. Sci.*, vol. 12, no. 12, pp. 2525–2533, Dec. 1977, doi: 10.1007/BF00553940.

[75] N. E. Frost and D. S. Dugdale, "The propagation of fatigue cracks in sheet specimens," *J. Mech. Phys. Solids*, vol. 6, no. 2, pp. 92–110, Jan. 1958, doi: 10.1016/0022-5096(58)90018-8.

[76] N. E. Frost, K. J. Marsh and L. P. Pook, *Metal Fatigue*. 1974.

[77] W. Weibull, "A theory of fatigue crack propagation in sheet specimens," in *Acta Metallurgica*, 1963, pp. 745–752.

[78] P. C. Paris, M. P. Gomez and W. E. Anderson, "A rational analytic theory of fatigue," *Trend Eng.*, vol. 13, pp. 9–14, 1961.

[79] R. Boukhili, F. Decharentenay and T. Vukhanh, "Effect of frequency and orientation on fatigue crack propagation in polyamide-12," *Int. J. Fatigue*, vol. 8, no. 3, pp. 127–134, Jul. 1986, doi: 10.1016/0142-1123(86)90003-4.

[80] J. Karger-Kocsis, K. Friedrich and R. S. Bailey, "Fatigue crack propagation in short and long glass fiber reinforced injection-molded polypropylene composites," *Adv. Compos. Mater.*, vol. 1, no. 2, pp. 103–121, Jan. 1991, doi: 10.1163/156855191X00225.

[81] M. H. Kothmann, R. Zeiler, A. Rios de Anda, A. Brückner and V. Altstädt, "Fatigue crack propagation behaviour of epoxy resins modified with silica-nanoparticles," *Polymer (Guildf).*, vol. 60, pp. 157–163, Mar. 2015, doi: 10.1016/j.polymer.2015.01.036.

[82] F. Ramsteiner and T. Armbrust, “Fatigue crack growth in polymers,” *Polym. Test.*, vol. 20, no. 3, pp. 321–327, 2001, doi: 10.1016/S0142-9418(00)00039-8.

[83] J. Wainstein, M. Chapetti, P. E. Montemartini and P. Frontini, “Fatigue Crack Propagation Evaluation of Several Commercial Grade Propylene Polymers,” *Int. J. Polym. Mater.*, vol. 54, no. 7, pp. 575–587, Jul. 2005, doi: 10.1080/00914030390278707.

[84] M. N. James, C. J. Christopher, Y. Lu and E. A. Patterson, “Fatigue crack growth and craze-induced crack tip shielding in polycarbonate,” *Polymer (Guildf).*, vol. 53, no. 7, pp. 1558–1570, 2012, doi: 10.1016/j.polymer.2012.01.032.

[85] Q. Z. Fang, T. J. Wang and H. M. Li, “Overload-induced retardation of fatigue crack growth in polycarbonate,” *Int. J. Fatigue*, vol. 30, no. 8, pp. 1419–1429, 2008, doi: 10.1016/j.ijfatigue.2007.10.005.

[86] T. Colmer, S. R. Daniewicz, J. C. Newman and R. Moser, “Measuring fatigue crack growth and closure in Polyether Ether Ketone (PEEK),” *Int. J. Fatigue*, vol. 95, pp. 243–251, Feb. 2017, doi: 10.1016/j.ijfatigue.2016.10.025.

[87] S. Arad, J. C. Radon and L. E. Culver, “Fatigue Crack Propagation in Polymethylmethacrylate; the Effect of the Mean Value of Stress Intensity Factor,” *J. Mech. Eng. Sci.*, vol. 13, no. 2, pp. 75–81, Apr. 1971, doi: 10.1243/JMES_JOUR_1971_013_013_02.

[88] S. A. Sutton, “Fatigue crack propagation in an epoxy polymer,” *Eng. Fract. Mech.*, vol. 6, pp. 587–595, 1974.

[89] J. C. Radon, “Fatigue crack growth in polymers,” *Int. J. Fract.*, vol. 16, no. 6, pp. 533–552, Dec. 1980, doi: 10.1007/BF02265216.

[90] K. Sadananda and A. K. Vasudevan, “Analysis of fatigue crack growth behavior in polymers using the unified approach,” *Mater. Sci. Eng. A*, vol. 387–389, no. 1-2 SPEC. ISS., pp. 536–541, 2004, doi: 10.1016/j.msea.2004.01.115.

[91] C. Kanchanomai and A. Thammaruechuc, “Effects of stress ratio on fatigue crack growth of thermoset epoxy resin,” *Polym. Degrad. Stab.*, vol. 94, no. 10, pp. 1772–1778, 2009, doi: 10.1016/j.polymdegradstab.2009.06.012.

[92] M. Rink, B. Guidetti, R. Frassine and L. Castellani, “Effect of notch severity on fatigue fracture in a rubber-modified glassy polymer,” *J. Mater. Sci.*, vol. 29, no. 11, pp. 3071–3079, 1994, doi: 10.1007/BF01117622.

[93] J. Furmanski and L. A. Pruitt, “Peak stress intensity dictates fatigue crack propagation in UHMWPE,” *Polymer (Guildf).*, vol. 48, no. 12, pp. 3512–3519, 2007, doi: 10.1016/j.polymer.2007.04.006.

[94] A. Boonyapookana, A. Saengsai, S. Surapunt, K. Nagata and Y. Mutoh, “Time dependent fatigue crack growth behavior of silica particle reinforced epoxy resin composite,” *Int. J. Fatigue*, vol. 87, pp. 288–293, Jun. 2016, doi: 10.1016/j.ijfatigue.2016.02.013.

[95] M. Brillhart, B. L. Gregory and J. Botsis, “Fatigue fracture behaviour of PEEK: 1. Effects of load level,” *Polymer (Guildf).*, vol. 32, no. 9, pp. 1605–1611, Jan. 1991, doi: 10.1016/0032-3861(91)90395-Y.

[96] M. Brillhart and J. Botsis, “Fracture behaviour of PEEK: 2. Effects of thickness and temperature,” *Polymer (Guildf).*, vol. 33, no. 24, pp. 5226–5232, 1992.

[97] A. J. Kinloch, S. H. Lee and A. C. Taylor, “Improving the fracture toughness and the cyclic-fatigue resistance of epoxy-polymer blends,” *Polymer (Guildf).*, vol. 55, no. 24, pp. 6325–6334, Nov. 2014, doi: 10.1016/j.polymer.2014.10.018.

[98] W. Elber, “The significance of fatigue crack closure,” *ASTM STP*, vol. 486, pp. 230–243, 1971.

[99] A. J. Cano, A. Salazar and J. Rodríguez, “Evaluation of different crack driving forces for describing the fatigue crack growth behaviour of PET-G,” *Int. J. Fatigue*, vol. 107, no. October 2017, pp. 27–32, 2018, doi: 10.1016/j.ijfatigue.2017.10.013.

[100] C. Rans, R. Alderliesten and R. Benedictus, “Misinterpreting the results: How similitude can improve our understanding of fatigue delamination growth,” *Compos. Sci. Technol.*, vol. 71, no. 2, pp. 230–238, 2011, doi: 10.1016/j.compscitech.2010.11.010.

[101] M. Hojo, K. Tanaka, C. G. Gustafson and R. Hayashi, “Effect of stress ratio on near-threshold propagation of delimination fatigue cracks in unidirectional CFRP,” *Compos. Sci. Technol.*, vol. 29, no. 4, pp. 273–292,

1987, doi: 10.1016/0266-3538(87)90076-5.

[102] S. Mall, G. Ramamurthy and M. A. Rezaizdeh, “Stress ratio effect on cyclic debonding in adhesively bonded composite joints,” *Compos. Struct.*, vol. 8, no. 1, pp. 31–45, 1987.

[103] M. G. Wyzgoski and G. E. Novak, “Fatigue fracture of nylon polymers Part II Effect of g/ass-fibre reinforcement,” *J. Mater. Sci.*, vol. 26, pp. 6314–6324, 1991, doi: 10.1007/BF02387810.

[104] A. Pegoretti and T. Ricco, “Fatigue crack propagation in polypropylene reinforced with short glass fibers,” *Compos. Sci. Technol.*, vol. 59, pp. 1055–1062, 1999, doi: 10.1016/S0266-3538(98)00143-2.

[105] A. J. Brunner, N. Murphy and G. Pinter, “Development of a standardized procedure for the characterization of interlaminar delamination propagation in advanced composites under fatigue mode I loading conditions,” *Eng. Fract. Mech.*, vol. 76, no. 18, pp. 2678–2689, 2009, doi: 10.1016/j.engfracmech.2009.07.014.

[106] S. Azari, G. Jhin, M. Papini and J. K. Spelt, “Fatigue threshold and crack growth rate of adhesively bonded joints as a function of load/displacement ratio,” *Compos. Part A Appl. Sci. Manuf.*, vol. 57, pp. 59–66, 2014, doi: 10.1016/j.compositesa.2013.11.001.

[107] J. A. Pascoe, R. C. Alderliesten and R. Benedictus, “Methods for the prediction of fatigue delamination growth in composites and adhesive bonds - A critical review,” *Eng. Fract. Mech.*, vol. 112–113, pp. 72–96, 2013, doi: 10.1016/j.engfracmech.2013.10.003.

[108] R. Jones, S. Stelzer and A. J. Brunner, “Mode I, II and Mixed Mode I/II delamination growth in composites,” *Compos. Struct.*, vol. 110, no. 1, pp. 317–324, 2014, doi: 10.1016/j.compstruct.2013.12.009.

[109] R. Khan, R. Alderliesten, S. Badshah and R. Benedictus, “Effect of stress ratio or mean stress on fatigue delamination growth in composites: Critical review,” *Compos. Struct.*, vol. 124, pp. 214–227, 2015, doi: 10.1016/j.compstruct.2015.01.016.

[110] R. Jones, A. J. Kinloch and W. Hu, “Cyclic-fatigue crack growth in composite and adhesively-bonded structures: The FAA slow crack growth approach to certification and the problem of similitude,” *Int. J. Fatigue*, vol. 88, pp. 10–18, 2016, doi: 10.1016/j.ijfatigue.2016.03.008.

[111] I. Simon, L. Banks-Sills and V. Fourman, “Mode I delamination propagation and R-ratio effects in woven composite DCB specimens for a multi-directional layup,” *Int. J. Fatigue*, vol. 96, pp. 237–251, Mar. 2017, doi: 10.1016/j.ijfatigue.2016.12.005.

[112] Rapra, “Polyamides as Engineering Thermoplastic Materials,” *I.B. Page*, 2001.

[113] L. W. McKeen, “Polyamides (Nylons),” in *Fatigue and Tribological Properties of Plastics and Elastomers, second edition*, William Andrew Publishing, 2010, pp. 175–228.

[114] J. Happian-Smith, *An introduction to modern vehicle design*. Reed Educational and Professional Publising Ltd, 2001.

[115] A. Paesano and D. Ph, “Polymeric Additive Manufacturing : Present Status and Future Trends of Materials and Processes,” 2016.

[116] B. Van Hooreweder, F. De Coninck, D. Moens, R. Boonen and P. Sas, “Microstructural characterization of SLS-PA12 specimens under dynamic tension/compression excitation,” *Polym. Test.*, vol. 29, no. 3, pp. 319–326, 2010, doi: 10.1016/j.polymertesting.2009.12.006.

[117] B. Van Hooreweder and J. P. Kruth, “High cycle fatigue properties of selective laser sintered parts in polyamide 12,” *CIRP Ann. - Manuf. Technol.*, vol. 63, no. 1, pp. 241–244, 2014, doi: 10.1016/j.cirp.2014.03.060.

[118] J. Munguia and K. Dalgarno, “Fatigue behaviour of laser sintered Nylon 12 in rotating and reversed bending tests,” *Mater. Sci. Technol.*, vol. 31, no. 8, pp. 904–911, 2015, doi: 10.1179/1743284715y.0000000014.

[119] J. Munguia and K. Dalgarno, “Fatigue behaviour of laser-sintered PA12 specimens under four-point rotating bending,” *Rapid Prototyp. J.*, vol. 20, no. 4, pp. 291–300, 2014, doi: 10.1108/RPJ-07-2012-0064.

[120] H. Amel, J. Rongong, H. Moztarzadeh and N. Hopkinson, “Effect of section thickness on fatigue performance of laser sintered nylon 12,” *Polym. Test.*, vol. 53, pp. 204–210, Aug. 2016, doi: 10.1016/j.polymertesting.2016.05.027.

[121] D. Schob *et al.*, “Experimental determination and numerical simulation of material and damage behavior of 3D printed polyamide 12 under cyclic loading,” *Eng. Fract. Mech.*, vol. 229, 2020, doi:

doi.org/10.24423/aom.3162.

[122] Y. J. Kim, H. You, S. J. Kim and G. J. Yun, “Effects of porosity on the fatigue life of polyamide 12 considering crack initiation and propagation,” *Adv. Compos. Mater.*, vol. 29, no. 4, pp. 399–421, Jul. 2020, doi: 10.1080/09243046.2020.1738635.

[123] E. Castillo, A. Fernández-Canteli and D. Siegele, “Obtaining S–N curves from crack growth curves: an alternative to self-similarity,” *Int. J. Fract.*, vol. 187, no. 1, pp. 159–172, May 2014, doi: 10.1007/s10704-014-9928-6.

[124] M. Blattmeier, G. Witt, J. Wortberg, J. Eggert and J. Toepker, “Influence of surface characteristics on fatigue behaviour of laser sintered plastics,” *Rapid Prototyp. J.*, vol. 18, no. 2, pp. 161–171, 2012, doi: 10.1108/13552541211212140.

[125] H. Kitagawa and S. Takahashi, “Applicability of fracture mechanics to very small cracks or the cracks in the early stage,” in *Proceedings of the Second International Conference on Mechanical Behavior of Materials.*, 1976, pp. 627–631.

[126] F. Paris, P., Erdogan, “A critical analysis of crack propagation laws,” *ASME J. basic Eng.*, vol. 85(4), pp. 528–533, 1963.

[127] M. H. El Haddad, K. N. Smith and T. H. Topper, “Fatigue Crack Propagation of Short Cracks.,” *Am. Soc. Mech. Eng.*, no. 78-Mat-7, 1978, doi: 10.1016/b0-08-043152-6/00516-7.

[128] M. H. El Haddad, K. N. Smith and T. H. Topper, “Fatigue Crack Propagation of Short Cracks,” *J. Eng. Mater. Technol.*, vol. 101, no. 1, p. 42, 2010, doi: 10.1115/1.3443647.

[129] C. Garb, M. Leitner, B. Stauder, D. Schnubel and F. Grün, “Application of modified Kitagawa-Takahashi diagram for fatigue strength assessment of cast Al-Si-Cu alloys,” *Int. J. Fatigue*, vol. 111, no. January, pp. 256–268, 2018, doi: 10.1016/j.ijfatigue.2018.01.030.

[130] R. Aigner, S. Pusterhofer, S. Pomberger, M. Leitner and M. Stoschka, “A probabilistic Kitagawa-Takahashi diagram for fatigue strength assessment of cast aluminium alloys,” *Mater. Sci. Eng. A*, vol. 745, no. November 2018, pp. 326–334, 2019, doi: 10.1016/j.msea.2018.12.108.

[131] K. Tanaka, Y. Nakai and M. Yamashita, “Fatigue growth threshold of

small cracks," *Int. J. Fract.*, vol. 17, no. 5, pp. 519–533, 1981, doi: 10.1007/BF00033345.

[132] R. O. Ritchie and J. Lankford, "in Small Fatigue Cracks," Warrendale: AIME, 1986, pp. 559–586.

[133] K. Sadananda and S. Sarkar, "Modified Kitagawa diagram and transition from crack nucleation to crack propagation," *Metall. Mater. Trans. A Phys. Metall. Mater. Sci.*, vol. 44, no. 3, pp. 1175–1189, 2013, doi: 10.1007/s11661-012-1416-x.

[134] J. . Peters and R. . Ritchie, "Foreign-object damage and high-cycle fatigue of Ti–6Al–4V," *Mater. Sci. Eng. A*, vol. 319–321, pp. 597–601, Dec. 2001, doi: 10.1016/S0921-5093(01)00982-0.

[135] Electro Optical Solutions, "PA 2200 Datasheet." 2007. [Online]. Available: http://www.3dformtech.fi/lataukset/Material-Data-PA2200.pdf

[136] Evonik, "VESTAMID: Polyamide 12. Innovative and reliable".

[137] GRANTA, "CES EduPack." 2020.

[138] L. Li, C. Y. Li, C. Ni, L. Rong and B. Hsiao, "Structure and crystallization behavior of Nylon 66/multi-walled carbon nanotube nanocomposites at low carbon nanotube contents," *Polymer (Guildf).*, vol. 48, no. 12, pp. 3452–3460, 2007, doi: 10.1016/j.polymer.2007.04.030.

[139] Z. Cai *et al.*, "The structure evolution of polyamide 1212 after stretched at different temperatures and its correlation with mechanical properties," *Polymer (Guildf).*, vol. 117, pp. 249–258, 2017, doi: 10.1016/j.polymer.2017.04.037.

[140] E. Moeskops, N. Kamperman, B. van der Vorst and R. Knoppers, "Creep behaviour of Polyamide in Selective Laser Sintering," vol. 19, no. 1, p. 55, 2004, [Online]. Available: http://eprints.uanl.mx/5481/1/1020149995.PDF

[141] B. Crist and J. M. Schultz, "Polymer spherulites: A critical review," *Prog. Polym. Sci.*, vol. 56, pp. 1–63, 2016, doi: 10.1016/j.progpolymsci.2015.11.006.

[142] S. Gogolewski, K. Czerntawska and M. Gastorek, "Effect of annealing on thermal properties and crystalline structure of polyamides. Nylon 12

(polylaurolactam)," *Colloid Polym. Sci.*, vol. 258, no. 10, pp. 1130–1136, Oct. 1980, doi: 10.1007/BF01382456.

[143] American Society for Testing and Materials, *ASTM D5023-07: Standard Test Method for Plastics: Dynamic Mechanical Properties: In Flexure (Three-Point Bending)*. 2007.

[144] American Society for Testing and Materials, "ASTM D638-14: Standard Test Method for Tensile Properties of Plastics," *Annu. B. ASTM Stand.*, pp. 1–15, 2015, doi: 10.1520/D0638-14.1.

[145] American Society for Testing and Materials, "ASTM D5045-99: Standard Test Methods for Plane-Strain Fracture Toughness and Strain Energy Release Rate of Plastic Materials," *Annu. B. ASTM Stand.*, vol. 99, no. Reapproved, pp. 1–9, 1996, doi: 10.1520/D5045-99R07E01.2.

[146] American Society for Testing and Materials, *ASTM E647-13a: Standard Test Method for Measurement of Fatigue Crack Growth Rates*. 2014, pp. 1–50. doi: 10.1520/E0647-13A.2.

[147] W. J. G. (Eds) Moore, D.R., Pavan, A., *Fracture Mechanics Testing Methods for Polymers, Adhesives and Composites*. Holanda: Elsevier Science Ltd. And ESIS, 2001. doi: 10.1017/CBO9781107415324.004.

[148] M. Crespo, "Fractura a altas velocidades de deformación de probetas entalladas de poliamida 12 fabricadas por sinterizado láser selectivo," Universidad Rey Juan Carlos, 2019.

[149] International Organization for Standardization, "ISO 13586:2000. Plastics - Determination of fracture Toughness- Linear Elastic Fracture Mechanics (LEFM)." 2000.

[150] American Society for Testing and Materials, *ASTM E1820-13: Standard Test Method for Measurement of Fracture Toughness*. 2013, pp. 1–54. doi: 10.1520/E1820-13.Copyright.

[151] G. E. Hale and F. Ramsteiner, "J-fracture toughness of polymers at slow speed," in *Fracture mechanics testing methods for polymers, adhesives and composites.*, vol. 1, D. R. Moore, A. Pavan and J. G. Williams, Eds. The Netherlands: Elsevier Science Ltd., and ESIS, 2001, pp. 123–157. doi: 9780080436890.

[152] L. Castellani, "Fatigue crack growth of polymers," in *Fracture mechanics testing methods for polymers, adhesives and composites.*, W. J. G. (Eds)

Moore, D.R., Pavan, A., Ed. The Netherlands: Elsevier Science Ltd., and ESIS, 2001, pp. 91–118.

[153] American Society for Testing and Materials, "ASTM D7791-12: Standard Test Method for Uniaxial Fatigue Properties of Plastics," *Annu. B. ASTM Stand.*, vol. i, pp. 1–15, 2005, doi: 10.1520/D7791-12.2.

[154] R. C. Rice, "Fatigue Data Analysis," in *Metals Handbook, 9th, Vol. 8, Mechanical Testing and Evaluation*, ASM International, 1985. doi: 10.31399/asm.hb.v08.a0009219.

[155] Martín-Meizoso, "Cálculo del Límite de Fatiga mediante el Método de Máxima Verosimilitud," *An. Mecánica la Fract.*, vol. 2, no. November 2014, pp. 406–410, 2009.

[156] P. Davoli, A. Bernasconi, M. Filippini, S. Foletti and I. V. Papadopoulos, "Independence of the torsional fatigue limit upon a mean shear stress," *Int. J. Fatigue*, vol. 25, no. 6, pp. 471–480, 2003, doi: 10.1016/S0142-1123(02)00174-3.

[157] C. Müller, M. Wächter, R. Masendorf and A. Esderts, "Accuracy of fatigue limits estimated by the staircase method using different evaluation techniques," *Int. J. Fatigue*, vol. 100, pp. 296–307, 2017, doi: 10.1016/j.ijfatigue.2017.03.030.

[158] D. Petersen, R. Link, J. Braam and S. van der Zwaag, "A Statistical Evaluation of the Staircase and the ArcSinVP Methods for Determining the Fatigue Limit," *J. Test. Eval.*, vol. 26, no. 2, p. 125, 1998, doi: 10.1520/JTE11982J.

[159] S. Cravero and C. Ruggieri, "Estimation procedure of J-resistance curves for SE(T) fracture specimens using unloading compliance," *Eng. Fract. Mech.*, vol. 74, no. 17, pp. 2735–2757, Nov. 2007, doi: 10.1016/j.engfracmech.2007.01.012.

[160] J. Guo, J. Bai, K. Liu and J. Wei, "Surface quality improvement of selective laser sintered polyamide 12 by precision grinding and magnetic field-assisted finishing," *Mater. Des.*, vol. 138, no. January 2018, pp. 39–45, 2018, doi: 10.1016/j.matdes.2017.10.048.

[161] Z. Xu, Y. Wang, D. Wu, K. P. Ananth and J. Bai, "The process and performance comparison of polyamide 12 manufactured by multi jet fusion and selective laser sintering," *J. Manuf. Process.*, vol. 47, no. June,

pp. 419–426, 2019, doi: 10.1016/j.jmapro.2019.07.014.

[162] I. Raphael, N. Saintier, G. Robert, J. Béga and L. Laiarinandrasana, “On the role of the spherulitic microstructure in fatigue damage of pure polymer and glass-fiber reinforced semi-crystalline polyamide 6.6,” *Int. J. Fatigue*, vol. 126, no. April, pp. 44–54, 2019, doi: 10.1016/j.ijfatigue.2019.04.036.

[163] D. J. Sheskin, *Parametric and non parametric statistical procedures: Second edition*. LLC, FL., 2003.

[164] G. V. Salmoria, J. L. Leite, L. F. Vieira, A. T. N. Pires and C. R. M. Roesler, “Mechanical properties of PA6/PA12 blend specimens prepared by selective laser sintering,” *Polym. Test.*, vol. 31, no. 3, pp. 411–416, 2012, doi: 10.1016/j.polymertesting.2011.12.006.

[165] R. Greco and L. Nicolais, “Glass transition temperature in nylons,” *Polymer (Guildf).*, vol. 17, no. 12, pp. 1049–1053, Dec. 1976, doi: 10.1016/0032-3861(76)90005-7.

[166] G. V. Salmoria, J. L. Leite, L. F. Vieira, A. T. N. Pires and C. R. M. Roesler, “Mechanical properties of PA6/PA12 blend specimens prepared by selective laser sintering,” *Polym. Test.*, vol. 31, no. 3, pp. 411–416, 2012, doi: 10.1016/j.polymertesting.2011.12.006.

[167] X. Cui and D. Yan, “Preparation, characterization and crystalline transitions of odd-even polyamides 11,12 and 11,10,” *Eur. Polym. J.*, vol. 41, no. 4, pp. 863–870, 2005, doi: 10.1016/j.eurpolymj.2004.10.045.

[168] W. Zhu, C. Yan, Y. Shi, S. Wen, J. Liu and Y. Shi, “Investigation into mechanical and microstructural properties of polypropylene manufactured by selective laser sintering in comparison with injection molding counterparts,” *Mater. Des.*, vol. 82, pp. 37–45, 2015, doi: 10.1016/j.matdes.2015.05.043.

[169] B. Crist, C. J. Fisher and P. R. Howard, “Mechanical properties of model polyethylenes: tensile elastic modulus and yield stress,” *Macromolecules*, vol. 22, no. 4, pp. 1709–1718, Apr. 1989, doi: 10.1021/ma00194a035.

[170] T. Yu, C. M. Wu, C. Y. Chang, C. Y. Wang and S. P. Rwei, “Effects of crystalline morphologies on the mechanical properties of carbon fiber reinforcing polymerized cyclic butylene terephthalate composites,”

Express Polym. Lett., vol. 6, no. 4, pp. 318–328, 2012, doi: 10.3144/expresspolymlett.2012.35.

[171] A. A. Mousa, "The effects of content and surface modification of filler on the mechanical properties of selective laser sintered polyamide12 composites," *Jordan J. Mech. Ind. Eng.*, vol. 8, no. 5, pp. 265–274, 2014.

[172] W. Hao, Y. Liu, T. Wang, G. Guo, H. Chen and D. Fang, "Failure analysis of 3D printed glass fiber/PA12 composite lattice structures using DIC," *Compos. Struct.*, vol. 225, no. June, p. 111192, 2019, doi: 10.1016/j.compstruct.2019.111192.

[173] P. E. Bretz, R. W. Hertzberg and J. A. Manson, "The effect of molecular weight on fatigue crack propagation in nylon 66 and polyacetal," *J. Appl. Polym. Sci.*, vol. 27, no. 5, pp. 1707–1717, May 1982, doi: 10.1002/app.1982.070270527.

[174] L. Engel, H. Klingele, G. W.Ehrenstein and H. Schaper, *An Atlas of Polymer Damage*. Cologne, 1978.

[175] A. Salazar, A. Rico, S. Rodríguez, J. M. Navarro and J. Rodríguez, "Relating fracture behavior to spherulite size in conrolled-rheology polypropylenes," *Polym. Eng. Sci.*, vol. 52, no. 4, pp. 805–813, Apr. 2012, doi: 10.1002/pen.22145.

[176] E. Castillo and A. Fernandez-Canteli, *A Unified Statistical Methodology for Modeling Fatigue Damage*. Dordrecht: Springer Netherlands, 2009. doi: 10.1007/978-1-4020-9182-7.

[177] K. Friedrich, "Crazes and shear bands in semi-crystalline thermoplastics," in *Crazing in Polymers*, Berlin/Heidelberg: Springer-Verlag, pp. 225–274. doi: 10.1007/BFb0024059.

[178] A. Pawlak and A. Galeski, "Plastic Deformation of Crystalline Polymers: The Role of Cavitation and Crystal Plasticity," *Macromolecules*, vol. 38, no. 23, pp. 9688–9697, Nov. 2005, doi: 10.1021/ma050842o.

[179] G. Shen, J. A. Gianetto and W. R. Tyson, "Measurement of J-R Curves using single-specimen technique on clamped SE(T) specimens," 2009.

[180] J. M. Larsen, A. H. Rosenberger, B. D. Worth, K. Li, D. C. Maxwell and W. K. Porter, "Assuring reliability of gamma titanium aluminides in long-term service," in *Gamma titanium aluminides. The Materials, Metals and Minerals Society*, 1999, pp. 463–472.

[181] M. Ciavarella and F. Monno, “On the possible generalizations of the Kitagawa-Takahashi diagram and of the El Haddad equation to finite life,” *Int. J. Fatigue*, vol. 28, no. 12, pp. 1826–1837, 2006, doi: 10.1016/j.ijfatigue.2005.12.001.

[182] G. Hénaff and A.-L. Gloanec, “Fatigue properties of TiAl alloys,” *Intermetallics*, vol. 13, no. 5, pp. 543–558, May 2005, doi: 10.1016/j.intermet.2004.09.007.

LIST OF FIGURES

LIST OF TABLES

A.1 MATLAB® script to to obtain J-R curves using the normalization method

```
%NORMALIZATION METHOD FOR PA-12
%DATA
W= ;          % [mm]   WIDTH (40 mm)
B= ;          % [mm]  THICKNESS (mm)
Bn= ;              % [mm]     NET THICKNESS(mm)
a0= ;          % [mm]     INITIAL CRACK SIZE (mm)
aF= ;          % [mm]    FINAL CRACK SIZE (mm)
v= ;           % [-]     POISSON'S RATIO
E= ;          % [MPa]     YOUNG'S MODULUS (GPa)
LIC= ;          % [MPa]     ULTIMATE TENSILE STRENGHT(MPa)
C= ;       % [mm/N]   COMPLIANCE (mm/N)

    %         PART 1              %%

if 0.4<=a0/W<=0.70;                                %-1- GEOMETRY COND 1.
elseif aF-a0<=(0.15*(W-a0))||aF-a0<8;                        %-2- GEOMETRY COND 2.
   Pexcel= xlsread('SPECIMEN_NAME.xls', 1,'B4:B144');        %-3- [N] LOAD FORCE
   DATA FROM EXCEL (N)
   Dexcel= xlsread('SPECIMEN_NAME.xls', 1,'C4:C144');        %-3- [mm] LOAD
   DISPLACEMENT DATA FROM EXCEL (mm)
   funD=fit(Dexcel,Pexcel,'poly9');
   Dim_Pexcel=numel(Pexcel);
   Div_Pexcel=fix(Dim_Pexcel/3);
   counterX_P=1;
   for i=1:Div_Pexcel
       X_P=counterX_P;
       D(i,1)=Dexcel(X_P,1);
       P(i,1)=funD(D(i,1));
       counterX_P=X_P+3;
   end
   P(Div_Pexcel,1)=Pexcel(Dim_Pexcel,1);
   %[N] MAXIMUM FORCE OBTAINED AND LOCATION IN THE CURVE
   P_MAX= max(P);
   LOC=zeros(Div_Pexcel,1);
   for i=1:Div_Pexcel;
      if P(i,1)==P_MAX;
       LOC(i,1)=1;
```

```
30.       elseif P(i,1)~=P_MAX;
31.        LOC(i,1)=0;
32.       end
33.    end
34.    [x_P_MAX,y_P_MAX]=find(LOC);    %LOCATION P_MAX.
    %[N] P INCREASE
35.    P1= P(1:x_P_MAX-1);
36.    AP=zeros(x_P_MAX-1,1);
37.    for i=1:x_P_MAX-1;
38.       if i==1;
39.          AP(i,1)=0;
40.       elseif 1<i<=x_P_MAX-1;
41.          AP(i,1)=P1(i,1)-P1(i-1,1);
42.       end
43.    end
    %[mm]  D INCREASE
44.    D1= D(1:x_P_MAX-1);
45.    AD=zeros(x_P_MAX-1,1);
46.    for i=1:x_P_MAX-1;
47.       if i==1;
48.          AD(i,1)=0;
49.       elseif 1<i<=x_P_MAX-1;
50.          AD(i,1)=D1(i,1)-D1(i-1,1);
51.       end
52.    end

    % [mm/N] DISPLACEMENT COEFICIENT AGAINST FORCE;
53.    CL= AD./AP;
54.    CL(1,1)=0;

    % CRACK SIZE ESTIMATION
55.    Be= B-((B-Bn)^2)/B;
56.    U= 1./(((Be*E*CL).^(1/2))+1);    %A2.13
57.    U(1,1)=0;
58.    f_ai= 1.000196-(4.06319*U)+(11.242*U.^2)-(106.043*U.^3)+(464.335*U.^4)-
    (650.677*U.^5);    %A2.12
59.    f_ai(1,1)=W-a0;
60.    ai= f_ai*W;
    % PLASTIC DIPLACEMENT (CL/CLL)
61.    DP=D1-(P1.*C);
62.    DPL= D1-(P1.*CL);          %A15.4
63.    DN= DP./W;    % NORMALIZED PLASTIC DISPLACEMENT
```

```
    % PLASTIC AREA INCREASE
64.   APL= zeros(x_P_MAX-1,1);
65.   for i=1:x_P_MAX-1
66.     if i==1
67.         APL(1,1)=0;
68.     elseif 1<i<=x_P_MAX-1
69.         APL(i,1)=((P1(i,1)+P1(i-1,1))*(DPL(i,1)-DPL(i-1,1)))/2;      %A2.9
70.     end
71.   end

    % BLUNTING CORRECTED CRACK SIZE
72.   b_i= W-ai;
73.   n_i= 2+(0.522*b_i)/W;
74.   r_i= 1.0+(0.76*b_i)/W;
75.   Jp_i= zeros(x_P_MAX-1,1);
76.   for i=1:x_P_MAX-1
77.     if i==1
78.         Jp_i(1,1)=0;
79.     elseif 1<i<=x_P_MAX-1
80.         Jp_i(i,1)=(Jp_i(i-1,1)+(n_i(i-1,1)/b_i(i-1,1))*((APL(i,1)-APL(i-1,1))/Bn))*(1-
    (r_i(i-1,1))*((ai(i,1)-ai(i-1,1))/b_i(i-1,1)));    %A2.8
81.     end
82.   end
83.  F=((2+f_ai).*(0.886+(4.64*f_ai)-(13.32*f_ai.^2)+(14.72*f_ai.^3)-
    (5.6*f_ai.^4))./((1-f_ai).^(3/2));    %A2.3
84.   Ki=(P1/((B*Bn*W)^(1/2))).*F;   %A2.2
85.   Ji=(Ki.^2*(1-v^2)/E)+Jp_i;  %A2.5
    % CRACK GROWTH(mm)
86.   ab_i= a0+(Ji/(2*LIC));      %A15.2
87. % NORMALIZED FORCE (N)
88.   counter1=0;         %- COUNTER N.FORCE
89.   for i=1:x_P_MAX-1
90.     if ab_i(i,1)<=aF
91.         cDN1=counter1+1;                        %-CONDITION ab_i<=aF
92.         PNS(i,1)= P1(i,1)/(W*B*(((W-ab_i(i,1))/W)^(2+0.522*(W-ab_i(i,1))/W)));  %-
    LOWER CRACK GROWTH
93.         DNS(i,1)=DN(i,1);
94.         counter1=cDN1;
95.     elseif ab_i(i,1)>aF
96.         break
97.     end
98.   end
99.   PN(1,1)=0;
```

```
100.        countersmooth=0;
101.        for i=1:cDN1;
102.          if i<=cDN1-3
103.            APN=(PNS(i+1,1)+PNS(i+2,1)+PNS(i+3,1))/3;
104.          elseif i>=cDN1-3 && i==cDN1-2
105.            APN=(PNS(i+1,1)+PNS(i+2,1))/2;
106.          else
107.             break
108.          end
109.          if PNS(i,1)>APN
110.            break
111.          elseif PNS(i,1)<=APN;
112.            cDN1smooth=countersmooth+1;
113.          end
114.          countersmooth=cDN1smooth;
115.          DN1(1,i)=DNS(i,1);
116.          PN(1,i)=PNS(i,1);
117.        end
118.      end

      %%%    FIGURES    %%%
119.      Pg=P';
120.      Dg=D';
121.      figure; hold on; grid;
122.      plot(Dg,Pg);
123.      axis([0 4 0 2000]);
124.      legend('Curve 1 Force-Displa.');
125.      ylabel('Force (N)');
126.      xlabel('Displacement (TOTAL) (mm)');
127.      P1g=P1';
128.      D1g=D1';
129.      figure; hold on; grid;
130.      plot(D1g,P1g);
131.      axis([0 3 0 2000]);
132.      legend('Curva 2 Force-Displa.');
133.      ylabel('Force (N)');
134.      xlabel('Desplazamiento (MAX) (mm)');
135.      PNg=PN';
136.      DN1g=DN1;
137.      LineWidht=2;
138.      figure; hold on; grid;
139.      plot(DN1g, PNg);
140.      axis([0 0.5 0 25]);
```

```
141.      legend('Curva 3 NORMALIZED  Force-Displ.');
142.      ylabel('Force (N/mm2)');
143.      xlabel('Displacement (mm/W)')

    % PART 2 EXCLUSION OF Vpli/W<=0.001  %%%%%

144.      counter2=0;
145.      for i=1:cDN1smooth
146.         if DNS(i,1)>=0.001;
147.            cDN2=counter2+1;
148.            DN2(cDN2,1)=DNS(i,1);
149.            PN2(cDN2,1)=PNS(i,1);
150.            counter2=cDN2;
151.         end
152.      end
    %%%   FIGURES WITH EXCLUSION OF Vpli/W<=0.001   %%%%%
153.      PN2g=PN2';
154.      DN2g=DN2';
155.      figure; hold on; grid;
156.      plot(DN2g,PN2g);
157.      axis([0 0.25 0 25]);
158.      legend('Curve 4 NORMALIZED  Force-Displ.');
159.      ylabel('Force (N/mm2)');
160.      xlabel('Displacement (Vpli/W<=0.001) (mm/W)');

    %%%%%%    PART 3  LINE CREATION    %%%%%%%

161.      x_D_MAX_ARRAY=Div_Pexcel;
162.      x_P_MAX_ARRAY=x_D_MAX_ARRAY;
163.      cDN3=x_D_MAX_ARRAY-((cDN1smooth-cDN2));
164.      DN3=zeros(cDN3,1);
165.      PN3=zeros(cDN3,1);
166.      for i=1:cDN2;
167.         PN3(i,1)=PN2(i,1);
168.        DN3(i,1)=DN2(i,1);
169.      end
170.      DN3(cDN3,1)= (D(x_D_MAX_ARRAY,1)-P(x_P_MAX_ARRAY,1)*C)/W;
171.      PN3(cDN3,1)= P(x_P_MAX_ARRAY,1)/(W*B*(((W-aF)/W)^(2+0.522*(W-
    a0)/W)));
172.      m=(PN3(cDN3,1)-(PN3(cDN2,1)))/(DN3(cDN3,1)-DN3(cDN2,1));
173.      counter3=cDN2;
174.      for i=(cDN1smooth+1):x_P_MAX_ARRAY;
175.         cDN3=counter3+1;
```

```
176.        DN3(cDN3,1)= (D(i,1)-P(i,1)*C)/W;
177.        counter3=cDN3;
178.      end
179.      counter4=cDN2;
180.      for i=(cDN1smooth+1):x_P_MAX_ARRAY;
181.        cPN3=counter4+1;
182.        PN3(cPN3,1)=PN3(cDN2,1)+(m*(DN3(cPN3,1)-DN3(cDN2,1)));
183.        counter4=cPN3;
184.      end
    %%%  LINE CREATION FIGURE    %%%
185.      PN3g=PN3';
186.      DN3g=DN3';
187.      figure; hold on; grid;
188.      plot(DN3g, PN3g);
189.      axis([0 0.25 0 25]);
190.      legend('Curve 5 NORMALIZED  Force-Displ.');
191.      ylabel('Force (N/mm2)');
192.      xlabel('Displacement (mm/W)');

    %   PART 4 FITTING FUNCTION     %%%%%

    %cftool(DN3,PN3)
193.      p1=228.3;
194.      p2=7.44;
195.      p3=0;
196.      q1=0;
197.      PN4=((p3+(DN3*p2)+((DN3.^2)*p1))./(DN3+q1));   %R-square=0.9765
    %%% FIGURE 4 FITTING FUNCTION  %%%
198.      PN4g=PN4';
199.      DN3g=DN3';
200.      figure; hold on; grid;
201.      plot(DN3g, PN4g);
202.      axis([0 0.1 0 25]);
203.      legend('Curve 6 NORMALIZED  Force-Displ.');
204.      ylabel('Force (N/mm2)');
205.      xlabel('Displacement (mm/W)');

    %%%   PART 5        ITERATION          %%%%%

206.      counter5=0;
207.      counter6=x_D_MAX_ARRAY-cDN3;
208.      if counter6==0;
209.        counter6=1;
```

```
    end
    ag=0.001;                % CRACK INCREMENT.
    AF4(1,1)=a0;             % FINAL CRACK LENGHT
    eta=2+0.522*(W-a0)/W;    %PLASTIC ETHA
    for i=1:cDN3;
        if DN3(i,1)>=0.002;
            cDN5=counter5+1;
            cPN6=counter6;
            DN5(cDN5,1)=DN3(i,1);   % NORM. DISPLACEMENT
            PN5(cDN5,1)=P(counter6,1)/(W*Be*(((W-AF4(cDN5,1))/W)^eta));
            PN6=PN4(cDN5,1);        % NORM. FORCE WITH ADJUST
            grieta=AF4(cDN5,1);
            con=(PN5(cDN5,1)-PN6)/PN6*100;
            while ~(con>=-0.1 && con<=0.1);
              if PN5(cDN5,1)<PN6
                AF4(cDN5,1)=grieta+ag;
                PN5(cDN5,1)=P(cPN6,1)/(W*Be*(((W-AF4(cDN5,1))/W)^eta));
                con=((PN5(cDN5,1)-PN6)/PN6)*100;
                grieta=AF4(cDN5,1);
              end
              if PN5(cDN5,1)>PN6;
                AF4(cDN5,1)=grieta-ag;
                PN5(cDN5,1)=P(cPN6,1)/(W*Be*((W-AF4(cDN5,1))/W)^eta);
                con=((PN5(cDN5,1)-PN6)/PN6)*100;
                grieta=AF4(cDN5,1);
              end;
            end
          counter5=cDN5;
          AF4((cDN5+1),1)=AF4(cDN5,1);
          counter6=cPN6+1;
        end
        if AF4(1,1)<a0
          return
        end
    end
    Dim_AF4=numel(AF4);
    AF5=AF4;
    for i=2:Dim_AF4;
       if AF5(i,1)<AF5(i-1,1);
         AF5(i,1)=AF5(i-1,1);
       end
    end
```

```
% PART 5 FIGURE WITH FITTING ITERATION %%%%%

PN5g=PN5';
DN5g=DN5';
figure; hold on; grid;
z=plot(DN5g, PN5g);
plot(DN3g, PN4g);
set(z,'Color','y');
axis([0 0.3 0 20]);
legend('Curve 7 NORMALIZED FORCE-DISPL.');
ylabel('Force (N/mm2)');
xlabel('Displacement (mm/W)');

%%% J-R %%%

Ri=(AF4-a0);
funD1=fit(D,P,'poly9');
counter7=Div_Pexcel-cDN3;
  for i=1:Dim_AF4;
    ic=counter7;
    UJR(i,1)=integrate(funD1,D(ic,1),D(1,1));
    JoF(i,1)=(eta*UJR(i,1))/(Be*(W-a0));    %A2.6
    JiF(i,1)=JoF(i,1)*(1-(((0.75*eta)-1)*Ri(i,1))/(W-a0));
    counter7=ic+1;
  End

%%% SMOOTH J-R %%%%%

smooth_AF6=zeros(Dim_AF4,1);
for i=2:Dim_AF4-20
  if JiF(i,1)>=JiF(i-1,1)&& Ri(i,1)<=Ri(i-1,1)
    smooth_AF6(i,1)=1;
    for v=2:i-1
      if smooth_AF6(v,1)==1
        smooth_AF6(v,1)=0;
      end
    end
  end
end
[x_smooth_AF6,y_smooth_AF6]=find(smooth_AF6);
JiF6(1,1)=0;
Ri6(1,1)=0;
cAF6=1;
```

```
287.      for i=x_smooth_AF6:Dim_AF4
288.         counter9=cAF6+1;
289.         JiF6(counter9,1)=JiF(i,1);
290.         Ri6(counter9,1)=Ri(i,1);
291.         cAF6=counter9;
292.      end
293.      for i=1:cAF6-1
294.          PJiF6(i,1)=JiF6(i+1,1);
295.          PRi6(i,1)=Ri6(i+1,1);    %a=16.99 b=0.4845  f(x) = a*x^b
296.      end

    %%%          FIGURE R-J       %%%

297.      JiFg=JiF';
298.      Rig=Ri';
299.      JiFg6=JiF6';
300.      Rig6=Ri6';
301.      figure; hold on; grid;
302.      plot(Rig, JiFg);
303.      z=plot(Rig6, JiFg6);
304.      set(z,'Color','g');
305.      axis([0 3 0 25]);
306.      legend('Curva 8 NORMALIZADA  J-R');
307.      ylabel('J (N/mm2)');
308.      xlabel('R');
    %  DATA EXPORT TO EXCEL %%

    %Curve 1 SMOOTH FORCE-DISPL. --F(N)/D(mm)--
309.      xlswrite('SPECIMEN_NAME.xls',P, 1,'D4')
310.      xlswrite('SPECIMEN_NAME.xls',D, 1,'E4')

    %Curve 2    MAX FORCE.-DISPL. --F(N)/D(mm)--
311.      xlswrite('SPECIMEN_NAME.xls',P1, 1,'F4')
312.      xlswrite('SPECIMEN_NAME.xls',D1, 1,'G4')

    %Curve 3 NORMALIZED  FORCE-DISPL. --F(N/mm2)/D(mm/W)--
313.      xlswrite('SPECIMEN_NAME.xls',PN', 1,'H4')
314.      xlswrite('SPECIMEN_NAME.xls',DN1', 1,'I4')

    %%%Curve 4 EXCLUSION OF Vpli/W<=0.001  --F(N/mm2)/D(mm/W)--
315.      xlswrite('SPECIMEN_NAME.xls',PN2, 1,'J4')
316.      xlswrite('SPECIMEN_NAME.xls',DN2, 1,'K4')
```

```
    %Curve 5 FORCE-DISPL LINE. --F(N/mm2)/D(mm/W)
317.    xlswrite('SPECIMEN_NAME.xls',PN3, 1,'L4')
318.    xlswrite('SPECIMEN_NAME.xls',DN3, 1,'M4')

    %Curve 6 FITTING --F(N/mm2)/D(mm/W)
319.
320.    xlswrite('SPECIMEN_NAME.xls',PN4, 1,'N4')
321.    xlswrite('SPECIMEN_NAME.xls',DN3, 1,'O4')

    %Curve 7 ITERATIVE FITTING --F(N/mm2)/D(mm/W)
322.    xlswrite('SPECIMEN_NAME.xls',PN5, 1,'P4')
323.    xlswrite('SPECIMEN_NAME.xls',DN5, 1,'Q4')

    %Curve 8 NORMALIZED  J-R
324.    xlswrite('SPECIMEN_NAME.xls',JiF, 1,'R4')
325.    xlswrite('SPECIMEN_NAME.xls',Ri, 1,'S4')

    %Curve 8 NORMALIZED  J-R SMOOTH
326.    xlswrite('SPECIMEN_NAME.xls',JiF6, 1,'T4')
327.    xlswrite('SPECIMEN_NAME.xls',Ri6, 1,'U4')
```

A.2 MATLAB® script for the Maximum likelihood function

```
1.  function FatigueLimit
    %FATIGUE LIMIT (Matlab 7.0.0 code: fatiguelimit.m)
    %It reads an Excel table with three columns:
    %Stress, Number of Failures, Number of Run-outs.
    %A normal distribution for the stress limit is assumed.
    %MAXIMUM LIKELIHOOD is used.
    %Function at likelihood.m is required
2.  clear all
3.  namefile=input('Name.xlsx', 's');
4.  data=xlsread(namefile);
5.  S=data(:,1); %The stresses (or loads, or strains) in the first column
6.  f=data(:,2); %Number of failures
7.  r=data(:,3); %Number of run-outs
8.  mu=S(fix(length(S)/2)); %Initial value for the mean
9.  sigma=S(2)-S(1); %Initial value for the standard deviation
10. mu0_sig0=[mu sigma]; %Initial values for mu and sigma
11. [optmusig]=fminsearch(@likelihood,mu0_sig0,[],S,f,r)
12. function like = likelihood(vmus,S,f,r) %Computes likelihood
13. mu =vmus(1); %Mean value for the normal distribution
14. sigma=vmus(2); %Standard deviation
15. like=-1; %Likelihood. Negative because 'fminsearch' searches minimums
16. for i=1:length(S);
17. like=like*(1-normcdf(S(i),mu,sigma)).^r(i).*normcdf(S(i),mu,sigma).^f(i);
18. end
```